DISS. ETH NO.28904

Three Stages of Phosphonic Acid Modification Applied to the Aluminum Oxide Surface

A thesis submitted to attain the degree of

DOCTOR OF SCIENCES

(DR. sc. ETH Zurich)

presented by

Ruohan Zhao

M.Sc., Universität Duisburg-Essen

University of Science and Technology Beijing

born on 17.11.1990

citizen of China

accepted on the recommendation of

Prof. Dr. M. P. Heuberger, examiner

Prof. Dr. H. Grützmacher, co-examiner

Prof. Dr. M. J. Niederberger, co-examiner

Prof. em. Dr. N. Spencer, co-examiner

Dr. L. Jeurgens, co-examiner

2022

This page intentionally left blank

Abstract

Aluminum oxide surface modification by phosphonic acid is a potential new generation of industrial surface functionalization technology. However, there are still a few technical challenges in practical application scenarios, such as heavy aluminum dissolution during the molecule adsorption process, the control of the final phosphonic acid adsorbate layer and aluminum oxide layer. Preliminary studies showed the phosphonic acid molecular structure has significant effects on aluminum dissolution inhibition, finally formed adsorbate layer morphology, and oxide layer stabilization. Building on these findings, this work systematically compares the phosphonic acid molecular steric and electron environment effects at different stages of phosphonic acid surface treatment. The aqueous soluble phosphonic acid molecules studied include the simplest phosphonic acid, alkyl/phenyl phosphonic acid derivatives with stepwise increased steric effect, and phenyl phosphonic acid derivatives with designed molecular electron environment. A phosphonic acid surface treatment decomposes in three distinctive stages, i.e. a dynamic stage during the phosphonic acid adsorption process, a final stage of the modified aluminum oxide in ambient atmosphere and a transition stage of H_2O rinsing and air-exposure oxidation between the above two stages.

During the first stage, phosphonic acid molecular structural effects on aluminum dissolution inhibition are in situ monitored by inductively coupled plasma-optical emission spectroscopy (ICP-OES). In addition, electrochemical impedance spectroscopy (EIS) evidences that two phosphonic acid adsorption modes exist, i.e. physisorption of aluminum-phosphonate complex and chemisorption of phosphonic acid layer. The first stage study shows that a higher phosphonic acid molecular steric effect improves the aluminum dissolution inhibition due to the chemisorbed phosphonic acids on the aluminum surface. The stability of this chemisorption is reduced if an electron withdrawing group decreases the electron density of the phosphonic acid anchor group.

The final stage of the phosphonic acid modified aluminum oxide surface is investigated using X-ray photoelectron spectroscopy (XPS), which allows ex situ characterization of the stratification of adsorbate phosphonic acid layer with adsorbent aluminum oxide. A phosphonic acid with higher steric increases the phosphonic acid stratification with aluminum oxide via enhanced interactions among the unreactive functional groups. Meanwhile, adsorbate high steric phosphonic acid also reduces the adsorbent aluminum re-oxidation process forming a thinner

oxide film. A time of flight- secondary ion mass spectrometry (ToF-SIMS) surface characterization evidences that physisorbed aluminum-phosphonate complexes in the first stage partially convert to chemisorbed states after the H_2O-rinsing and air-exposure steps.

Finally, the effect of the aluminum re-oxidation via air-exposure during the transition stage is studied under O_2 controlled atmosphere, using a glovebox and XPS/hard X-ray photoelectron spectroscopy (HAXPES) connected system. Oxygen and aluminum Auger parameters are used to provide a sensitive differentiation via aluminum oxide chemical state changes. It reveals that a strong aluminum re-oxidation process during the transition stage is necessary to stabilize an unstable phosphonic acid modified aluminum oxide surface. With these systematic and fundamental understandings, this work offers new perspective for the industrial application of aluminum oxide surface treatment by phosphonic acid.

Zusammenfassung

Die Oberflächenmodifizierung von Aluminiumoxid durch Phosphonsäure ist eine potenzielle neue Generation der industriellen Oberflächenfunktionalisierungstechnologie. In praktischen Anwendungsszenarien gibt es jedoch noch einige technische Herausforderungen, wie z. B. die starke Aluminiumauflösung während des Moleküladsorptionsprozesses, die Kontrolle der endgültigen Phosphonsäureadsorbatschicht und der Aluminiumoxidschicht. Vorläufige Studien zeigten, dass die Molekülstruktur der Phosphonsäure signifikante Auswirkungen auf die Hemmung der Aluminiumauflösung, die Morphologie der endgültig gebildeten Adsorbatschicht und die Stabilisierung der Oxidschicht hat. Aufbauend auf diesen Erkenntnissen vergleicht diese Arbeit systematisch die molekularen sterischen und Elektronenumgebungseffekte der Phosphonsäure in verschiedenen Stadien der Phosphonsäure-Oberflächenbehandlung. Insbesondere umfassen die untersuchten wasserlöslichen Phosphonsäuremoleküle einfachste Phosphorsäure, Alkyl/Phenyl-Phosphonsäure-Derivate mit stufenweise erhöhter sterischer Wirkung und Phenyl-Phosphonsäure-Derivate mit entworfener molekularer Elektronenumgebung. Eine Phosphonsäure-Oberflächenbehandlung gliedert sich in drei charakteristischen Phasen auf: einer dynamischen Phasen während des Phosphonsäure-Adsorptionsprozesses, einer Übergangsphase nach dem Spülen mit H_2O und der Oxidation unter Lufteinwirkung und einer finalen Phase des modifizierten Aluminiumoxids unter Umgebungsatmosphäre.

Während der ersten Phase werden die molekularen Struktureffekte der Phosphonsäure auf die Hemmung der Aluminiumauflösung in situ durch induktiv gekoppelte Plasma-Emissionsspektroskopie (ICP-OES) überwacht. Zusätzlich beweist die elektrochemische Impedanzspektroskopie (EIS), dass zwei Phosphonsäure-Adsorptionsmodi, d. h. Physisorption des Aluminium-Phosphonat-Komplexes und Chemisorption der Phosphonsäureschicht existieren. Die Studie der ersten Stufe zeigt, dass ein höhermolekularer sterischer Effekt der chemisorbierten Phosphonsäuren die Hemmung der Aluminiumauflösung auf der Aluminiumoberfläche verbessert. Die Stabilität dieser Chemisorption wird verringert, wenn eine elektronenziehende Gruppe die Elektronendichte der Phosphonsäure-Ankergruppe reduziert.

Die Endstufe der mit Phosphonsäure modifizierten Aluminiumoxidoberfläche wurde mittels Röntgenphotoelektronenspektroskopie (XPS) untersucht. Dies ermöglicht eine Ex-situ-Charakterisierung der Schichtung der adsorbierten Phosphonsäureschicht mit adsorbierendem Aluminiumoxid. Eine Phosphonsäure mit höherer Sterik erhöht die Phosphonsäureschichtung mit Aluminiumoxid durch verstärkte Wechselwirkungen zwischen den unreaktiven funktionellen

Gruppen. Zusätzlich reduziert die adsorbierte Phosphonsäure mit hohem sterischem Gehalt auch den Reoxidationsprozess des adsorbierenden Aluminiums, wodurch ein dünnerer Oxidfilm gebildet wird. Eine Oberflächencharakterisierung durch time-of-flight Sekundärionen-Massenspektrometrie (ToF-SIMS) zeigt, dass physisorbierte Aluminium-Phosphonat-Komplexe in der ersten Phase nach dem Spülschritt mit H_2O und der Luftexposition teilweise in chemisorbierte Zustände übergehen.

Schliesslich wird die Wirkung der Aluminium-Reoxidation durch Lufteinwirkung während der Übergangsphase unter kontrollierter O_2-Atmosphäre untersucht. Dazu wurden eine Glovebox und ein mit XPS/harter Röntgenstrahl-Photoelektronenspektroskopie (HAXPES) verbundenes System verwendet. Sauerstoff- und Aluminium-Auger-Parameter wurden verwendet, um eine messbare Differenzierung durch Änderungen des chemischen Zustands von Aluminiumoxid festzustellen. Dies beweist, dass ein starker Aluminium-Reoxidationsprozess während der Übergangsphase notwendig ist, um eine instabile Phosphonsäure-modifizierte Aluminiumoxidoberfläche zu stabilisieren. Mit diesen systematischen und grundlegenden Erkenntnissen bietet diese Arbeit neue Perspektiven für die industrielle Anwendung der Aluminiumoxid-Oberflächenbehandlung durch Phosphonsäure.

Table of Contents

Chapter 1. Introduction

1.1. Industrial Background

Aluminum alloys are widely used as structural materials in automobile[1], aerospace[2, 3] and construction industry due to their high strength to weight ratio, ductility, formability and low cost[4]. These extraordinary engineering properties make aluminum alloy a perfect alternative material to the traditional steel in automobile industry because aluminum alloy maintains similar frame rigidity and crash safety but with a lower vehicle body weight[5]. Especially, with the increased electronic vehicle market, aluminum alloy has already become the fastest grown automotive material[6]. To assemble the aluminum alloy for vehicle structures, organic adhesive is broadly used since it is more advanced than welding or mechanical joining: uniform stress distribution, no galvanic corrosion, low weight, cheap and easy to process (no inert gas protection)[7, 8]. The adhesive jointed aluminum alloy sheets are sandwich structures as shown in Figure 1.1[9]. A primer is often used between the aluminum oxide and adhesive to increase the adhesion and corrosion resistance of the joining part[10, 11]. Traditionally, a conventional chromate coating (CCC) on the aluminum oxide prior to the adhesive application is used as this primer. The CCC increases the adhesion and corrosion resistance due to its self-healing barrier protection on aluminum alloy surface, which is chemically stable in a wide pH range [12, 13].

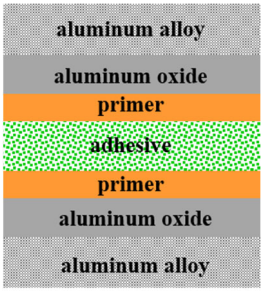

Figure 1.1. *Sandwich structure of adhesive jointed aluminum sheets: metallic aluminum alloy forms a native oxide layer once exposing in air; a primer is used to increase the adhesion and durability between aluminum oxide and adhesive.*

However, currently there is an urging requirement to replace the toxic and carcinogenic CCC on aluminum oxide especially in the automobile industrial since the use of hexavalent chromium has already been forbidden in European Union since 2007[14]. Since early 80s, researchers have already started to investigate an non-chromate conversion coating on metal surface, such as phosphoric acid anodizing[15], plasma based surface treatment[16], laser based surface treatment[17], and silane based sol-gel coating[18]. Phosphonic acid (PA) surface treatment

would be a possible new generation of non-chromate aluminum surface treatment for the automobile industry. Firstly, it is already proved that PA increased the durability of adhesive jointed aluminum alloy[19-22]. Secondly, phosphonic acid group of PA forms more stable covalent interaction with aluminum oxide surface via a condensation reaction than other molecules containing anchor groups such as carboxylic acid[23-26], amine[26] and silane groups[27-29]. Thirdly, the molecular structure and functional groups of PA molecules can be designed and functionalized to meet specific requirements[30, 31].

To develop a suitable industrial PA surface treatment for aluminum oxide, on one side, it is important to understand the main processes occurring during the PA treatment stage; i.e. the adsorption of PA on aluminum and the dissolution of aluminum under low pH condition. The aluminum dissolution can cause heavy contamination of PA solution leading to an increase in production costs (bath conditioning, filtering and control)[32]. On the other side, it is essential to characterize the final stage of PA modified aluminum oxide surface, e.g. the morphology of adsorbed PA layer, and the aluminum oxide thickness and stability. Specifically, it is broadly recognized that different PA adsorbed layers on aluminum surface strongly influence the durability of adhesive-aluminum interface[33]. Meanwhile, the heavy aluminum dissolution during the prior PA adsorption process might lead to an accumulation of aluminum-phosphonate complex on aluminum surface and a lateral heterogeneous dissolved aluminum surface. Therefore, the control of the PA adsorption process and the final PA modified aluminum oxide surface quality are the two main factors limiting the application of PA surface treatments for aluminum oxide in automotive industry. Therefore, it is essential to understand the adsorption/dissolution kinetics at the metal (aluminum subtract)/liquid (PA solution) interface; meanwhile, characterize the adsorbed PA layer and the modified aluminum oxide.

1.2. Literature Review

Previous in-situ studies on liquid-metal interfaces conducted in PA solution mainly focused on steel substrates, where various organic PA molecules were used as corrosion inhibitor. Specifically, the influence of the PA molecular structural chelating effect[34-40] on the steel corrosion inhibition in acid or Cl^- corrosive solution were studied using electrochemical impedance test (EIS): molecules such as aminotris(methylenephosphonic acid), nitrilotri(methylphosphonic acid) and 1-hydroxyethylidene diphosphonic acid were intensively compared. Meanwhile, the corrosion inhibition effect of PA molecules with varied steric and functional groups were also studied by EIS[41-43]; molecules such as laurylphosphonic acid,

ethyllaurylphosphonate, diethyllaurylphosphonate, piperidin-1-yl-phosphonic acid, and (4-phosphono-piperazin-1-yl) phosphonic acid are used as corrosion inhibitor. These studies showed that an enhanced PA molecular chelating and steric effects increased the steel corrosion resistance in corrosive electrolytes.

Based on these studies on steel substrate, EIS is also used to study the corrosion inhibition effect of PA on aluminum substrate in corrosive electrolytes [44-46]. However, different to steel, PA is commonly used to create self-assembly monolayers (SAMs) on aluminum substrate firstly. Then the corrosion resistance of this PA modified aluminum oxide in acid or Cl^- contained corrosive electrolyte was evaluated by EIS test:

A SAMs of dodecylphosphonic acid ($C_{12}H_{27}O_3P$) on aluminum alloy surface was formed by 4 hours adsorption in neutral solution followed with cleaning and annealing. The EIS test showed that the modified aluminum alloy exhibited a good corrosion resistance in Cl^- corrosive solution after an exposure of 96 hours[47]. Another work compared the influence of adsorption solution pH (i.e. acid, neutral and alkaline) on the corrosion inhibition resistance of mono-dodecyl phosphonic acid ($C_{12}H_{27}O_4P$) SAMs. The PA modified samples were immersed in Cl^- corrosive solution up to 180 hours, and then the EIS test started. The results showed that the SAMs formed in neutral adsorption environment had a better corrosion resistance[48]. Moreover, the effect of adsorption time on SAMs corrosion resistance was compared by using fluorinated PA ($CH_3(CF_2)_5(CH_2)_2PO_3H_2$) for 24 hours, 144 hours and 240 hours. The EIS test showed that a longer adsorption time provided a better corrosion resistance in Cl^- corrosive solution[49]. Then the PA steric effect on the corrosion resistance of SAMs on aluminum alloy was compared by using octylphosphonic acid ($C_8H_{19}O_3P$) and octadecylphosphonic acid ($C_{18}H_{39}O_3P$). The potentiodynamic polarization curves showed that a longer alkyl chain (high steric) presented a better corrosion resistance in Cl^- corrosive solution[26]. Additionally, the SAMs of PA was insufficient to protect aluminum alloy surface comparing to a polymer coating. One EIS study showed that the SAM of tetradecylphosphonic acid ($C_{14}H_{31}O_3P$) only provided limited inhibition on nano-porous oxide film in Na_2SO_4 and neutral pH buffer solutions[50].

These studies showed clearly that the SAMs of PA increased the aluminum corrosion inhibition in corrosive solution. Thus, it is important to identify the critical parameters of the SAMs formed by PA. The characterization of the SAMs started by using adsorbent such as gold[51] or other chemically stable substrates, e.g. tantalum oxide[52, 53], zirconium oxide [54, 55] and titanium oxide[55]. Recent studies also investigated the adsorbed PA layer on aluminum oxide

surface. The chemisorbed PA molecule interacts with the aluminum oxide surface via a condensation reaction, which creates mono-, bi- and tridentate binding modes between phosphonic acid anchor group and hydroxyl group on the aluminum oxide surface, as illustrated in Figure 1.2[56].

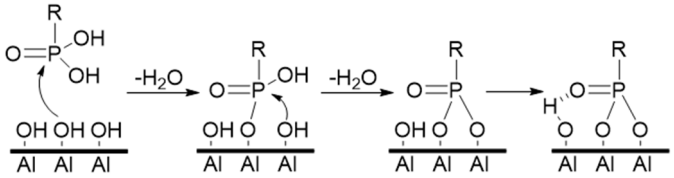

Figure 1.2. *Phosphonic acid (PA) anchor group condensation reaction with the hydroxyl group on aluminum surface.*

The molecular steric effect on the PA formed SAMs on aluminum substrate has been investigated in many previous studies. Octylphosphonic acid ($C_8H_{19}O_3P$, OPA), decylphosphonic acid ($C_{10}H_{23}O_3P$, DPA), octadecylphosphonic acid ($C_{18}H_{39}O_3P$, ODPA) and fluorinated PA ($CF_3(CF_2)_7(CH_2)_2PO_3H_2$, PFDPA) ethanol solutions were used to modified physical vapor deposited (PVD) aluminum surface for 24 hours. X-ray photoelectron spectrum spectroscopy (XPS), contact angle measurement and atomic force microscopy (AFM) surface characterization results showed that ODPA and PFDPA formed more hydrophobic SAMs than DPA and OPA. Meanwhile, ODPA formed a more densely packed SAMs on PVD aluminum surface, while DPA and OPA form a SAM of less density. Moreover, ODPA formed the most stable SAMs followed by PFDPA, DPA, and OPA[57]. The kinetics of DPA adsorbed layer on the aluminum sheet (99.99%) surface in aqueous solution is investigated by an in situ AFM study for 160 min. It showed that a few adsorbed PA islands formed on surface at the initial stage. With the increase of adsorption time, firstly, the gaps of these initial islands were filled up; then the adsorbed DPA islands grew in size but not in number[58]. Meanwhile, OPA dynamic adsorption on aluminum sheet (99.99%) in ethanol consisting of $NaClO_4 \cdot H_2O$ electrolyte up to 53 hours is studied by using odd random phase EIS. This work showed that H_2O produced during the condensation reaction stayed near oxide surface, and combined with acid, which created a local attack on aluminum oxide[59]. Meanwhile, a quartz crystal microbalance (QCM) study showed that the adsorption kinetics of ODPA was accelerated with the increase of aluminum oxide surface hydroxyl density[60].

Meanwhile, the effect of different functional groups of PA on SAMs formation is also studied by comparing fluorinated PA ($CF_3(CF_2)_7(CH_2)_{11}PO_3H_2$) with hexadecanephosphonic acid ($C_{16}H_{35}O_3P$, HDPA) and docosanephosphonic acid ($C_{20}H_{43}O_3P$, DCPA). Through infrared

spectroscopy, ellipsometry and contact angle measurement, the formation of SAMs on the aluminum oxide occurred at a faster rate for fluorinated PA than HDPA and DCPA. However, the SAMs of fluorinated PA did not reach an ordered state as HDPA and DCPA due to the steric effect of the fluorocarbon segment[61]. Another work also showed that fluorinated PA ($F_3C(CF_2)_7(CH_2)_2PO(OH)_2$) formed a more hydrophobic SAM with lower surface energy and adhesion comparing to DP and ODP formed SAM[62]. Additionally, methylphosphonic acid (CH_5O_3P, MPA), butylphosphonic acid ($C_4H_{11}O_3P$, BuPA), DPA and ODPA were used to study the hydrothermal stability of PA modified aluminum oxide. This work showed that the increased molecular steric enhanced PA modified aluminum oxide stability characterized by X-ray diffraction, nuclear magnetic resonance spectroscopy (NMRS), N_2 physisorption, and IR spectroscopy[63].

These studies provide valuable insights of PA molecular structural effect on dynamic adsorption process and the final formed PA layer on surface. However, targeting on the industrial application of aluminum surface modification, more research should combine the in situ study of PA adsorption process with ex situ characterization of final obtained PA modified aluminum oxide synchronously. Moreover, there is a lack of systematical understanding of PA structural effects in aqueous solution that is industrial favorable due to the economic and environmental cost. Additionally, the electron environment effect of PA molecule is barely considered, which theoretically varies the PA acidity and the stability of phosphonic acid anchor group interaction with aluminum/aluminum oxide.

1.3. Scope and Outline of Thesis

1.3.1. Scope of Thesis

The focus point of this work is to study the PA molecular structural effect on the phosphonic acid anchor group interaction with aluminum/aluminum oxide surface. In order to get a better mechanistic understanding of the different processes, pure aluminum is used as substrate in order to avoid the additional complex effects of the different alloying elements of aluminum alloys. Meanwhile, only water soluble PA molecules with unreactive alkyl chain/phenyl group are considered to discard any additional effect of other reactive functional groups of PA molecules.

Nine water soluble PA molecules are chosen for this study, as shown in Figure 1.3. The PA molecules can be classified in three groups; namely, (a) ***group with low steric*** effect consisting

of phosphonic acid (H_3PO_3), methylphosphonic acid (MPA), and ethylphosphonic acid (EPA); (b) ***group with high steric*** effect consisting of tert-butylphosphonic acid (tBPA), benzylphosphonic acid (BPA), and (2-phenylethyl)phosphonic acid (PePA); (c) ***group with high steric*** *effect and* ***varied electronic environment*** consisting of (4-cyanophenyl)phosphonic acid (CnPPA), phenylphosphonic acid (PPA) and (4-methoxyphenyl)phosphonic acid (MtPPA).

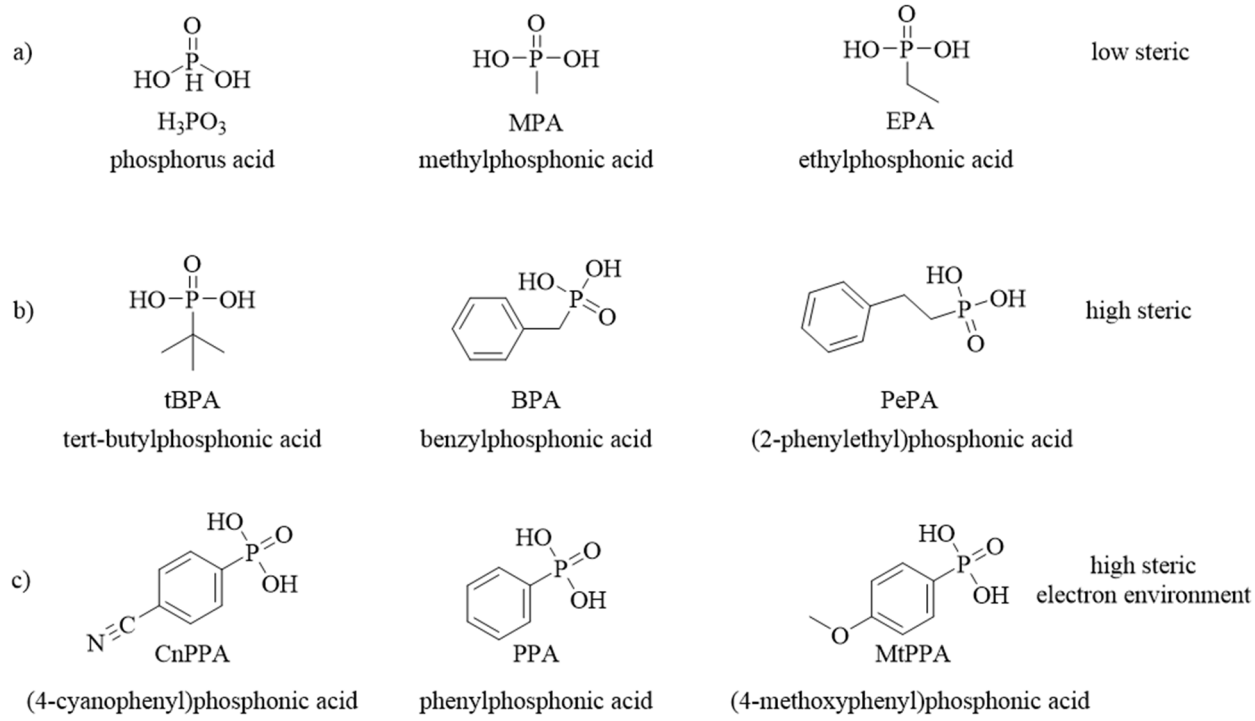

Figure 1.3. *Selection of phosphonic acid molecules exhibiting systematically different steric and electron environment effects. The first two groups exhibit similar electron environment at the phosphorus center, but with increasing steric of the functional group, namely a) "low steric" and b) "high steric". The group, c) "high steric electron environment" contrasts electron delocalization, i.e. via electron-withdrawing (CnPPA) and electron-donating (MtPPA) functional groups.*

In groups a) and b), the extent of the steric influence is solely determined by the size and nature of the hydrocarbon substituent connected to the phosphonic acid anchor group. To study the electron environment effect, phenyl phosphonic acids considered in this work include substituted phenyl phosphonic acids with decreasing electron withdrawing effect: (4-cyanophenyl)phosphonic acid (CnPPA) < phenylphosphonic acid (PPA) < (4-methoxyphenyl)phosphonic acid (MtPPA). The cyano and methoxy functional groups of the CnPPA and MtPPA molecules are respectively electron withdrawing and donating in nature, whereas the phenyl group of PPA is slightly electron withdrawing due to its resonance effect. Specifically, cyano and methoxy groups are either electron -withdrawing or -donating in nature, which means the

electron densities of phosphonic acid anchor groups of two molecules are changed due to different functional groups (electron density delocalization), i.e. the electron density of phosphonic acid group is reduced with an electron withdrawing group (cyano group of CnPPA) at the para position of phenyl ring; conversely, electron density of phosphonic acid group is increased with an electron donating group (methoxy group of MtPPA) at the para position of phenyl ring, as shown in Figure 1.4.[32]. Electron withdrawal from the phosphorus center decreases the electron density of the phosphonic acid anchor group, which reduces the stability of chemisorbed state(s) of the phosphonic acid group with the hydroxylated aluminum surface due to increased hydrolysis rates of the ester bond [32, 64].

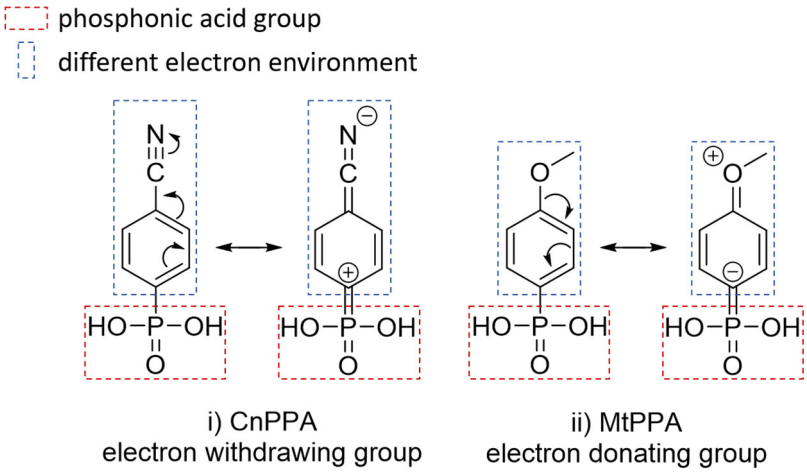

Figure 1.4. *Electron delocalization of phosphonic acid molecules with different electron environment: i) (4-cyanophenyl)phosphonic acid (CnPPA) with electron-withdrawing group, which decreases the electron density of phosphonic acid group; ii) (4-methoxyphenyl)phosphonic acid (MtPPA) with electron-donating group, which increases the electron density of phosphonic acid group*

1.3.2. Thesis Outline

Based on different stages of PA surface treatment, this thesis firstly starts with two chapters:

Chapter 3. In situ study of the dynamic charges and species transfer on aluminum surface in acidic PA aqueous solution (pH≈2). In this chapter, the effects of PA molecular structure on the steady state competing processes of aluminum dissolution, ionic interaction of aluminum-phosphonate complexes precipitation, and PA molecule physisorption/chemisorption on the aluminum surface are studied. Specifically, two adsorption modes of PA molecules on the aluminum surface are investigated in detail. This chapter shows that the increased PA steric effect decreases the aluminum dissolution process by the enhanced adsorption mode from physisorption

to unstable/stable chemisorption. Moreover, a molecular electron withdrawing effect destabilizes the chemisorption, while a molecular electron donating effect stabilized the chemisorption.

Chapter 4. Ex situ surface characterization of the final PA modified aluminum oxide. After the adsorption process in Chapter 3, PA modified aluminum surface is rinsed by H_2O in air and characterized by XPS. This chapter systematically investigates the PA molecular structural effect on adsorbate PA layer and final adsorbent aluminum oxide. Specifically, a novel robust concept is introduced to describe the stratified structure of adsorbate PA layer and adsorbent aluminum oxide, namely stratification factor. This chapter shows that with the increase of PA steric effect, a PA layer with a higher stratification factor is formed on a thinner aluminum oxide surface. However, the PA molecular electron environment effect is insignificant on the final formed aluminum oxide surface.

Note that there is a transition stage, i.e. H_2O-rinsing and air-exposure, between PA dynamic adsorption stage (Chapter 3) and the final stage PA modified aluminum oxide surface (Chapter 4) as illustrated in Figure 1.5.

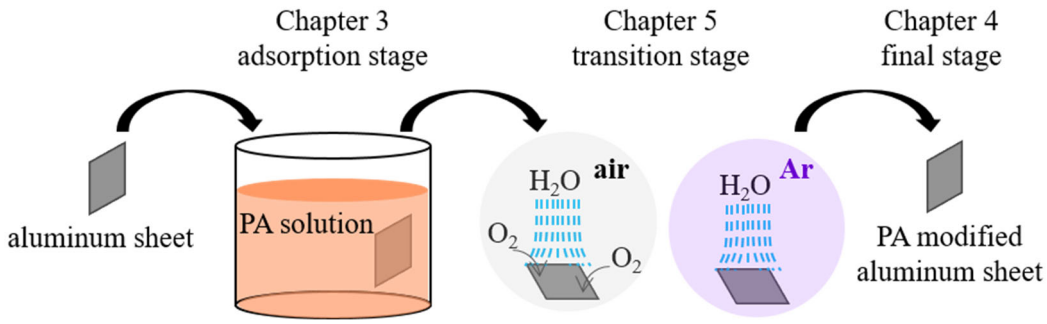

Figure 1.5. *Illustration of three stages of a complete phosphonic acid (PA) surface treatment process on aluminum sheets. Chapter 3 studies the dynamic PA adsorption process on aluminum surface. Chapter 5 studies the transition stage of the re-oxidation process of PA modified aluminum surface in air and in argon (Ar) atmosphere. Chapter 4 studies the final PA modified aluminum oxide surface.*

This transition stage firstly stops the aluminum dissolution process by H_2O neutralization. Synchronously, H_2O rinsing also removes the majority of physisorbed species, i.e. aluminum-phosphonate complexes on surface. Meanwhile, the air-exposure generates an aluminum re-oxidation process, which oxidizes the PA modified aluminum surface as well. It is necessary to investigate the effect of re-oxidation during the transition stage on the final stage of PA modified aluminum oxide surface. Because this re-oxidation process might be essential to stabilize an unstable PA modified aluminum surface that is problematical for the next step industrial application, e.g. polymer coating and adhesive applying.

Thus, a glovebox is employed to control this re-oxidation process. A setup coupling a glovebox and together with X-ray photoelectron spectroscopy (XPS) was previously used for air sensitive material surface characterization [65-69]. However, it was barely used for aluminum oxide surface modification since aluminum oxide is stable at neutral environment. Nevertheless, the aluminum oxide stability during the prior adsorption process depends on the PA molecular structure[32, 70, 71]. The effect of re-oxidation process on the final PA modified oxide surface is unknown. Thus, it is important to compare the stability of PA modified aluminum oxide during the transition state in the O_2 controlled environment. This study is highly industrial relevant since it directly relates to the choice of different PA molecular structures for certain application environment: during the transition stage, a self-stabilized PA modified aluminum oxide fits well to a continues oxygen-limited production line; while an unstable PA modified aluminum oxide needs an additional stabilization period.

Chapter 5. The transition state of PA modified aluminum oxide surface is studied using a set up consisting of glovebox, XPS/ hard X-ray photoelectron spectroscopy (HAXPES) chamber, and ultra-high vacuum (UHV) connection system. With this set up, XPS/HAXPES characterization provides an in situ information on surface without further oxidation and contamination from air-exposure. The stability of PA modified aluminum oxide during the transition state is investigated by using two PA molecules with opposite electron environments to modify aluminum oxide surface in glovebox, namely CnPPA and MtPPA as shown in Figure 1.3. Prior to this transition state, CnPPA creates an unstable chemisorption on aluminum surface, while MtPPA passivates the aluminum surface via a stable chemisorbed state as stated in Chapter 3. Meanwhile, the effect of re-oxidation process during the transition state is compared by carrying on PA treatments in glovebox and air. This chapter shows that MtPPA modified aluminum oxide stabilized itself via strong chemisorbed PA layer during the transition state; while CnPPA modified aluminum oxide surface needs additional re-oxidation process in air to stabilize its modified surface.

From Chapter 3, Chapter 4 and Chapter 5, the PA molecular structural effects on aluminum oxide surface modification on three stages, i.e. dynamic adsorption stage, PA modified oxide transition stage and final stage of PA modified oxide, have been systematically study respectively. These fundamental understandings cover the whole process of PA surface treatment on metal surface.

With the current study, a systematical stepwise understanding of PA molecular structure effect on PA surface treatment of aluminum oxide at different stages is established. Meanwhile, this

work also provides a few novel robust characterization methodologies to describe in situ/ex situ PA adsorption behavior, e.g. relative inhibition factor and stratification factor. This work establishes a platform for further studies using other PA molecules and aluminum alloys.

Chapter 2. Experimental Methods

2.1. In Situ Adsorption Process Monitoring

2.1.1. Phosphonic Acid Solution Preparation

Nine PA molecules, as displayed in Chapter 1, Figure 1.3, are commercially available and were used as received: namely, phosphonic acid (Sigma, 99%), methylphosphonic acid (Abcr, 98%), ethylphosphonic acid (Abcr, 98%), tert-butylphosphonic acid (ACROS, 98%), benzylphosphonic acid (ACROS, 98%), (2-phenylethyl)phosphonic acid (Abcr, 95%), phenylphosphonic acid (Sigma, 97%), (4-methoxyphenyl) phosphonic acid (Abcr, 95%) and (4-cyanophenyl)phosphonic acid (Abcr, 98%). The solutions were prepared using MilliQ water (18.2 MΩ·cm, Merck) and stored in polypropylene tubes. For each molecule, 0.01 M solution of PA was prepared and the pH of the prepared solution was determined; it varied from pH=2.2 to pH=2.5 as shown in appendix A Table A.1.

2.1.2. Aluminum Surface Pretreatment

A commercially available aluminum sheet (Constellium-Singen, 99.9%, 0.5 mm) was cut into 8.7×13.7 mm^2 pieces; manually polished with 4000 grit sandpaper; then cleaned with acetone, ethanol and H_2O in an ultrasonic bath each for 10 min. The aluminum sheet was then dried with Argon flow and stored in a wafer shipper. To obtain a reproducible oxidized aluminum surface before any experiment, the stored aluminum sheet was firstly etched in 5 mL 5 wt% NaOH (Sigma-Aldrich, ≥ 97.0 %) solution for 1 min. The NaOH etched aluminum samples were then rinsed with MilliQ water and dried by an Argon flow, as shown in Figure 2.1(i).

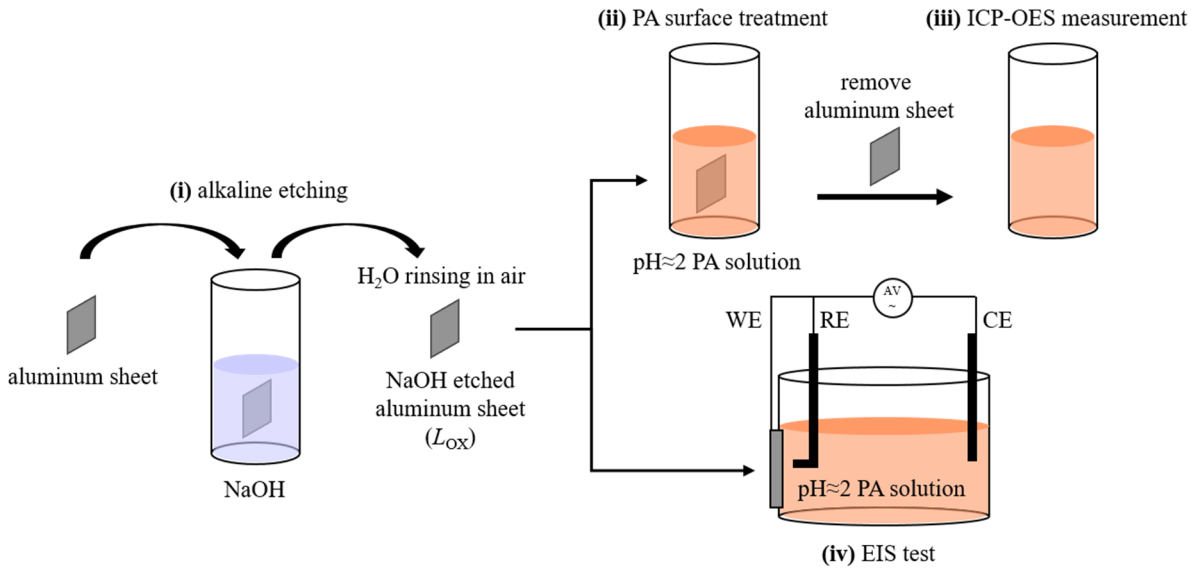

Figure 2.1. *Sketch of the experimental procedure to study the aluminum dissolution/ PA adsorption. (i) alkaline etching is the aluminum surface pretreatment prior to PA surface treatment. Then the NaOH etched aluminum sheet (Lox) is immersed in PA solution (ii) for different durations followed by ICP-OES elemental analysis (iii) to determine aluminum concentration in the residual PA solution. Lox is also mounted on the electrochemical cell for the EIS test (iv) to measure the aluminum surface impedance in PA solution.*

2.1.3. Phosphonic Acid Surface Treatment

The pretreated aluminum sheet was then directly immersed in 5 mL acid solution for different durations (5 min, 15 min, 60 min, 120 min, and 240 min) at room temperature in a polypropylene tube, as shown in Figure 2.1(ii). The aluminum sheet was then removed from the polypropylene tube for rinsing (MilliQ water) in air and subsequent drying with Ar flow. The residual acid solution (5 mL) in the polypropylene tube was collected for elemental (aluminum) concentration analysis, as shown in Figure 2.1(iii). Each of the treatment condition (i.e. different PA molecules and immersion time) was repeated three times.

2.1.4. Elemental Analysis

To dissolve any possible aluminum-phosphonate salt sediments for quantification, 1 ml of H_3PO_4 (Sigma-Aldrich, ≥85%) was added to the residual PA solution. An inductively coupled plasma-optical emission spectrometer (ICP-OES), Optima 3000 ICP-OES (PerkinElmer AG, Rotkreuz, Switzerland), was used to quantify the amount of aluminum dissolved into the treatment solution. The ICP-OES calibration was performed using blank solutions and matrix-matched multi-element standard solutions in a concentration range from 0.02 to 10 mg/L.

2.1.5. Electrochemical Impedance Spectroscopy (EIS)

The EIS experiment was carried out at open-circuit potential (OCP) in a 50 mL electrochemical cell with a ≈0.2 cm^2 electrode area. A classical three electrodes setup with an Ag/AgCl reference electrode (Metrohm AG, Swizterland) and a platinum counter electrode was used. The measurements were performed with a Metrohm-Autolab PGSTAT30 system (Metrohm-Autolab, Switzerland). After the NaOH surface pretreatment, the aluminum sheet was directly mounted (pressed laterally against an O-ring) on the electrochemical cell, as shown in Figure 2.1(iv). For each PA solution, a triplicate measurement was performed. The results were highly reproducible for each type of PA molecule and for simplicity, one selected plot has been presented. An alternating voltage U(f)=10 mV was applied between the reference electrode and the working electrode (aluminum surface). The EIS experiment consists of a frequency scan from 100 kHz down to 2 mHz with the electrochemical current, I(f) recorded. The impedance$(f) = \frac{I(f)}{U(f)}$ is then calculated. This frequency-dependent complex impedance can be compared to an equivalent electronic circuit to gain physically quantitative insights. This analysis started with an equivalent circuit model that is well-established for a polymer coated-metal in a corrosive media[72] (Figure 2.2) and added two modifications: the first modification allows modeling interface heterogeneity in form of porous insulating cover layers. It is adopted from a previous work that used this approach to fit porous adsorbed polymer layers[73, 74]. The second modification allows inclusion of changes at the interface that are apparent at low frequency (LF). Such changes are physically linked to morphological changes at the interface that are caused by bipolar resonances occurring in the small electrical field applied by EIS and related to the presence of partially mobile surface ionic species. This aspect is usually not implemented in classical EIS analysis software, so in order to attain the necessary mathematical flexibility a custom fitting software in Labview environment was programmed. The fitting argument was defined as the (complex absolute) difference between measured and calculated circuit impedance. Variations of the circuit values and enabled coefficients was done in manual iterations and in the direction to minimize the fitting argument on the entire frequency range. This semi-automated approach was necessary to avoid physically inappropriate solutions with this partially determined model.

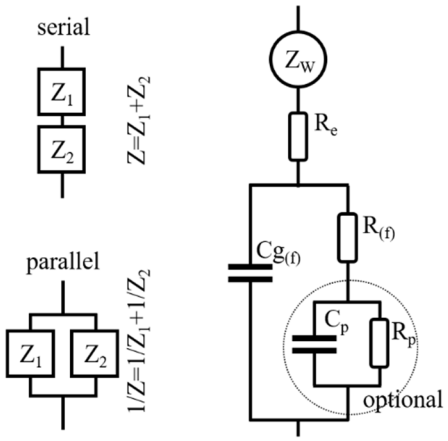

Figure 2.2. *equivalent electrical circuitry used for data fitting, including diffusion related Warburg impedance (Z_W), solution resistance (R_e), frequency dependent geometric interface capacitance ($Cg_{(f)}$), frequency dependent interface- or charge transfer resistance ($R_{(f)}$), and optional interface heterogeneity, modeled by a discrete R_p&C_p element.*

Figure 2.2. displays the equivalent circuit used for our fitting analysis; it includes the $\frac{(1-j)}{\sqrt{\omega}}$ Warburg impedance element to model the long-range diffusion of ions[75], as well as a customized frequency-dependent interface resistance($R_{(f)}$) and interface capacity ($Cg_{(f)}$). In order to capture changes of LF-impedance without introducing meaningless fitting features at higher frequency, the fitting functions are defined by an array of coefficients (C_i) and asymptotically convergence towards higher frequency. The frequency-dependent elements are thus mathematically represented in the form: $R_{(f)}\ or\ Cg_{(f)} = \sum_i \frac{C_i}{a(f)^i}$, where $a(f) = \log(f) + 4$. The coefficients C_i were fitted in semi-automatic iterations and values reproducing to a good visual fit are listed in the Appendix A, Table A.3. The optional parameters C_p, R_p were only enabled in the model if absolutely required to reproduce the overall shape of the curves. The simulation and fitting algorithm were programmed by Prof. Dr. Manfred Heuberger.

2.1.6. Computational Details

Density functional theory (DFT) calculations were carried out using the DMol3 module in Materials Studio 2018[76]. The geometries of molecules were optimized using a functional B3LYP with the DNP 3.5 basis set, which predicts comparable geometries as accurately as the Gaussian basis sets do[77]. Several chemical descriptors were calculated based on the molecular electron properties computed at the same level theory, including vertical ionization potential (IP), vertical electron affinity (EA), and electronegativity (χ), by using the following equa-

tion[78]: $\chi = (IP + EA)/2$. The energy gap (ΔE) is also calculated from the energy difference between highest occupied molecular orbital (HOMO) and lowest unoccupied molecular orbital (LUMO)[79]: $\Delta E = E_{HOMO} - E_{LUMO}$. The DFT calculation was supported by Jiuke Chen

2.2. Ex Situ Surface Characterization

2.2.1. Sample Preparation and Surface Treatment

The aluminum sheet alkaline pretreatment and the PA surface treatment were described in section 2.1.2 and 2.1.3 respectively. The experimental procedure is also illustrated in Figure 2.3 After PA surface treatment, the PA modified aluminum was immediately rinsed by MilliQ water in air (Figure 2.3 iv), subsequently dried in an argon flow and then stored in a wafer shipper under the argon atmosphere (Figure 2.3 b) for XPS surface characterization (Figure 2.3 v).

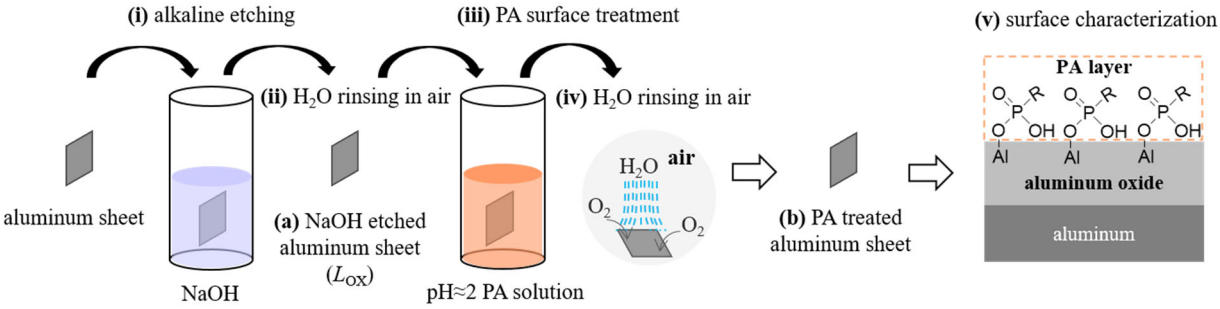

Figure 2.3. *Sketch of the experimental procedure for the phosphonic acid (PA) treatment of an aluminum sheet and surface analysis, consisting of the following sequential steps: (i) alkaline etching in NaOH followed by (ii) rinsing by MilliQ water in air and subsequent drying with argon flow. The thus obtained predefined oxide layer on the aluminum surface is further denoted as (a) LOX and was also characterized by XPS. (iii) PA surface treatment of LOX at pH ≈ 2 solution, followed by (iv) rinsing by MilliQ water in air and subsequent drying in argon flow. (b) The final PA modified aluminum oxide is stored in an argon desiccator. (iv) XPS analysis of the PA modified aluminum oxide.*

To improve the mass resolution of the ToF-SIMS analysis, the aluminum samples were mechanically polished to obtain a mirror finishing surface and then electro-polished in a perchloric acid solution at 8 V for 400 s at room temperature. Subsequently, the aluminum samples were rinsed with MilliQ water, dried with Argon flow and stored in the wafer shipper. The polished sheets were then treated with PA solutions, as described in section 2.1.3. The followed sample reparation for ToF-SIMS analysis is same as XPS mentioned above.

2.2.2. Surface Analysis by XPS and ToF-SIMS

XPS surface analysis was performed with a Physical Electronics (PHI) Quantum 2000 X-ray photoelectron spectrometer using monochromatic AlK_{α} radiation and a hemispherical analyzer, as equipped with a channel plate and a position-sensitive detector. The anode is operated at 15 kV and 28.8 W with an analyzed sample area of about 150 μm in diameter. All data was collected at an electron take-off angle of 45° with the analyzer operating in the constant pass energy mode. Survey spectra over the binding energy (BE) range from 0 to 1200 eV were acquired at a constant pass energy of 117.4 eV. Detailed spectra of the C 1s, O 1s, Al 2p, P 2s and upper valence band regions were recorded at a pass energy of 46.95 eV, resulting in an energy resolution of 0.95 eV (as determined from the width of the Ag 3d5 peak). The P 2p signal has an interference with a plasmon originating from the neighboring Al 2s peak (in the binding energy range from 128.4 eV to 138.6 eV). Therefore, the P 2s peak was used for quantification. Elemental concentrations were calculated in atomic percent using the Shirley-background corrected integrated peak areas (as resolved after peak fitting using the Multipack software), while assuming a homogenous distribution of elements in the solid and applying the built-in PHI sensitivity factors provided by the equipment manufacturer. Only the O1s sensitivity factor was adapted to match the stoichiometric ratio of Al_2O_3 as measured for a sapphire reference.

ToF-SIMS analysis of a selected number of PA-treated samples were performed on a ToF-SIMS.5 from IONTOF GmbH, Germany, using a $Bi3^{2+}$ beam with an energy of 25 keV and a cycle time of 100 μs. An area of 500 x 500 μm^2 was scanned 50 times with a resolution of 128 x 128 pixels.

2.3. In Situ Surface Characterization

This setup consists of a custom designed UHV (10^{-9} mbar) transfer system used to connect the sputter chamber, glovebox, and XPS/HAXPES chamber as illustrated in Figure 2.4. With this experimental set up, the oxidation and contamination are limited to the minimum level.

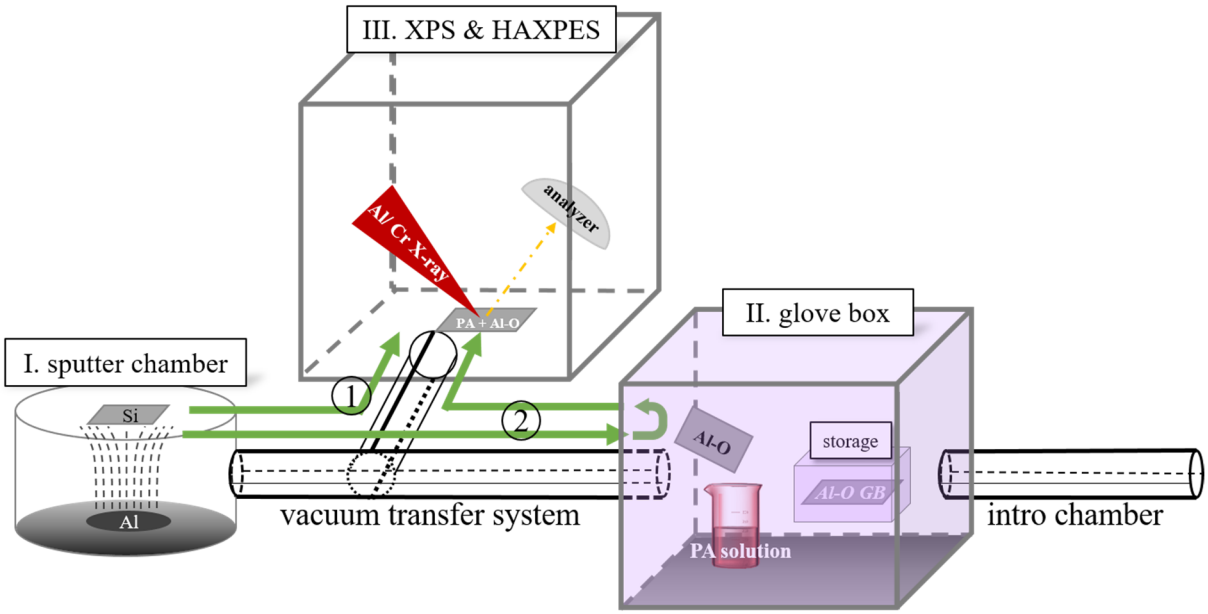

Figure 2.4. *Aluminum substrate production at I. sputter chamber, PA surface treatment in II. glovebox and surface characterization at III. XPS (X-ray photoelectron spectroscopy) & HAXPES (Hard X-ray photoelectron spectroscopy) chamber are connected via a vacuum transfer system to avoid oxidation/contamination in air; a vacuum intro chamber is used to transfer samples from air.*

Glovebox (noted as GB) is connected with a vacuum intro chamber to transfer samples from outside (in air), and an internal vacuum transfer system. The glovebox is filled with argon gas, where the O_2 concentration is controlled c.a. 0.01 ppm; H_2O concentration is controlled c.a. 0.01 ppm. However, during the PA surface treatment in the GB, the O_2 concentration increased up to maximum 0.05 ppm, and H_2O concentration increased up to maximum 20 ppm due to the PA solution evaporation.

2.3.1. PA Solution Preparation

(4-cyanophenyl)phosphonic acid, namely CnPPA, (Abcr, 98%) and (4-methoxyphenyl)phosphonic acid, namely MtPPA, (Abcr, 95%) were used as received. 0.01 M PA solution was prepared using MilliQ water (18.2 MΩ·cm, Merck) in a centrifuge tube. For treatments inside glovebox, PA solutions were deaerated with an argon flow for 60 min; then the deaerated PA solution was sealed by a Parafilm and transferred in glovebox immediately. For treatments in air, the PA solutions were directly used after the preparation.

2.3.2. Aluminum Substrate Preparation (Sputter Chamber)

To increase the sensitivity and reproducibility of surface characterization, physical vapor deposition (PVD) is used to obtain a fresh atomic flat aluminum layer on silicon wafer surface

(10×10 mm^2). Aluminum layers of 500 nm thickness were grown by DC magnetron sputtering in an ultra-high vacuum (UHV) chamber with base pressure lower than 5 x 10^{-9} mbar. The films were grown on Si (001) substrates that have 90 nm of a-Si_3N_4 on top (to prevent any intermixing or diffusion at the interface). The following deposition parameters have been used: 80 W Al gun power, 0.5 Pa Ar pressure. Samples after deposition were directly transferred into the glovebox for surface treatment via a vacuum transfer system. The PVD deposition was supported by Dr. Cancellieri Claudia.

2.3.3. Reference Aluminum Oxide/Hydroxides

Crystalline aluminum oxide/hydroxide

α-Al_2O_3 (sapphire) [0001] was purchased from Crystec, Germany. Before the surface characterization, sapphire was ultrasonically cleaned in ethanol and isopropanol each for 10 min. α-$Al(OH)_3$ (Bayerite) was synthesized at lab. Aluminum sheets (99.9%, Raffinal) were polished with 2500 grit sandpaper and ultrasonically cleaned in MilliQ water for 5 min. Subsequently, for Bayerite synthesis, aluminum sheets were immersed in 100 mL and 50 ℃ MilliQ water for five days. Eventually, aluminum sheet was dried by Ar flow, and the crystal orientation was checked by X-ray diffraction (XRD). The XRD characterization results are in Appendix C, Figure C.1. Then the reference crystalline samples were stored in glovebox. The synthesis of Bayerite was supported by Dr. Guseva Olga.

Amorphous Aluminum Oxides/Hydroxide

The native amorphous aluminum oxides/hydroxide are created by exposing PVD aluminum into different environments. A native aluminum oxide formed on PVD aluminum surface is created by storage of fresh PVD aluminum in glovebox for 10 min, namely "Al-O GB", as illustrate in Figure 2.4, green arrow ②. The other native aluminum oxide is formed by transfer PVD aluminum out of glovebox and exposure in air for 10 min, namely "Al-O air". Additionally, "Al-O GB" was dipped into pure H_2O for 5 min in glovebox and followed drying procedure in vacuum to create an aluminum hydroxide surface, namely "H_2O+Al-O GB".

2.3.4. PA Surface Treatment

For the PA treatment in the glovebox, a stored in glovebox PVD aluminum substrate (Al-O GB) was dipped into PA solution for 5 min, subsequently rinsed by H_2O for three times. Due to the limitation of sample handling in glovebox, instead of drying sample by Ar flow, the H_2O

rinsed sample was stored in a vacuum chamber (10^{-9} bar) for 30 min to dry the residual H_2O on surface, as illustrated in Figure 2.4, green line②. The CnPPA and MtPPA treated aluminum oxide in glovebox is named "Al-O+CnPPA GB" and "Al-O+MtPPA GB" respectively. For the PA surface treatment in air, a fresh PVD aluminum substrate was firstly removed out of glovebox. Then the PVD aluminum substrate was dipped into PA solution for 5 min, followed with three times H_2O rinsing and Ar flow drying in air. Afterwards, the treated sample was transferred back into glovebox ready for surface characterization. The CnPPA and MtPPA treated aluminum oxide in air is named "Al-O+CnPPA air" and "Al-O+MtPPA air" respectively. Each PA treatment condition was repeated for three times. Abbreviations of these PA modified aluminum oxides are listed in Table 2.1.

Table 2.1. The summary of the abbreviations of reference native amorphous aluminum oxide and PA modified aluminum oxide. Additionally, a metallic PVD Al sample is also listed here created in ultra-high vacuum (UHV).

surface treatment	abbreviation
direct transformation of a PVD Al sample from sputter chamber to XPS/HAXPES surface characterization via UHV transfer system	Metallic Al
storage of a PVD Al sample in glovebox	Al-O GB
exposure of a PVD Al sample in air	Al-O air
immersion of a "Al-O GB" in a deaerated H_2O in glovebox	Al-O+H_2O GB
CnPPA modified PVD Al sample in glovebox	Al-O+CnPPA GB
CnPPA modified PVD Al sample in air	Al-O+CnPPA air
MtPPA modified PVD Al sample in glovebox	Al-O+MtPPA GB
MtPPA modified PVD Al sample in air	Al-O+MtPPA air

2.3.5. HAXPES/XPS

The PA modified PVD aluminum oxides and reference aluminum oxide/hydroxides (crystalline and amorphous structure) were quantitatively evaluated by X-ray photoelectron spectroscopy (XPS) and hard X-ray photoelectron spectroscopy (HAXPES). Analysis using HAXPES and XPS was performed with a PHI Quantes spectrometer (ULVAC-PHI, Japan) equipped with a conventional Al-Kα X-ray source (1486.6 eV) and a high energy Cr-Kα (5414.7 eV) X-ray source. Both sources are high flux focused monochromatic X-ray beams that can be scanned across the sample surface selected area. All data was collected at an electron take-off angle of

45° with the analyzer. The energy scale of the hemispherical analyzer was calibrated according to ISO 15472 by referencing the Au 4f7/2 and Cu 2p3/2 main peaks (as measured in situ for corresponding sputter-cleaned, high-purity metal references) to the recommended binding energy (BE) positions of 83.96 eV and 932.62 eV, respectively. Charge neutralization during each measurement cycle was accomplished by a dual beam charge neutralization system, employing low energy electron and Ar ion beams (1 V bias, 20 mA current). The core level measurements with both sources were performed in high-power mode. The electron beam is scanned to deconcentrate heat dissipation; hence, the analysis is performed along a line 1.4 mm long. The step size and pass energy for core level measurements were 0.13 eV and 69 eV respectively, for both sources (surveys were acquired at 280 eV pass energy and 0.5 eV step)[80]. XPS measured detailed spectra of the C 1s, O 1s, Al 2p, P 2s, O KLL, upper valence band regions and HAXPES measured detailed spectra of C 1s, O 1s, Al 2p, P 1s, O KLL, Al KLL were recorded at pass energy of 69 eV and 0.13 eV step. The metallic Al 2p peak is taken as reference at 73 eV [81]and all the energy scales are shifted accordingly. When Al metallic peak is not available (like in crystal aluminum oxide/hydroxides), alignment of the energy scale has been done using the C1s peak at 286.2 eV. The atomic concentrations were calculated from the peak areas after Shirley background subtraction using the predefined sensitivity factors in the MultiPak 9.9 software provided by ULVAC-PHI. The XPS/HAXPES measurement was supported by Dr. Cancellieri Claudia.

Chapter 3. Two Steady State Adsorption Modes of Phosphonic Acids on Aluminum Surface

The following results of this chapter were published as a research article: Zhao R, Schmutz P, Jeurgens L P H, Chen J, Gooneie A, Ott N, Gaan S, and Heuberger M. ACS Applied Materials & Interfaces, 2022, 14(34): 39467-39477. The major part of this work was done by Zhao R. Schmutz P and Ott N supervised the electrochemical measurement. Heuberger M programmed the fitting algorithm of electrochemical impedance test results. Chen J and Gooneie A did the density function calculation of phosphonic acid molecules. Gaan S, Schmutz P, Jeurgens LPH, and Heuberger M contributed to the discussion and further correction of this paper.

The critical challenges of aluminum surface treatment by phosphonic acid (PA) have been stated in Chapter 1. Facing these challenges, this chapter investigates the charges and species transfer processes on the aluminum surface in the phosphonic acid (PA) solution including aluminum dissolution, precipitation of aluminum-phosphonate complexes and PA adsorption/ desorption. To explore these dynamic processes on the electrochemically unstable aluminum surface, techniques such as inductively coupled plasma-optical emission spectrometry (ICP-OES) and electrochemical impedance spectroscopy (EIS) are employed. The PA molecular steric and electron environment effects are systematically compared. Firstly, theoretical charges and species transfer rating modes on the aluminum surface in the acidic PA solution (pH≈2) are established. Then a steady state aluminum dissolution/ PA adsorption is observed by ICP-OES, which shows a constantly increasing rate of aluminum concentration as a function of time. Meanwhile, it also indicates the PA molecular structural effect on the efficiency of aluminum dissolution inhibition. In parallel, detailed EIS study distinguishes the two steady state adsorption modes of PA molecules on aluminum surface, i.e. dissolution limiting physisorption, and unstable/ stable chemisorption. Based on the understanding of fundamental relationships among PA molecular effects, the steady state interface morphology as well as the steady sate aluminum dissolution rate, a more differentiated molecular structure related description of the aluminum dissolution inhibition of PA molecules via molecular DFT calculations are carefully discussed in the end of this chapter.

3.1. Results and Discussion

3.1.1. Charges and Species Transfer Rate Model

The air-exposed aluminum surface is covered with a nanometer thick native aluminum oxide/hydroxide whose structure depends on its environmental exposure history. Thus, a pretreatment process involving an alkaline (NaOH) etching was performed on the aluminum samples to get a reproducible thin[82] aluminum oxide/hydroxide surface (L_{OX}) before the phosphonic acid (PA) treatment. Then the aluminum surface undergoes a series of changes during the PA treatment.

Owing to the low pH of the considered solution, it is expected that the thin fresh aluminum oxide is dissolved firstly then metallic aluminum substrate continues to dissolve into the acidic PA solution. The here used in-situ experimental methods are not sensitive to detect the transition of fresh aluminum oxide dissolution to metallic aluminum dissolution. This missing information is discussed in Chapter 4. Thus, in the following discussion and for pure simplicity, the dissolution of the initial L_{OX} film is not taken into account. The aluminum surface during the PA treatment undergoes a series of transformations, which are illustrated in a simplified mechanism shown in Figure 3.1. Together with the covalent binding between PA and aluminum[56], these mechanisms give rise to a dynamic aluminum-PA solution interface with a rate balance among aluminum dissolution with low-soluble complex formation (**A**), PA physisorption/desorption (**B**) and PA chemisorption (**C**).

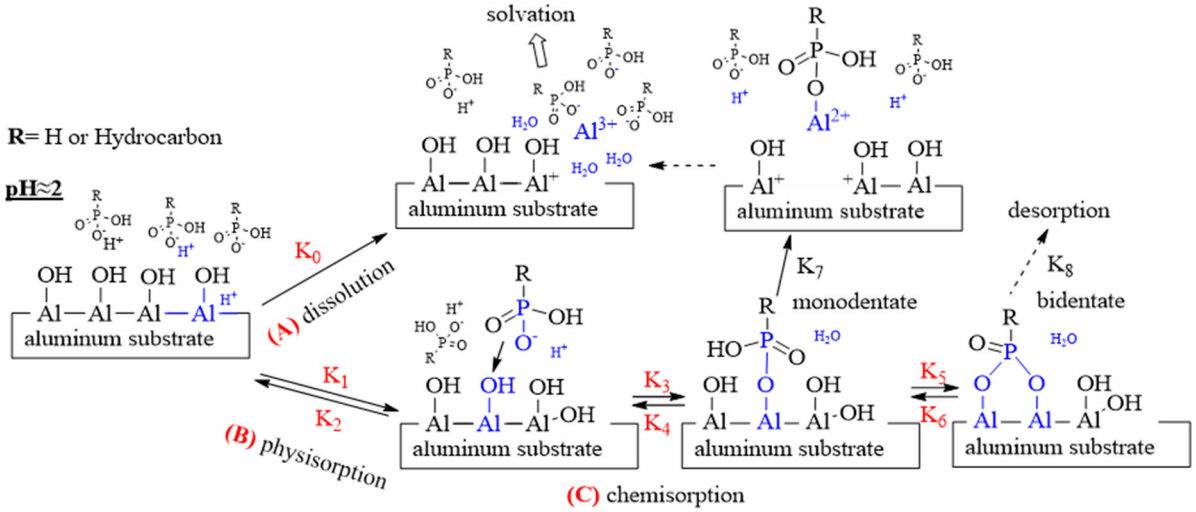

Figure 3.1. *Simplified rate model of charges and species transfer on the aluminum surface in pH≈2 phosphonic acid (PA) solution. The main processes involve (A) aluminum dissolution with aluminum-phosphonate complex solvation, (B) PA physisorption on the surface, and (C)*

chemisorption of PA on the surface. This model distinguishes between monodentate and bidentate chemisorption.

The aluminum dissolution (Figure 3.1(A)) in the PA solution (pH≈2) starts with the attack of the Al-Al bonds by hydronium (H_3O^+) and initially leads to formation of aluminum-phosphonate salt complexes. A rate constant K_0 is assigned for this step. The physisorption (rate constants K_1, K_2) of PA molecules is controlled by Van der Waals and ionic PA-aluminum surface interactions. The surface proximity and mobility of the physisorbed state helps to initiate the energetically more stable chemisorption (K_3, K_4). Once a PA molecule is chemisorbed in the monodentate state, it can be further transformed into the bidentate chemisorbed state (K_5, K_6). Depending on steric and binding energetics, direct dissolution of monodentate aluminum-phosphonate complexes via hydrolysis is possible (K_7); meanwhile, dissolution of bidentate compounds is energetically less likely (K_8). It is also expected that there is an excess accumulation of physisorbed ionic complexes at or near the interface due to their low solubility.

The number of aluminum reactive sites available on surface is noted as N. In this pH≈2 solution, a non-equilibrium environment exists, since any attractive/binding interactions between PA molecules and aluminum slow down aluminum dissolution, which means $K_0>K_7>K_8\approx0$; in the rate model, the number of aluminum sites that can be dissolved is denoted as N_D. The physisorption (Figure 3.1(B)) of PA molecules on the aluminum surface covers some of these reactive sites and moderates aluminum dissolution; the number of hence dynamically protected sites is referred to as N_P. In absence of chemisorption (i.e. $K_3=0$) a steady state is reached as follows:

when $K_1/K_2<1$, then $N_P \ll N_D$, aluminum is dissolved at a high rate; on the other hand, when $K_1/K_2>1$, the aluminum dissolution rate is reduced by physisorbed species and the steady state interface can be characterized by $\frac{N_P}{N_D} \cong \sigma \cdot \frac{K_1}{K_2}$, where σ is the effective number of aluminum atoms kinetically protected by adsorbed PA molecules. As a result, the steady state aluminum dissolution rate is directly related to the inhibition efficiency of the PA molecules with an inhibition factor, ω, defined as $\omega \propto \frac{N_P}{N_D} \propto {K_0}^{-1}$.

In the presence of chemisorption (Figure 3.1(C)), the situation is significantly changed; namely, when $1\leq K_1/K_2< K_3/K_4$, the physisorbed PA will mostly transform into chemisorbed PA. Aluminum sites protected by chemisorbed PA shall be denoted as N_{C1} (monodentate) and N_{C2} (bidentate); Since the chemisorption of PA proceeds via covalent interaction with aluminum surface, the chemisorption process can have a higher protective effect and hence reduces

aluminum dissolution rates even more, comparing to physisorption alone. In the limiting case for strong bidentate adsorption ($K_5/K_6>>1$) and negligible direct desorption of chemisorbed species ($K_7 \approx K_8 \approx 0$), it then follows: $\frac{N_{C2}}{N_D} \cong \sigma \cdot \frac{K_1}{K_2} \cdot \frac{K_3}{K_4} \cdot \frac{K_5}{K_6}$. In this case where most steady state adsorbed PA is linked to the aluminum surface via bidentate binding mode, the maximum inhibition factor, ω, can be expressed as $\omega \propto \frac{N_{C2}}{N_D} \propto {K_0}^{-1}$.

This "limiting case" discussion illustrates how effective a reaction cascade of (Figure 3.1(B)) and (Figure 3.1(C)) can chiefly populate the chemisorbed states and hence dynamically reduce the aluminum dissolution rate to negligible values, albeit never reaching zero.

The population of physisorbed phosphonic acid, N_P, is a thermodynamic prerequisite for a more stable chemisorption (N_C) with a covalent binding strength that is affected by the phosphorus electron environment. The steady state number-ratio between physisorbed and chemisorbed states is principally determined by K_3/K_4.

In addition, PA can form a bidentate chemisorbed state at a ratio K_5/K_6 relative to the monodentate state. It is important to note that both, monodentate and bidentate states can probably directly desorb in form of bivalent or monovalent Al^{1+} and Al^{2+} salt complexes. This mechanism is included in the rate model via rate constants K_7 and K_8. Due to adsorption energetics, it is expected that the general case is $K_7>K_8\approx 0$, and for hydrocarbon substituents (R) of PA molecules a steric effect is expected that specifically alters K_4 and K_7.

Shortly after the immersion of the aluminum sheet into the pH≈2 PA solutions, phosphonic acid molecules directly react with a hydrolyzed aluminum surface, which defines time $t_0=0$. According to the rate model (Figure 3.1), the aluminum dissolution rate is initially high and the population of physisorbed and chemisorbed states is low. Due to the multi-step adsorption cascade, the bidentate chemisorbed state has the longest time constant to reach steady state population. A steady state can be defined as an asymptotic state when aluminum dissolution rate and populations of physisorbed and chemisorbed states no longer change with time (see Appendix A, Figure A.1). Numerical time-integration simulation (Figure A.1) was performed to illustrate how this transition towards steady state occurs, in presence of physisorption with and without the possibility to ensue monodentate or bidentate chemisorption. Figure A.1 clearly demonstrates how chemisorbed states, if they exist, are predominantly populated at steady state. It is worth noting that due to the adsorption cascade, the bidentate chemisorbed state has the longest time constant to reach steady state population but nevertheless, its population can actually dominate at steady state.

3.1.2. Aluminum Dissolution Inhibition

It was experimentally verified that the aluminum dissolution rates are indeed constant as expected for a steady state scenario. Figure 3.2a) displays the aluminum elemental concentration in the PA solution as a function of time, as determined from ICP-OES. The experimental data is listed in the supporting information Table A.2. The linear slopes fitted to these data points indicates constant aluminum dissolution rates (K_0), which significantly vary with molecular structure, as listed in Table 3.1. The linear fitting demonstrates that during the treatment, steady state conditions are maintained for at least 240 min. This important finding strongly supports the steady state assumption raised by the simplified rate model earlier in this section. It is also worth noting that the steady state rates actually vary over more than two orders of magnitude between the different types of phosphonic acids studied in this work, which strongly supports the multi-step adsorption nature.

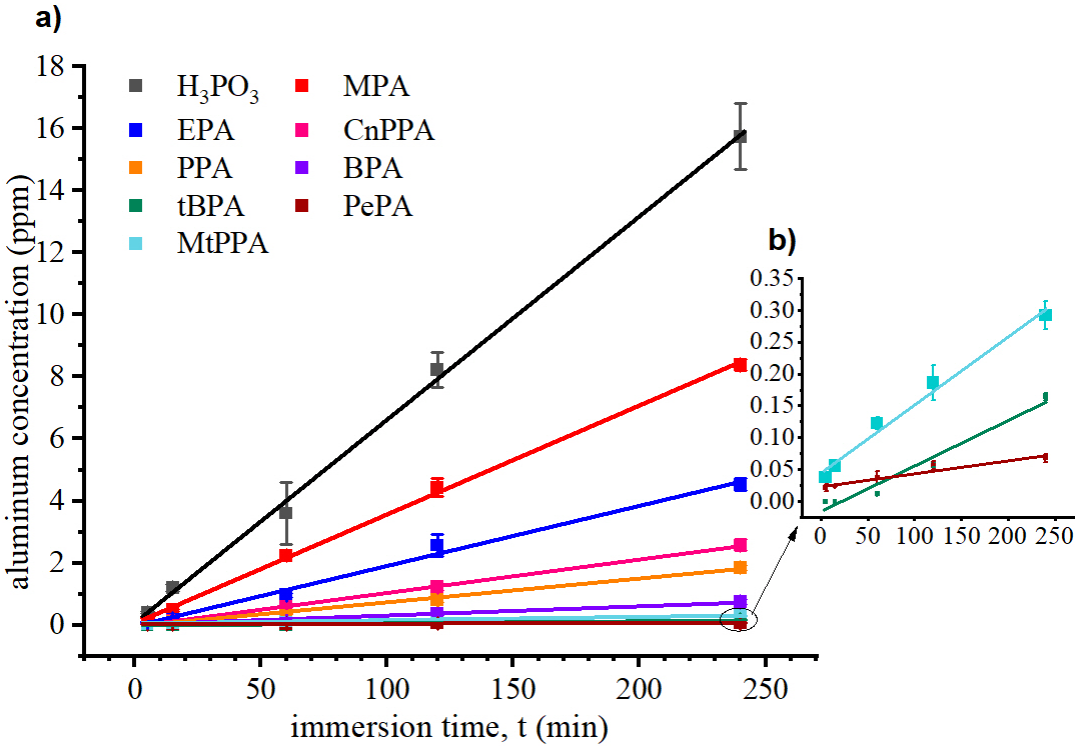

Figure 3.2. *ICP-OES measurement of supernatant aluminum concentration as a function of immersion time, where the experimental data are presented with symbols and error bars and the line shows the linear on; a) phosphonic acid molecules with low, medium and high dissolution inhibition; b) enlarged caption for tBPA, MtPPA and PePA with high dissolution inhibition.*

Although a detailed discussion about the effect of different PA molecules will follow later, it is obviously noted from the rates (i.e. slopes) in Figure 3.2 a and b that molecules with higher

steric effect (group b and c molecules in Chapter 1, Figure 1.3) and electron donating nature (MtPPA) enhance the molecules' dynamic steady state protection capability on an aluminum surface, i.e. increase the aluminum dissolution inhibition factor ω. Previous work also reported that only high steric organic acids acted as aluminum dissolution inhibitor[83, 84]. When the modest aluminum dissolution inhibition obtained in H_3PO_3 solution (ωH_3PO_3) is considered as a benchmark reference, the relative enhanced inhibition factor of other PA molecules (ω_{PA}) referring to ωH_3PO_3 can be expressed relatively as: $\frac{\omega_{PA}}{\omega_{H3PO3}} = \frac{{K_{0(PA)}}^{-1}}{{K_{0(H3PO3)}}^{-1}}$.

The experimental values are shown in Table 3.1 and organized according to the groups defined in Chapter 1, Figure 1.3. It clearly shows that with the increased molecular steric effect (group b and c), the aluminum dissolution is ten to hundred times hindered comparing to group a.

Table 3.1. *Aluminum dissolution rate K_0, and relative aluminum dissolution inhibition factor, ω_{PA} in various PA solutions referring to H_3PO_3 solution.*

	group a)			group b)			group c)		
PA molecule	H_3PO_3	MPA	EPA	tBPA	BPA	PePA	CnPPA	PPA	MtPPA
K_0 [10^{-3} ppm/min]	67.0	35.2	17.5	0.8	2.6	0.2	9.9	6.6	1.2
ω_{PA}	1.0	1.9	3.8	83.8	25.8	335	6.8	10.2	55.8

3.1.3. PA Adsorption on Aluminum Surface

Due to the steady state condition, meaningful electrochemical impedance spectroscopy (EIS) measurements were possible in solutions containing each of the PA molecular structures. EIS measures the complex impedance as a function of frequency, Z(f), while a small amplitude AC voltage, U(f)≈10 mV is applied to drive charge carriers between reference electrode and working electrode (aluminum surface) with the electrochemical current measured. It is standard to further analyze the resulting complex impedance $Z(f) = \frac{I(f)}{U(f)}$ data using an electrical equivalent circuit. A semi-automated custom fitting tool is used (written in LabView) to allow flexible inclusion of non-standard elements into established electrochemical equivalent circuit models. The measured EIS data are displayed in Figure 3.3 as points in the Nyquist-plots of experimental results and the fitted impedances from the equivalent model are shown as plain lines. Bode plots and detailed fitting parameters are also available in the Appendix A, as shown in Figure A.2.

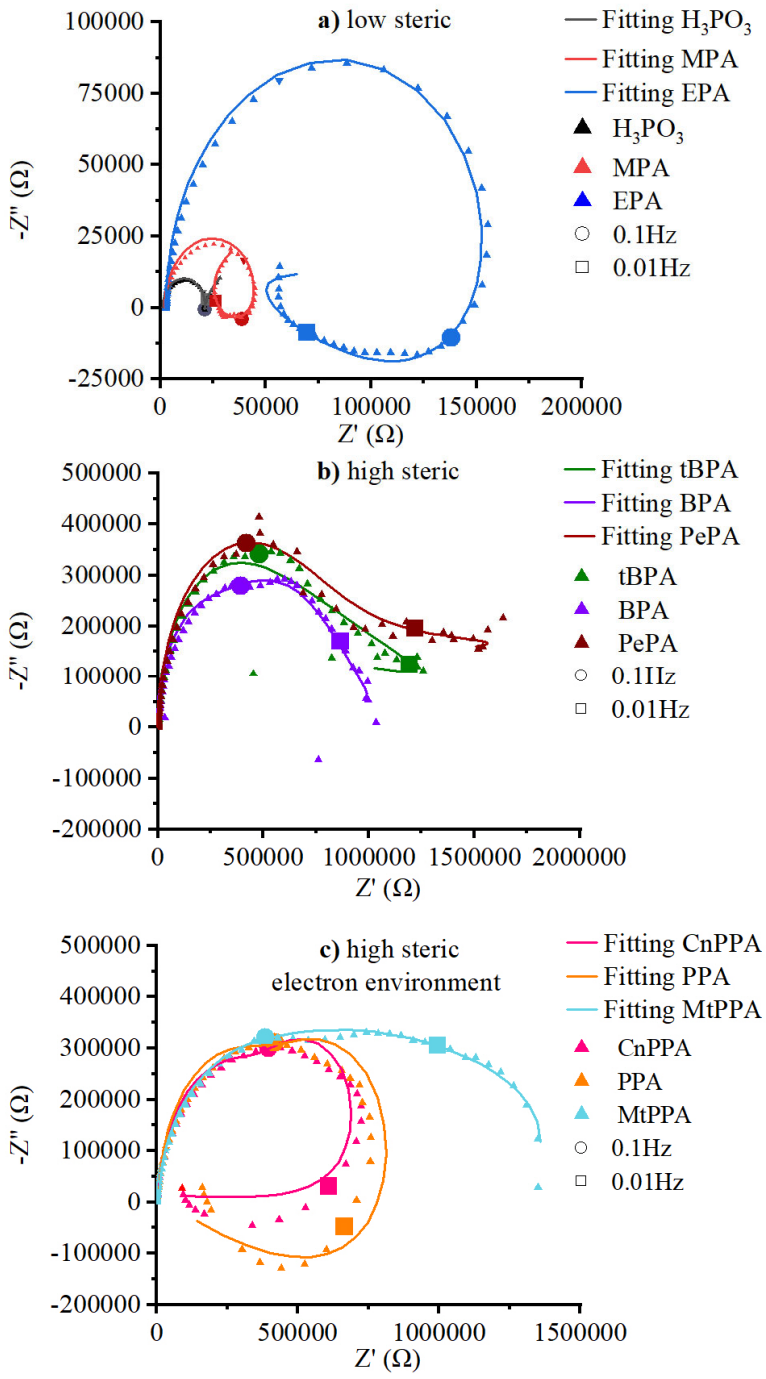

Figure 3.3. *Electrochemical impedance spectroscopy (EIS) measurement of aluminum in different solutions of phosphonic acid (PA) molecules at pH≈2; the different investigated molecules are grouped as shown in Chapter 1, Figure 1.3; original data are plotted as symbols and plain lines represent the fitted equivalent models; a) low steric series: H_3PO_3, MPA, EPA; b) high steric series: tBPA, BPA, PePA; c) high steric with varied electronic environment: CnPPA, PPA, MtPPA. The impedance data measured at 0.1 Hz and 0.01 Hz are marked on the plots as enlarged circle and square, respectively to mark the limits of the low frequency domain.*

The equivalent circuit shown in Figure 2.2 is used to fit the impedance data and interpret the physical meaning of its frequency dependence. The elements in the circuit can always be decomposed into serial or parallel segments; these are adding directly or reciprocally. In our example, R_e and Z_W act in series and are also in series with the parallel junction of $Cg_{(f)}$ to $R_{(f)}$. A capacitance represents an -90° off-phase element with an impedance $Z_C = \frac{-j}{\omega C}$ that decreases towards higher frequency $f = \frac{\omega}{2\pi}$. Towards high frequency (HF), the capacitor $Cg_{(f)}$ (and C_p) exhibit vanishingly small impedance. For that reason R_e and Z_W, whichever is higher, dominates the total impedance at HF. In this HF range, EIS essentially senses ionic motion in the solution and not at the interface. As the frequency decreases, the interface impedance of $Cg_{(f)}$ increases accordingly, exceeding R_e+Z_W , but always limited by $R_{(f)}$ plus optionally (R_p&C_p), which will then become the prevailing impedance at low frequency (LF), where EIS essentially senses the (complex) interface consisting processes (A), (B) and (C) mentioned in Figure 3.1. The equivalent circuit fitting allows extraction of all that information at once, with varying sensitivity in different frequency ranges. $Cg_{(f)}$ and $R_{(f)}$ together form a parallel R_p&C_p gate, which leads to the common semicircle of an electrochemical cell on a Nyquist plot.

To model lateral heterogeneity occurring at the aluminum/ PA solution interface, an optional R_p&C_p gate was added. The optional R_p&C_p gate was already previously proposed to model the presence of pores in a polymer thin film on the electrode surface[72]. The idea is that in our surface functionalizing situation, the protective adsorbed film is partly inhomogeneous and leaky (acting like the pores in a thicker coating) with R_e, inside which the ions can move closer to the aluminum electrode and form another double layer (C_p), and also add a local charge transfer (R_p). Such an optional "pore" element can introduce an additional semicircle feature in the Nyquist plot, particularly if there is a predominant or monomodal "pore" morphology.

An important new feature of our fitting algorithm is that $R_{(f)}$ or $Cg_{(f)}$ can be allowed to change their values in the LF-regime; note that, at LF the EIS spectra contain information about electrochemical changes occurring directly at the interface. For mobile or "unstably adsorbed" ionic species on surfaces, small configuration/morphology changes can be generated and detected by the EIS induced field perturbation. The fitted functions for $R_{(f)}$ and $Cg_{(f)}$ are thus displayed in Figure 3.4 with an emphasis on the low frequency domain; they sense the response of the adsorbed interface layer to the small electrical fields generated by EIS, which is illustrated in Figure 3.1. In the following, the EIS results are discussed in detail with reference to three groups based on the PA molecular structure mentioned in Chapter 1, Figure 1.3.

3.1.3.1. Low Steric PA

The first group a) is characterized by the build-up of a typical capacitive Nyquist-semicircle reminiscent of a simple electrochemical reaction. The impedance of aluminum surface follows a sequence at low frequency $Z_{H3PO3} \approx 21$ kΩ< $Z_{MPA} \approx 45$ kΩ< $Z_{EPA} \approx 160$ kΩ (see Appendix A, Figure A.2):

H_3PO_3: The Nyquist plot of PA (Figure 3.3a) shows a single semicircle, defined by $Cg_{(f)}$, $R_{(f)}$ exhibiting a rather small impedance ≈21 kΩ, followed by a 45° increase of impedance at far LF. This final increase corresponds to a Z_W=1.2 kΩ Warburg impedance element, and describes the ionic diffusion limit (typically controlled by the large amount of aluminum-phosphonate complexes diffusing away from the surface and detected by ICP-OES). The (short-range) solution resistance R_e=1.3 kΩ, is found to be of similar order to the Warburg impedance element. On the other hand, the maximum impedance of the interface (at LF) is more than an order of magnitude higher than the solution resistance (R_e), which suggests that there must be an elevated charge transfer resistance due to a kinetic barrier at the surface. It is thus indicative for a rate limiting adsorbed layer of low-solubility aluminum-phosphonate complexes. The interface capacitance ($Cg_{(f)}$), shows a remarkable increase (Figure 3.4a) at LF, indicating significant resonance ion mobilization and/or thinning of this kinetic barrier layer. The resistance of the interface ($R_{(f)}$), meanwhile decreases only by a small amount. Altogether, this can be interpreted as the signature of a loosely physisorbed layer of aluminum-phosphonate complexes that slightly slows down ion-diffusion at the interface and can easily be mobilized with the low amplitude LF-voltage.

MPA and EPA: Methylphosphonic acid (MPA) and ethylphosphonic acid (EPA) have similar Nyquist curves (Figure 3.3a) and are equally characterized by a single semicircle. A LF-falloff in impedance bends the circles over; this can only be described by a falloff of resistance at the interface ($R_{(f)}$) to a final value around ≈13.5 kΩ (Figure 3.4a); it is noted that this final value is similar to the one found for H_3PO_3 ≈19.2 kΩ, indicating a morphologically similar layer. Before the LF-falloff occurs, MPA exhibits a maximum impedance of ≈45 kΩ; which is even exceeded by EPA to ≈160 kΩ (Bode plot shown in Figure A.2). Together, these findings indicate that both form a slightly more (or laterally more homogeneous) physisorbed layer that acts as a slightly more effective ion diffusion barrier than H_3PO_3, yet they can also be readily mobilized in a small amplitude LF-field. This LF-mobilization is again accompanied by a significant increase of interface capacitance ($Cg_{(f)}$)—underlying again the inherent morphologic similarity to above H_3PO_3 interface barrier. Note that the sequence of increasing physisorption

and increasing barrier effect seen in this group is in agreement with the increasing steric size (i.e. Van der Waals interaction) and hydrophobicity (i.e. lower solubility) of the functional group.

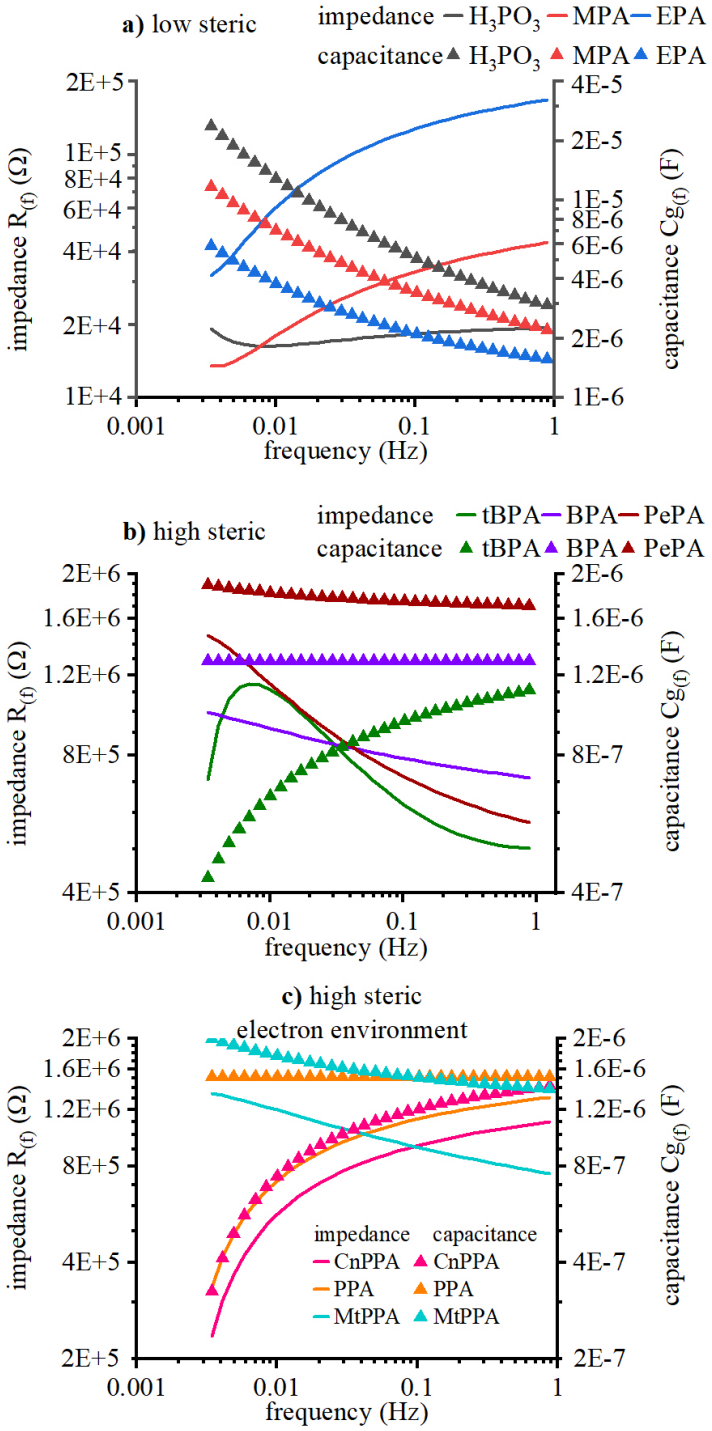

Figure 3.4. *Trend analysis of LF-fitted interfacial resistance ($R_{(f)}$) and capacitance ($Cg_{(f)}$), sorted by the three groups of investigated phosphonic acids, namely a) low steric, b) high steric and c) high steric with varied electron environment. The fitting functions (see also experimental section) were chosen to capture changes at low frequency, while preserving an asymptotic behavior at higher frequency, where EIS is less sensitive to changes of interfacial properties.*

3.1.3.2. High Steric PA

The second group b) is characterized by Nyquist graphs that exhibit a semicircle with an extended high-impedance LF-tail, followed by a minor falloff at ultra-low frequency (f< 0.01 Hz) (Figure 3.3b). Note that the semi-circle, i.e. particularly tert-butylphosphonic acid (tBPA), shows early signs of splitting into two circles, which is indicative for interface inhomogeneity in form of a monomodal pore-like diffusion barrier[73, 74]. Remarkably, the impedance PA adsorbed aluminum surface in this group b) is an order of magnitude higher than in group a), namely around ≈1.2 MΩ-1.7 MΩ. LF-fitting reveals that the $R_{(f)}$ impedance is increasing within this group (Figure 3.4b), which signifies a very clear quantitative distinction to group a). Compared to group a) molecules, it is concluded that molecules from group b) form a different and stronger bond to the surface. Furthermore, the remarkable increase of interface capacity is no longer observed, suggesting that the adsorbed film is rather chemisorbed than physisorbed because it cannot be mobilized or thinned. The author hypothesizes that the chemisorbed PA molecules in this group b) on the aluminum surface protect the Al-Al bonds. With the rate model discussed in Figure 3.1, this type of protection must involve coverage of a certain minimal surface area, and furthermore, collective effects between PA molecules may play a role. Since the phosphonic acid anchor group is formally the same for all molecules in this study, the difference must be linked mainly to the steric size of the functional group (-R) attached to the phosphonic acid anchor group. The chemical structure in group b) indeed provides larger steric volume and is thus likely to cover a larger neighboring surface area. It is thus justified from the results to name this group "high steric".

tBPA: After an initial strong increase of $R_{(f)}$, presumably due to a protective chemisorption, tert-butylphosphonic acid exhibits a rather sharp limiting LF-falloff, suggesting that the initial protective effect is ultimately lost towards the DC limit (Figure 3.4b). In contrast to group a) there is only very little change of the interface capacity, suggesting that there is no significant mobilization of excess physisorbed ions at the interface. It is noted that this finding could partially also be explained by a lower solubility of complexes due to the presence of a more hydrophobic tert-butyl group.

BPA and PePA: The EIS response of benzylphosphonic acid (BPA) and (2-phenylethyl)phosphonic acid (PePA) are similar to tBPA, albeit there is no LF-impedance falloff (Figure 3.3b and Figure 3.4b). Both molecules indicate a continuously increasing interface $R_{(f)}$ at low frequency (≤1 Hz) and, like tBPA, only small changes in $Cg_{(f)}$ (i.e. minor mobilization).

In contrast to tBPA, these two phosphonic acids exhibit phenyl functional groups, which seem to be sterically efficient and stable ionic barriers.

3.1.3.3. High Steric PA with Varied Electron Environment

The third group c) is plotted by Nyquist graphs that exhibit high maximum impedances (Figure 3.3c), suggesting the capability to form long-term chemisorbed layers (that is referred to surface passivation in the field of corrosion) protected by a phenyl group also seen to be effective in group b). While all three molecules in this group c) are composed of phenyl group and thus offer comparable steric, the substituents on the para position of phenyl group are used to introduce a systematic variation of the PA molecular electron environment, i.e. phosphonic acid anchor group electron density, as shown in Chapter 1, Figure 1.3; this is expected to affect the strength of chemisorption of P-O-Al bonds. Indeed, it is observed that a clear correlation between the fitted LF-falloff (Figure 3.4c) and electronic environment variations of the functional group. It is noted that all molecules in this group still show signs of pore-like heterogeneity at the electrochemical interface and the C_p&R_p gate was consequently activated in the equivalent circuit to obtain better fitting.

CnPPA and PPA: (4-cyanophenyl)phosphonic acid (CnPPA) has a strong electron withdrawing effect on phosphonic acid anchor group. It exhibits a broad and continuous decrease of $R_{(f)}$ (Figure 3.4c). Similar to group b), $Cg_{(f)}$ does not significantly change over a broad frequency range, except at ultra-low frequency. A very similar behavior is observed for phenylphosphonic acid (PPA). The phenyl group here also reduces the electron density of the phosphonic acid anchor group.

MtPPA: the presence of cyano group of (4-methoxyphenyl)phosphonic acid (MtPPA) has a strong electron donating methoxy group that increases the electron density of phosphonic acid anchor group. Accordingly, the LF-fitted interface resistance is continuously increasing, i.e. the LF-falloff due to electron withdrawing seen in CnPPA and PPA is no longer detected (Figure 3.4c).

The physisorption, chemisorption and desorption processes of different PA molecules on the aluminum surface discussed in Figure 3.1 are the main factors changing the aluminum surface impedance ($Z_{Al\_surface}$, obtained from Bold plot as shown in Figure A.2). The adsorbed PA molecules can reduce the steady state charges and species transfer on the aluminum surface, which means the inhibition factor of aluminum in various PA molecule solutions is correlating well to

the aluminum surface impedance, $\omega \propto \frac{N_P}{N_D} \propto Z_{Al\_surface}$. Taking the aluminum surface impedance in H_3PO_3 solution as the reference, the relative increased inhibition effect of other PA molecules can be calculated as: $\frac{\omega_{PA}}{\omega_{H3PO3}} = \frac{Z_{Al\_surface(PA)}}{Z_{Al\_surface(H3PO3)}}$.

The results are summarized in Table 3.2, and it is clear that increased steric effect increased ω_{PA} significantly. The electron withdrawing effect destabilizes the chemisorbed PA molecules on the aluminum surface while electron donating effect has the opposite effect.

Table 3.2. *Aluminum surface impedance ($Z_{Al\_surface}$) and relative aluminum dissolution inhibition effect derived from low frequency impedance in various phosphonic acid (PA) solutions referring to H_3PO_3 solution (ω_{PA}).*

PA molecule	group a)			group b)			group c)		
	H_3PO_3	MPA	EPA	tBPA	BPA	PePA	CnPPA	PPA	MtPPA
$Z_{Al\_surface}$ (MΩ)	0.021	0.045	0.16	1.26	0.99	1.65	1.26	0.77	1.35
ω_{PA}	1.0	2.1	7.6	60.0	47.1	78.6	60.0	36.7	64.3

It is interesting to compare the aluminum-dissolution results of Table 3.1 with the EIS findings of Table 3.2. In particular, there is a general correlation between steady state dissolution rate and aluminum surface impedance as displayed in Figure 3.5. The low-frequency (LF) aluminum surface impedance is considered here since it is a good measure for the aluminum dissolution resistance directly at the interface, e.g. in the adsorbed PA layer on aluminum surface. There are two linear correlation, and it confirms that the aluminum dissolution rate is limited by different types of adsorbed layers. Both appear as an interfacial resistance, i.e. LF-impedance in EIS and likely consist of adsorbed phosphonic acid and related ionic aluminum complexes. Our systematic variation of phosphonic acid structure in Figure 3.5 thus allows to make the following three general statements:

1. A growing steric size of the PA molecules increases the dynamic protection of the aluminum surface during the treatment time.
2. Low steric PA molecules hinder aluminum dissolution via physisorbed aluminum-phosphonate complex
3. High steric PA molecules provide good aluminum dissolution inhibition via chemisorbed PA layer.
4. PA molecular electron withdrawing effect destabilizes chemisorbed states.

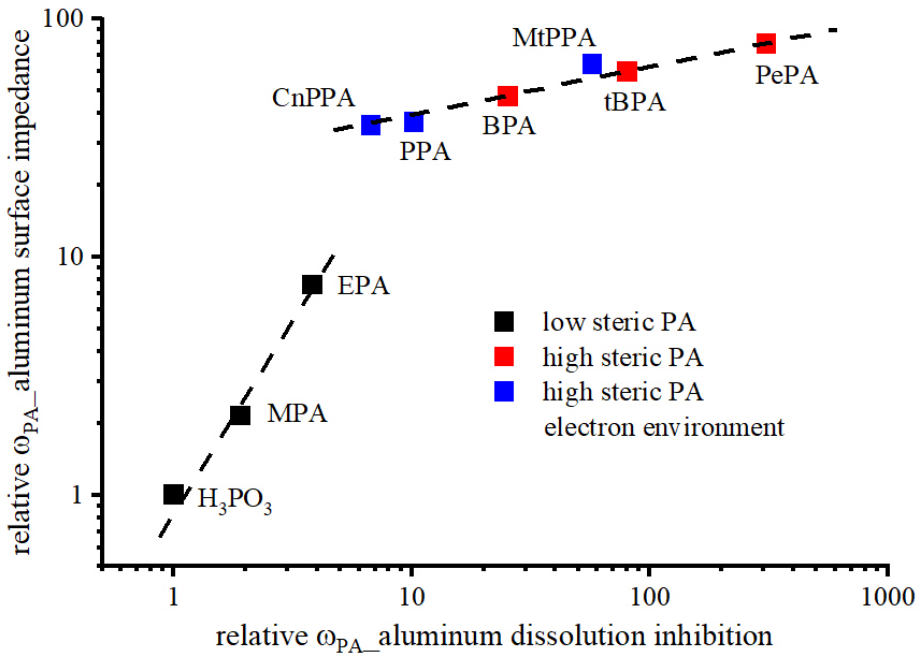

Figure 3.5. *Summary of phosphonic acid (PA) molecules inhibition effect (ω_{PA}) in terms of relative aluminum dissolution rate (by ICP-OES) and of aluminum surface impedance (by EIS) referring to H_3PO_3. The lower dashed line shows that the increased steric effect of low steric PA enhanced dynamic diffusion barrier (aluminum-phosphonate complex) on aluminum surface; the upper dashed line shows that the high steric PA molecules create a chemisorbed layer on aluminum surface, whereas, the stability of chemisorbed PA varied with molecular electron environment.*

3.1.4. Theoretical Molecule Calculations

Computation tools are increasingly used to study adsorbate interaction with various metal surfaces[85]. Thus, in this work DFT calculations were performed on PA molecules to get insights into the molecular characteristics, i.e. energy gap (ΔE) and the electronegativity (χ). The relevant data is presented in Figure 3.6 and Appendix A, Table A.4. For a given reaction and similar reactants, the energy gap is related to the reactivity of the reactant[86]. The electronegativity (χ) represents the ability of an atom to attract shared electrons of a covalent bond (P-O-Al): atoms with similar χ produce a more balanced covalent bond, whereas a higher difference in χ leads to a more polar covalent bond, which also tends to be more susceptible to desorption also represented by K_7 and K_8 in Figure 3.1.

Looking at the big picture, it is interesting to note that the right half of Figure 3.6 represents a group of molecules with theoretically relatively slow chemisorption rates and it indeed consists of group a) plus tBPA. Since in our steady-state experiment, the rate of chemisorption forms a

dynamic balance with the aluminum dissolution rate (Figure 3.1), a relatively low chemisorption rate seems to explain why physisorption remains the predominant adsorption mode for this group of molecules, as seen in EIS experiments—ionic complexes are then formed faster than covalently chemisorbed PA-layers.

Likewise, the left half of Figure 3.6 represents the group of molecules with theoretically relatively higher chemical reactivity and it correlates remarkably well with the molecules of group b) and c), except tBPA, that are indeed identified as "mainly chemisorbed" by EIS (Figure 3.5). The blue arrow in Figure 3.6 indicates the direction of increasing aluminum dissolution inhibition. There is obviously a good agreement between calculated electronegativity and bond stability in EIS LF-electric field, which could identify a critical factor for the high inhibition performance of BPA and PePA. Similar effects due to electronegativity were also previously observed in other DFT simulations[87].

Despite the here presented "big picture" agreements, the present DFT calculations cannot assess the complexity of the dynamic adsorption process nor consider details of the resulting modified oxide morphology[88, 89].

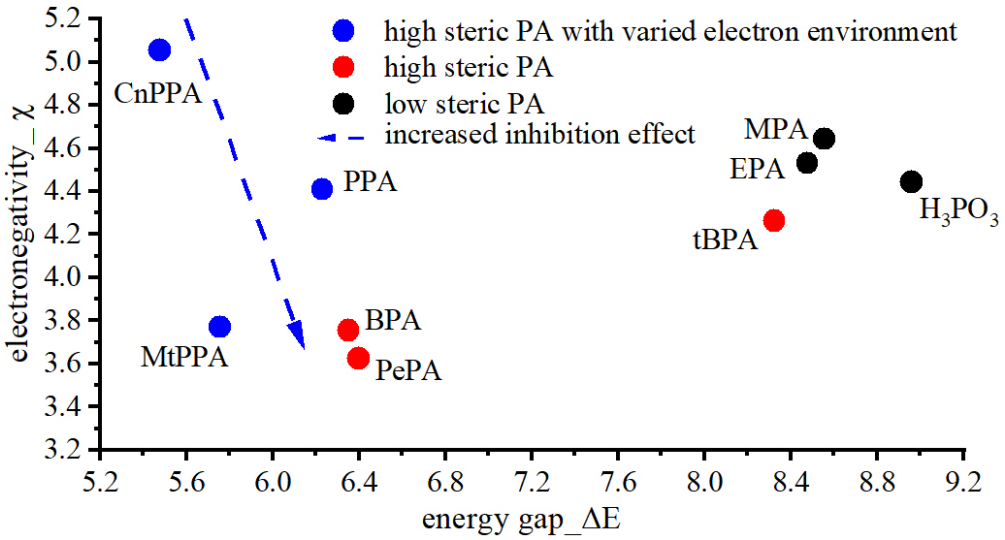

Figure 3.6. *Density function theory (DFT) calculated PA molecular electronegativity (χ) versus energy gap (ΔE). The dash arrow shows the increased experimental inhibition effect of aluminum dissolution found experimentally.*

3.2. Conclusion

A selection of nine different phosphonic acid (PA) molecules was used to comparatively study their steady state adsorption behavior at the dynamically dissolving aluminum surface at pH≈2. The results reveal existence and details of two distinct steady state adsorption modes.

Aluminum dissolution was found to vary over two orders of magnitude leading to effective passivation only for specific PA molecular structures (with optimal steric and electron environment effects). Systematic variations of the functional group attached to phosphonic acid anchor group allowed differentiation between PA molecular steric and electron environment effects.

The steady state nature of this unique and technologically relevant solid-liquid interface is demonstrated via time-resolved ICP-OES measurements and then discoursed in terms of a proposed rate model. The results suggest that PA molecules with high molecular steric can inhibit aluminum dissolution, whereas low steric PA molecules are less effective.

EIS was used to investigate details of charges and species transfer at aluminum-PA solution interface. EIS data is analyzed using an enhanced equivalent circuit model that allows identification and discussion of changes in low-frequency adsorbed PA film ionic resistance. The analysis shows that the selected molecules can be grouped into three groups of distinctive electrochemical behavior.

The first group a) of low steric PA molecules seems to form a weakly physisorbed diffusion barrier, consisting of aluminum-phosphonate complexes. The solubility of these complexes decreases with increased PA steric (from H_3PO_3 to EPA), though the aluminum dissolution remains relatively high.

It is found that the dynamic stability at PA solution-aluminum interface increases to a higher level when PA molecular steric increases in groups b) and c). A very different behavior is observed, where energetically more stable chemisorbed states are populated. Specifically, tert-butyl group (tBPA) and aromatic structures (PPA, BPA, CnPPA, MtPPA, PePA) generally provide high steric effect that are favorable for chemisorption. However, in group c), the covalent P-O-Al bond stability can be significantly weakened via electron withdrawing effect.

The discussed correlations between DFT-calculated PA molecule electron properties (electronegativity and energy gap) and experimental data are remarkable, despite the substantial simplifications made.

Chapter 4. Phosphonic Acid Structural Effect on Adsorbate Layer and Adsorbent Aluminum Oxide

This chapter is adapted from a scientific manuscript in preparation for publication with multiple co-authors: Zhao R, Patrik S, Gaan S, Crockett R, Hauert R, Heuberger M and Jeurgens L P H. The major part of this work was done by Zhao R. Hauert R supervised the XPS surface characterization. Crockett R performed the ToF-SIMS measurement. Patrik S, Gaan S, Heuberger M and Jeurgens L P H contributed to the discussion and correction of this paper.

After the PA adsorption process on the aluminum surface as described in Chapter 3, the treated aluminum sheet is removed from the PA solution and rinsed by H_2O in air. The dynamic charge- and species- transfer process on the aluminum surface is then stopped. A final state of PA modified aluminum oxide is obtained. Chapter 4 continues to study the PA molecular structural effect on such final modified aluminum oxide surface. Firstly, the adsorbate PA layer is characterized by X-ray photoelectron spectroscopy (XPS) to investigate the PA structural effects on the stratification of PA layer with aluminum oxide layer as a function of prior adsorption time. A novel concept a dimensionless stratification factor is introduced to describe the stratification level of adsorbate PA molecules (phosphorus signal) with adsorbent aluminum oxide. Then, the effect of adsorbate PA layer on the adsorbent aluminum oxide thickness and surface oxide/hydroxide state is discussed. Meanwhile, this chapter also reveals the missing link that Chapter 3 is dedicated to (section 3.1.1.), i.e. the adsorbent transition from initial native aluminum oxide (L_{OX}) to aluminum during the PA treatment. At the end of this work, time of flight-secondary ion mass spectroscopy (ToF-SIMS) is used to investigate the phosphonic acid anchor group binding mode with aluminum oxide. Our findings reveal a fundamental understanding of the relationship among PA molecular steric effect, prior treatment time, PA adsorbate layer, aluminum re-oxidation and PA binding mode with the aluminum oxide.

4.1. Result and Discussion

4.1.1. Stratification Factor

Each type of PA molecule studied (Chapter 1, Figure 1.3) contains a single phosphorus atom of the phosphonic acid anchor group. Hence, the detected P 2s photoelectron intensity (I_{P2s}) provides a qualitative measure of the average surface concentration of PA molecules in the probed surface region. Accordingly, for each PA treatment, an estimate of the phosphorus surface atomic concentration ($\tilde{C}_{\mathrm{P}}$ in at.%) was calculated from the integrated areas of the resolved C 1s, O 1s, Al 2p, P 2s main peaks by using the corresponding experimental sensitivity factors and assuming homogeneous element distribution. However, as shown in Chapter 1, Figure 1.3, different PA molecules each have a different atomic number fraction associated with the phosphorus atom. Hence, a qualitative comparison of the molecule surface concentration of the different types of PA molecules is obtained by normalizing $\tilde{C}_{\mathrm{P}}$ with the corresponding molecular atomic number fraction, f_{P}, which is defined as the number of phosphorus atom divided by the total number of atoms in the respective PA molecule, i.e. $\tilde{C}_{\mathrm{P}}/f_{\mathrm{P}}$ (excluding hydrogen, since it cannot be detected by XPS). Values of f_{P} for the different types of PA molecules considered in this study are reported in Table B.1 of Appendix B. Moreover, with the XPS probing depth of ≈ 5 nm, $\tilde{C}_{\mathrm{P}}/f_{\mathrm{P}}$ sole does not include the information on the layer structure. Specifically, if the PA layer is occurring as a top-surface layer on the adsorbent aluminum oxide layer, or if there is a mixture of aluminum oxide/hydroxide and PA molecules in the modified oxide layer, which is crucial for surface functionalization, e.g. a well-stratified PA surface provides better surface functionalization such as hydrophobic or reacting with further applied polymer/adhesive.

To obtain the information on the stratification of PA layer within aluminum oxide layer, it is important to note that the adsorbate PA layer on the surface attenuates the Al 2p signal from both aluminum oxide and metallic aluminum. Specifically, as illustrated in Figure 4.1a, the Al 2p photoelectron intensity is attenuated differently depending on the coverage of the single PA molecule (functional group, R); e.g. a high PA steric effect will result in a higher PA coverage that is more effective attenuation of the Al 2p signal intensity. Furthermore, a less compact PA layer that rather mixes with aluminum oxide/hydroxide results in a low attenuation of Al 2p signal, as illustrated in Figure 4.1b. With the increase of PA steric, the attenuation of Al 2p is increased (Figure 4.1c) until the PA layer is completely stratified on top of the aluminum oxide layer (Figure 4.1d). Accordingly, to include the information on stratification of PA layer and oxide layer, and improve the robustness of the *qualitative* comparison of the different adsorbate

PA molecules distribution, the normalized phosphorus concentration, $\tilde{C}_P/f_P$, was divided by the corresponding aluminum surface concentration (including both metallic and oxidized Al 2p peaks), $\tilde{C}_{Al}$. Resulting value of the normalized phosphorus surface concentration will be further denoted as PA stratification factor, namely $\theta_{PA} = \frac{\tilde{C}_P}{f_P \cdot \tilde{C}_{Al}}$.

The here defined stratification factor is a unit less number between zero and infinity; the higher its value, the more phosphorus is located in a prominent separate layer (i.e. PA layer) above the aluminum containing layer(s).

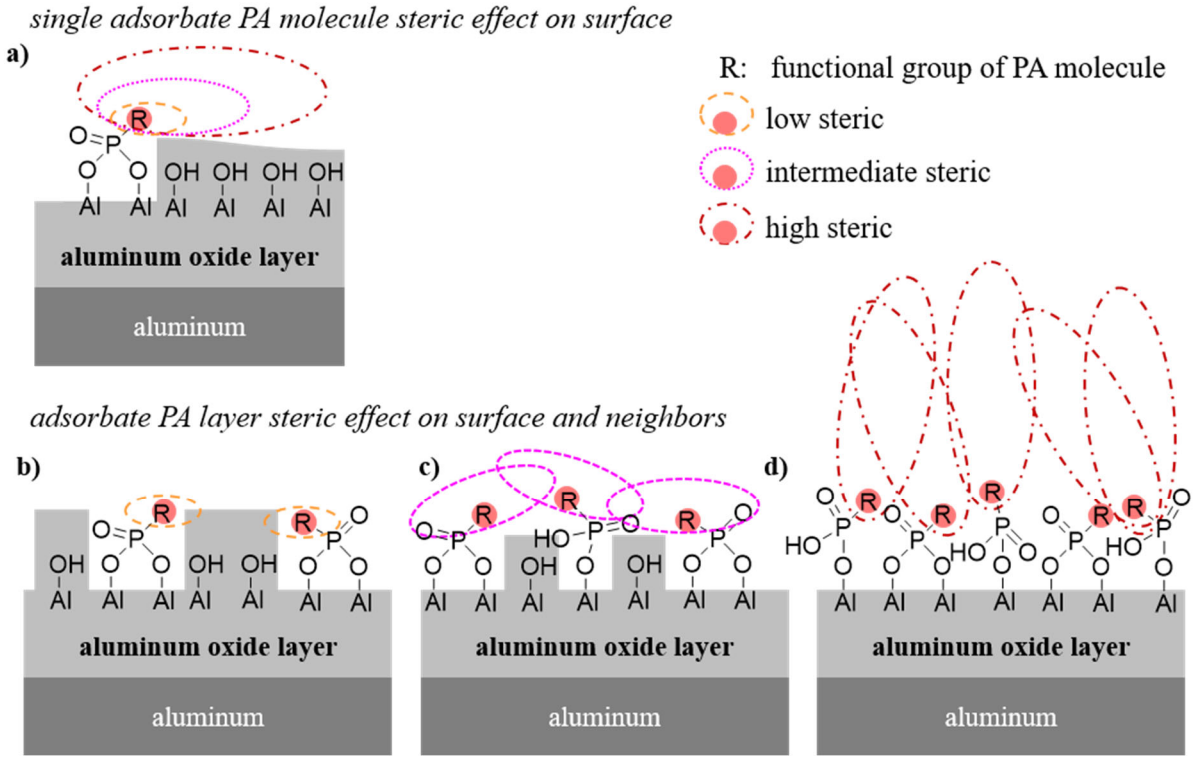

Figure 4.1. *Schematic illustration of different stratification degrees of PA molecules with an idealized hydroxylated aluminum oxide surface. The steric effect of the functional groups, R, as attached to the phosphonic acid anchor group is visualized by the elliptical line shapes.* ***(a)*** *For single PA molecules adsorbed on the hydroxylated surface, different steric effects of the functional group, R, cause a different volumetric molecular coverage of the aluminum oxide surface. For adsorbed PA layer on surface:* ***(b)*** *a negligible interaction between neighboring low-steric PA molecules results in a relatively low stratification with oxide, whereas* ***(c,d)*** *a higher PA steric effect increases the stratification of the PA adsorbate layer with adsorbent aluminum oxide, resulting in higher stratification factor.*

Besides this simple measure, more quantitative and elaborate calculations of photoelectron intensity have been proposed to extract the thickness and molecular density of adsorbed molecules on solid surfaces, such as for the adsorption of organometallic dyes on aluminum oxide

[90]. However, such quantitative procedures require specific pre-knowledge and/or presumptions on the composition, atomic density, porosity, morphology and molecular arrangement of the adsorbate layer, as well as of the respective inelastic mean free paths for inelastic electron scattering of the photoelectrons. Such detailed quantitative procedures are not feasible for screening the performance of a large range of different PA molecules with unknown adsorption characteristics and depth distributions, as is the case in the present study.

4.1.2. Adsorbate PA layer

As displayed in Figure 4.2, calculation of the stratification factor versus immersion time for each type of PA molecule provides a measure of the layer composition. The stratification factor results are again discussed in three groups of PA molecules (Chapter 1, Figure 1.3), i.e. (a) low steric, (b) high steric and (c) high steric with varied electronic environments.

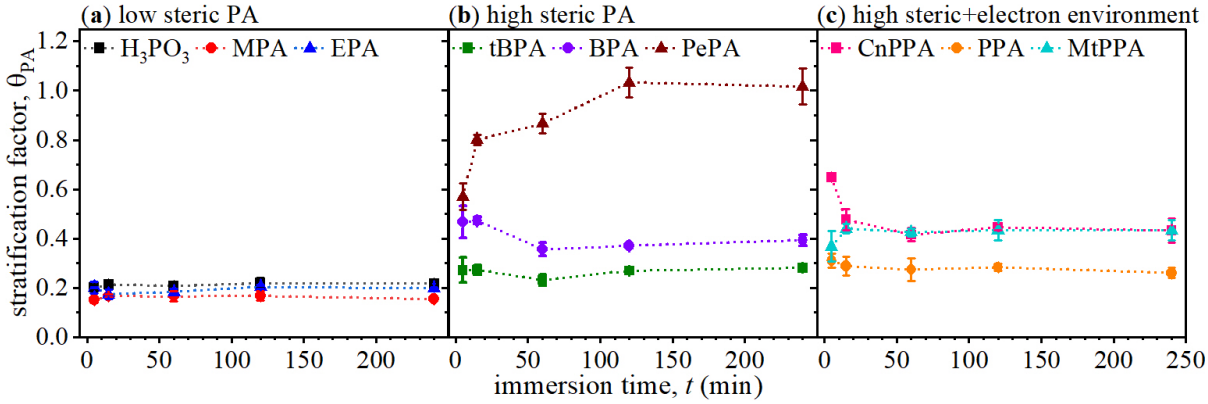

Figure 4.2. *Stratification factor, θ_{PA}, versus immersion time for the three groups of PA molecules categorized in Chapter 1, Figure 1.3: (a) low steric PA, (b) high steric PA and (c) high steric PA with different electronic environments of the phosphonic acid anchor group. The stratification factor was determined from the measured C 1s, O 1s, Al 2p, P 2s photoelectron intensities and the atomic P fraction, f_P. Typical industrial immersion times are in a range of 6 seconds to 600 seconds.*

4.1.2.1. Low Steric PA

The first group a) consists of phosphonic acid (H_3PO_3) methyl phosphonic acid (MPA), ethyl phosphonic acid (EPA). The molecular steric volume is stepwise increased from H_3PO_3< MPA< EPA. A previous study shows how an increased steric effect decreased the in situ aluminum dissolution in PA solution[32]. However, the corresponding ex-situ θ_{PA} values are similar (0.19±0.02) for all three low steric PA modified aluminum oxides, and independent of the immersion time as shown in Figure 4.2a. Moreover, the corresponding $\theta_{PA} \approx 0.19$ are relatively low as compared to those of the high steric PA molecules following in Figure 4.2 (b and c).

Such low θ_{PA} values suggest that low steric PA is found throughout the aluminum oxide/hydroxide layer, independent of the steric sequence (i.e. H_3PO_3< MPA< EPA). A more homogeneous distribution of phosphorus might be attributed to the formation of physisorbed aluminum-phosphonate (Al-PA) complexes as described in Chapter 3[32]. In an Al-PA complex, the aluminum and phosphorus atoms condense via ionic interaction throughout a layer (i.e. minimal stratification). There is evidence that such complexes are converted to chemisorbed state during H_2O rinsing in air, which then generates similar oxidized layers, still exhibiting a homogeneous mixture of PA and aluminum oxide/hydroxide on surface. This hypothesized conversion from a prior stage of physisorbed Al-PA complexes to the current final chemisorbed state is evidenced by the ToF-SIMS analysis of the PA binding mode with aluminum oxide in section 3.2.4. Notably, H_3PO_3 modified aluminum oxide exhibits similar chemisorbed PA binding mode with aluminum oxide as PePA that shows a stable chemisorption on aluminum surface during prior adsorption stage. Moreover, the time-independent θ_{PA} values indicate only those physisorbed Al-PA complexes that are strongly interacting with the surface (i.e. low solubility) convert to a chemisorbed state during the H_2O rinsing in air. We further hypothesize that during the in-situ adsorption stage the initial aluminum oxide film (Chapter 2, Figure 2.3a, L_{OX}) is continuously dissolved at the onset of the immersion in the low steric PA solution. Actively dissolved aluminum cations combine with PA anions to form a more stable Al-PA complex, which can remain near the dissolving aluminum metal surface during the PA treatment[32]. Most of this sediment of aluminum-phosphonate complexes are effectively removed from the surface during the H_2O rinsing step. If only parts were removed, there should be an increase of film thickness and associated change of stratification factor with time. However, neither stratification factor (Figure 4.2a) or oxide thickness (discussed later in Figure 4.5a) of low steric PA modified aluminum oxide increases with time.

4.1.2.2. High Steric PA

The group b) consists of tert-butylphosphonic acid (tBPA), benzylphosphonic acid (BPA), and (2-phenylethyl)phosphonic acid (PePA), again with increasing steric volume, i.e. tBPA< BPA< PePA. The calculated θ_{PA} values for the high steric PA modified aluminum oxides are plotted as a function of the immersion time in Figure 4.2b. The tBPA adsorbate layer on the aluminum oxide surface has a time-invariant θ_{PA} value of around 0.27±0.02, which is higher than the values of the low steric PA series (0.19±0.02). Indeed, the higher PA steric effect of tBPA is expected to promote Van der Waals interactions of the functional groups (i.e. the tert-

butyl groups) with the surface and among neighboring PA molecules, as illustrated in Figure 4.1c, which results in the formation of a more compact and (kinetically) more stratified tBPA adsorbate layer on the aluminum oxide surface, as compared to the low steric group, after the water rinsing in air step.

BPA has a higher steric effect than tBPA (due to the benzyl group), and indeed the corresponding θ_{PA} value is higher than tBPA (Figure3.3c). Notably, the initial θ_{PA} value of ~0.47 (15 min) for BPA decreases to a constant value of ~0.37 after 60 min. Chapter 3 supported the idea that BPA exhibits a stable chemisorption on aluminum oxide surface during the dynamic adsorption stage. But this chemisorption was still less pronounced as for PePA as seen from a higher aluminum dissolution rate and lower EIS measured aluminum surface impedance. Thus, we may conclude that within prior adsorption time of 15 min, BPA probably adsorbed on the initial aluminum oxide (*L*OX), which is in accord with the observed higher initial θ_{PA} value (as illustrated in Figure 4.1c). However, the *L*OX was continuously dissolved with time during this prior adsorption stage over 60 min (*L*OX dissolution is discussed later in detail in Figure 4.5). Like before, the dissolved aluminum cations still formed Al-PA complex on surface. Thus, after H_2O rinsing in air, the stratification of chemisorbed BPA layer with aluminum oxide layer is reduced due to the mixture of Al-PA complexes captured by BPA layer on surface.

Remarkably, the θ_{PA} value of PePA modified aluminum oxide increases from θ_{PA} =0.57 for t = 5 min to θ_{PA} =1.0 for t = 120~240 min. Note that PePA created the most stable in-situ chemisorption on aluminum oxide surface during the prior adsorption stage due to its highest steric effect among PA molecules studied. Thus, these strong chemisorbed PePA molecules seem to also effectively passivate the initial aluminum oxide (*L*OX) in acidic PA solution. After H_2O rinsing in air, PePA adsorbed layer then exhibits a high stratification (i.e. surface concentration) with *L*OX surface similar to BPA (as illustrated in Figure 4.1c) since PA is mainly adsorbed at the *L*ox surface and no significant amounts of PA-Al complexes have been formed. Note that the initial (5 min) θ_{PA} value of PePA is slightly higher than BPA, which might be due to a higher steric of single PePA molecule causing higher Al 2p signal attenuation as described in Figure 4.1a. The post-treatment oxide layer thickness (Figure 4.5) is higher with PePA, which indeed supports the idea that the original Lox is effectively protected from dissolution. There is a gradual increase of θ_{PA} value within 120 min suggesting that PePA adsorbed layer at the top is increasingly populated with time. This is due to the increased steric effect of PePA favors the adsorption of additional molecules on the neighboring sites resulting into a transition from

a less compact PePA layer to a dense compact PePA layer as illustrated in Figure 4.1 from c) to d). This transition increases the attenuation of Al 2p signal exhibiting an increasing θ_{PA} value. This transition process is also associated with an increase of the ratio between the carbon and aluminum atomic concentrations, $\tilde{C}_C/\tilde{C}_{Al}$, with time, as shown in Figure 4.3a (note: this trend is only observed for the PePA treatment).

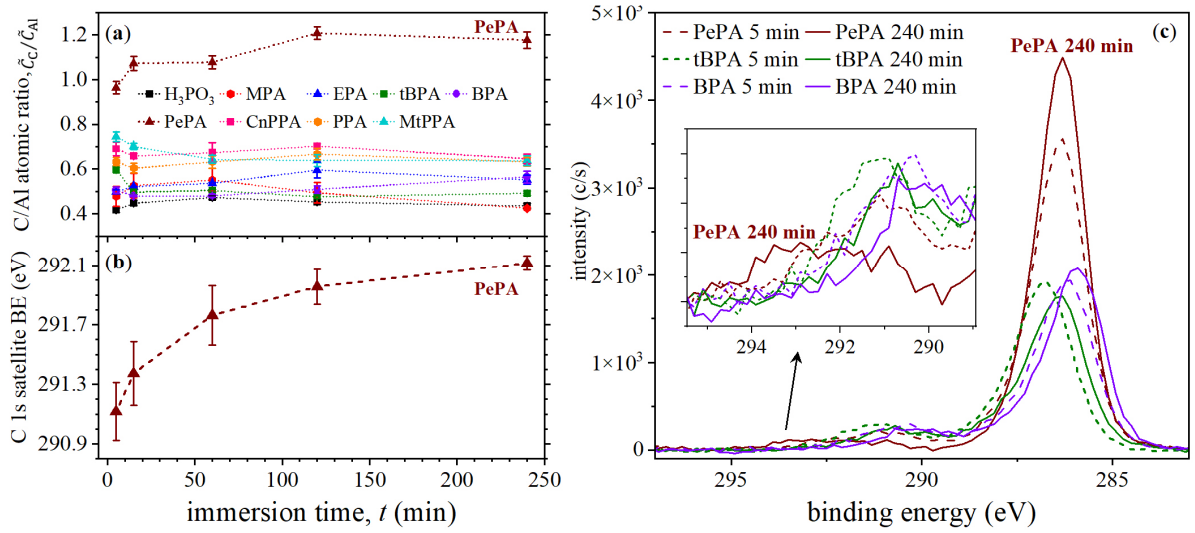

Figure 4.3. *Ex-situ XPS analysis of the PA adsorbate layers on aluminum oxide.* ***(a)*** *Ratio of the C and Al atomic concentrations, $\tilde{C}_C/\tilde{C}_{Al}$, with increasing immersion time.* ***(b)*** *Binding energy shift of the C 1s π→π* shakeup satellite as function of time for the PePA modified aluminum oxide surface.* ***(c)*** *XPS spectra of the C 1s region (for t = 5 min and t = 240 min) as recorded after high steric PA treatment (tBPA, BPA and PePA), evidencing a weak, but distinct C 1s π→π* shakeup satellite peak at the higher binding energy side of the C 1s main peak.*

The binding energy (BE) shift of the C 1s shakeup of PePA layer helps to identify the driving force of the gradually increased stratification factor, as follows. For molecules with π electron orbitals, such as phenyl or vinyl group, the C 1s peak shows a discrete π→π* shakeup satellite about 6-10 eV at the higher binding from the main (zero-loss) C 1s peak[91]. The shake-up peak is due to an electronic transition during the photoemission process, involving initial and final state molecular orbitals associated with an unsaturated carbon functionality[92]. The π electron orbitals from neighboring molecules can have a weak attractive interaction, which can result in so-called π-π stacking, which affects the π→π* shakeup satellite structure. For aromatic rings, the T-shaped conformation (edge to face) and the face-to-face-offset stacking (as in graphite) are the energetically favored conformations[93]. π-π stacking of phenyl groups typically induces a shift of the π →π* C 1s shakeup peak towards higher binding energies (up to about ~10.0 eV from the zero-loss C 1s peak[92]), as indeed evidenced for the PePA treated surfaces in Figure 4.3b and c. As evidenced in Figure 4.3b, the C 1s shakeup peak for the PePA

treated surface increases with increasing immersion time from 291.2 eV to 292.5 eV, which suggests a gradual rearrangement of the phenyl groups on the aluminum oxide surface due to the increased π-π interactions with increasing surface coverage. For the longest PePA treatment of t = 240 min, the XPS analysis shows a clear difference of the π→π* shakeup satellite binding energy with respect to the other PA treated surfaces: see Figure 4.3c and Appendix, Figure B.1. An additional relatively weak π→π* shakeup satellite intensity has appeared in the binding energy range from 290 eV to 294 eV (see Figure 4.2c), which indicates that the phenyl groups of the adsorbed PePA molecules alter their π →π* excitations with increasing surface coverage due to π-π stacking. These findings indicate that the attractive π-π interactions between neighboring phenyl groups induce mutual reorientations of previously adsorbed PePA molecules. In other words, the π-π interaction among the phenyl groups provides a driving force for the increasing of adsorbed PePA molecules on the aluminum oxide surface. For short immersion time, few PePA molecules are randomly adsorbed on the oxide surface and the π-π interactions are still relatively weak, as sketched in Figure 4.4a. With increasing time, the π-π interactions between neighboring phenyl groups favor a mutual alignment (reorientation) of adsorbed PA molecules on the oxide surface, while at the same time creating additional space for new PePA molecules to adsorb on the surface, as illustrated in Figure 4.4 b and c. Surface saturation by a relatively compact packing of aligned PePA molecules is reached after 120min, as illustrated in Figure 4.4d. The illustrated sequence in Figure 4.4 assumes a T-shaped conformation (edge to face) of neighboring phenyl groups (since it is one of the energetically favored configurations) [93], although the present results cannot distinguish between a preferred T-shaped conformation and face-to-face-offset stacking. Similar surface reorganization phenomenon is also reported in other previous studies[94].

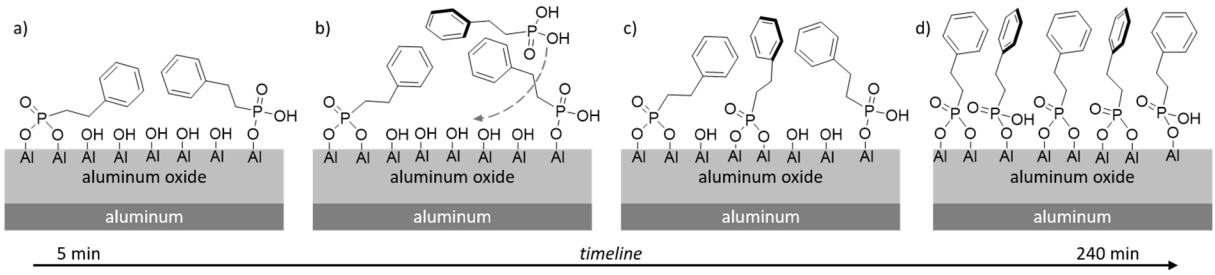

Figure 4.4. *Illustration of the subsequent steps of adsorbate layer formation by PePA molecules on the hydroxylated aluminum surface, showing a collective reorientation of adsorbed PePA molecules with increasing stratification with aluminum oxide layer as driven by the π-π interaction of neighboring phenyl groups (with a preferred T-shaped conformation of the π-π stacking interactions).*

In summary, a plausible picture emerges from this stratification factor increase with increasing steric effect. Specifically, the surface treatment with low steric PA molecules (i.e. H_3PO_3, MPA and EPA) results in adsorbate PA layers exhibiting low stratification factor, which seems to originate from the conversion of the prior permeable physisorbed aluminum-phosphonate complex to chemisorbed state after H_2O rinsing in air. The consistently higher stratification factor of PA molecules increases with increasing PA steric effect (tBPA and BPA). This is driven by the increased individual PA coverage and interaction among PA molecules on the surface (as illustrated in Figure 4.1c). However, when the steric effect includes π→π stacking capability as with PePA with 2-Phenyl ethyl group, the increased Van der Waal's interaction among 2-phenyl ethyl groups even further increases the stratification of PePA adsorbate layer with aluminum oxide layer. This emergence of self-assembly results in a distinctive adsorption behavior (as illustrated in Figure 4.1d and Figure 4.4): leading to a gradual increase of the number of adsorbed molecules that is accompanied by a gradually increased stratification factor of the PePA adsorbate. Notably, BPA has a similar molecular structure (albeit a lower steric effect) as compared to PePA. However, BPA does not show signs of self-assembly, since BPA has lower steric and one less degree of freedom to rotate the phenyl group. The author thus suggests that surface densification of adsorption PA molecules by π-π interactions might also require a certain molecular conformational freedom, actually in accordance with previous findings[95, 96]. Notably, it is also evidenced an influence of the PA alky chain length on the absorption behavior[97]: from decylphosphonic acid ($C_{10}H_{23}O_3P$) to octadecylphosphonic acid ($C_{18}H_{23}O_3P$), the increased steric effect changes the PA adsorbed layer from a randomly oriented and loosely bounded adsorbate layer to a well orientated and more compact adsorbate layer.

It is worth noting that the in-situ aluminum dissolution inhibition of PePA (as discussed in Chapter 3) is not significantly enhanced by this slow increased PePA stratification process because at the initial stage, a loose compact PePA chemisorbed layer on aluminum oxide surface already provides a sufficient protection.

4.1.2.3. High Steric PA with Varied Electron Environment

The group c) consists of (4-cynaophenyl)phosphonic acid (CnPPA), phenyl phosphonic acid (PPA) and (4-methoxyphenyl)phosphonic acid (MtPPA) exhibiting similar high steric effects, but varying electron densities of phosphonic acid anchor group, which increases in the order CnPPA< PPA < MtPPA. Chapter 3 shows that the different electron environments affect the

stability of the PA chemisorbed aluminum surface[32]. However, as follows from the comparison of Figure 4.2c, CnPPA and MtPPA have a similar stratification factor of roughly $\theta_{PA} \approx 0.44\pm0.02$ after 15 min, despite their different electron environments. However, within the initial 15 min, CnPPA exhibits decrease of θ_{PA} value similar to the case of BPA. According to the picture established above, this can also be explained by the gradually dissolved initial aluminum oxide (L_{OX}) and the near-surface Al-PA complexes as explained in the section 4.1.2.2.

Notably, PPA has a slightly lower steric effect, resulting in a lower stratification $\theta_{PA} = 0.28\pm0.02$ (as compared to CnPPA and MtPPA). Thus, the PA molecular electron environment has negligible effect on the adsorbate layer, while PA molecular steric effect still dominates the adsorbate PA layer formation.

4.1.3. Adsorbent Aluminum Oxide

As illustrated in Figure 2.3, the aluminum sheets were etched in NaOH solution and then rinsed by water in air to obtain a reproducible surficial oxide layer prior to each PA treatment. This native aluminum oxide is named as L_{OX}. The different polymorphs of aluminum oxide are unstable at pH≈ 2 and thus the oxide film is actively dissolved in a PA solution, unless the dissolution is kinetically hindered by the formation of a diffusion limiting physisorbed aluminum-phosphonate complex or chemisorbed PA molecules as discussed in Chapter 3. The high aluminum dissolution rate (Figure 3.2) and low aluminum surface impedance (Figure 3.3a) both indicate the surface treatment with the low steric PA molecules results in fast complete dissolution of L_{OX}. With increasing steric effect of the PA molecule, aluminum dissolution is kinetically hindered by chemisorption of high steric PA. Subsequent water rinsing in air not only removes any physical precipitates, but also induces a re-oxidation of the hydroxylated aluminum surface, particularly when the PA adsorbate layer is permeable for O_2. To study the role of the adsorbate PA molecules in the aluminum re-oxidation process after H_2O rinsing in air, the PA modified aluminum oxide surfaces were analyzed by XPS. In the following, first the aluminum oxide thicknesses of L_{OX} and after PA treatment are compared for the different groups of PA molecules. Next, the changes in the local chemical state of the oxygen anions in the oxide films will be determined from the oxygen auger parameter.

4.1.4. Aluminum Oxide Thickness

4.1.4.1. Alkaline Etched aluminum oxide

A XPS survey scan of *L*OX film is presented in Appendix B, Figure B.2. The survey evidences a typical oxidized aluminum surface with some adventitious carbon, which originates from air-expose after the rinsing step. Moreover, the featureless plateau shape of the upper valence band region (in the binding energy range from 0 to 15 eV) is characteristic for an amorphous state of the *L*OX film, as shown in Appendix B Figure B.3[98]. The valence band also evidences a small, but significant contribution from the conduction band of the underlying metal (causing signal intensity in the binding energy range from 5 eV up to the Fermi level)[98]. Analogously, the measured Al 2p regions of *L*OX evidence separate metallic and oxidized contributions from the metal substrate and the oxide overlayer, respectively (Appendix B, Figure B.4). This implies that in all cases the thickness of the amorphous aluminum oxide layer is significantly less than the XPS probing depth. The XPS probing depth equals $3\lambda \cdot \cos(\theta)$, where λ denotes the inelastic mean free path (IMFP) of the emitted photoelectrons traversing through the solid and θ is the detection angle with respect to the sample surface normal (here: $\theta = 45°$). Values of λ_m and λ_o for emitted Al 2p photoelectrons traversing through aluminum metal and the aluminum oxide film can be calculated from the well-known TTP2 formalism[99] by adopting appropriate values for the density, optical bandgap and the number of valence electrons in the metallic aluminum and in the amorphous oxide film, respectively. The exact density of the amorphous *L*OX film (after water rinsing and exposure to air) is unknown, but may be assumed to lie in between the densities of amorphous Al_2O_3 and the $Al(OH)_3$ hydroxide phase. Values for the densities, optical band gap and number of valence electrons for various oxide and hydroxide phases are listed in Appendix B, Table B.2. This results in an average value (and standard deviation) of the IMFP of Al 2p photoelectrons in the oxide/hydroxide phase of $\lambda_o \approx 3.25 \pm 0.20$ nm (*note:* for the metallic aluminum substrate, $\lambda_m = 3.12$ nm). The corresponding Al 2p probing depth therefore lies in the range of 6.5 - 7.3 nm. The metallic Al 2p main peak is clearly discernable in all measured Al 2p spectra, which indicates that the thickness of the *L*OX film is well below 6 nm.

A more accurate estimate of the oxide film thickness is obtained from[100].

$$d = \lambda_o \sin 45^0 \ln\left(\frac{N_m \lambda_m I_o}{N_o \lambda_o I_m} + 1\right) \tag{4.1}$$

where N_m and N_o are the atomic molar densities of aluminum in the metal and the oxide, respectively (Appendix B, Table B.2); I_o and I_m are the primary zero-loss intensities of oxidized and metallic Al 2p main peaks, as resolved by peak fitting of the Shirley background corrected Al 2p spectra. Here it is noted that the presence of an adsorbate layer does not affect the thickness calculation according to Equation(4.1), since the Al 2p photoelectrons emitted

from the metallic aluminum and the aluminum oxide overlayer have practically the same kinetic energy (and thus experience the same attenuation by a given overlayer).

The averaged value and standard deviation of the thickness of the L_{OX} film, as calculated for three different L_{OX} film (after rinsing and air exposure), applying the different densities and IMPFs as tabulated in Table B.2 Appendix B, equals 3.56 ± 0.65 nm. Noteworthy, this average oxide film thickness lies in between the oxide film thicknesses of 3.4±0.1 and 3.7±0.1 nm, as reported for native (air-formed) and water-exposed oxide films on Al(100) and Al(111) single crystals, respectively[82].

4.1.4.2. PA modified aluminum oxide

The average values (with standard deviation) of the thickness of the oxide film after each PA treatment (by applying different parameters from α-$Al(OH)_3$ to α-Al_2O_3) is plotted as a function of the immersion time in Appendix B, Figure B.5. It follows that the calculated thickness values vary about ±0.5 nm for a change in density as large as 38% (from 2.46 g/cm^3 for α-$Al(OH)_3$ to 3.97 g/cm^3 for α-Al_2O_3). The shapes of the valence band spectra of PA treated surfaces are very similar to those of the L_{OX} film, i.e. rather featureless plateau shape for an amorphous state of the oxide film (Appendix B, Figure B.3 and B.6) [98]. The density of the oxide film will thus be likely close to that of amorphous-Al_2O_3 with ~3.2 g/cm^3. Therefore, in the following the oxide properties of amorphous aluminum oxide [101] will be used to calculate the thickness values of the L_{OX} and PA modified aluminum oxides. The thus calculated final oxide film thickness values are plotted as a function of the immersion time for each group of PA molecules in Figure 4.5. The corresponding averaged value and standard deviation of the initial thickness of the L_{OX} film equal 3.36±0.1 nm and is also indicated by the grey area in Figure 4.5.

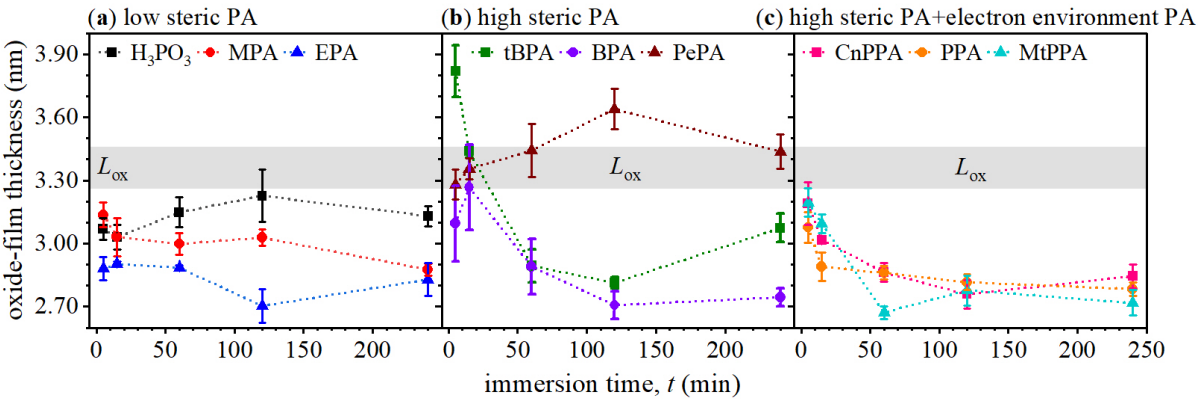

Figure 4.5. *Average thickness of the PA modified aluminum oxide as function of the immersion time for the different groups of PA molecules. Each final thickness value and error bar*

were calculated from three identical, repetitive PA surface treatments (employing the properties of amorphous-Al_2O_3). The grey area denotes the average thickness of the NaOH etched aluminum oxide film, L_{OX} (i.e. prior to PA treatment).

As follows from Figure 4.5, except for PePA, all studied PA molecules exhibit a final oxide film thickness (for $t \geq 120$ minutes) lower than the initial oxide, L_{OX}. This indicates that the PA adsorbed aluminum surface during PA surface treatment are re-oxidized after the water rinsing and air exposure step, forming an oxide film with a final thickness lower than the initial L_{OX} thickness.

The limiting oxide film thickness established upon air exposure of "bare" metallic aluminum surfaces (i.e. without a native oxide film) is well-described by the Cabrera-Mott theory[102-106]: the limiting thickness of the passive oxide film that is practically instantaneously formed on bare metallic aluminum surfaces upon air-exposure, is dictated by the surface-charge field (i.e. the so-called kinetic or Mott potential) induced by charged oxygen species adsorbed on the oxide film surface[102-106]. For instance, the limiting oxide thickness on a bare Al(111) surface increases with increasing partial oxygen pressure and thus with increasing chemical activity of O_2[106]. As follows from the consistently lower final oxide film thickness values in Figure 4.5 (as compared to the initial L_{OX} thickness), the PA adsorbate layers to some extent reduce the chemical activity of oxygen at the interface between the metallic aluminum substrate and the adsorbate PA overlayer during air-exposure, resulting in a slightly lower limiting oxide film thickness as compared to the initial L_{OX} thickness (by NaOH etching). A similar finding has been reported for alkylated silicon surfaces, where bulky alkyl groups more effectively hinder surface oxidation[107].

Group a), low steric PA modified aluminum oxides exhibit the final oxide film thickness independent of the prior immersion time (Figure 4.5), which is consistent with the very fast and complete dissolution of the initial L_{OX} at the onset of the surface treatment (i.e. within 5 min immersion time). The corresponding final oxide film thickness established upon re-oxidation of the bare aluminum surfaces decreases with increasing steric effect from H_3PO_3 → MPA → EPA. Meanwhile, as discussed in Figure 4.2a, adsorbate low steric PA layer converts from the prior aluminum-phosphonate complex after the H_2O rinsing in air, which is a mixture of PA and aluminum oxide/hydroxide. Thus, the increased steric effect of these PA molecules does not increase the stratification of PA layer with aluminum oxide layer. However, the increased PA steric effect reduced the access of O_2 to the adsorbent metallic aluminum substrate. Thus, this reduced re-oxidation process causes a formation of a thinner oxide layer.

Indeed, comparing to high steric PA modified aluminum oxide, e.g. BPA and PPA, the low steric PA molecules, such as H_3PO_3 and MPA, have a larger final (passive) oxide film thickness. However, when the steric effect increased to EPA, the EPA modified aluminum oxide exhibits similar oxide thickness as high steric PA after 120 min. The adsorbate EPA steric effect is a cut-off point between active aluminum re-oxidation (i.e. H_3PO_3 and MPA) and efficient aluminum re-oxidation inhibition (e.g. EPA and BPA).

Group b) and **c)** modified aluminum oxides are discussed together since the effect of electron environment on oxide layer thickness is negligible. Noteworthy, for the high steric molecules in Figure 4.5 b and c (except for tBPA and PePA), the PA modified aluminum oxide film thickness is very similar to the initial L_{OX} thickness for $t \leq 15$ minutes, but then steadily decreases with increasing immersion time, approaching a roughly constant final thickness for $t \geq 120$ minutes. The final thickness for $t \geq 120$ minutes is very similar for all high steric molecules (and also comparable to that of EPA). As discussed in Chapter 3[32], with increasing steric effect, the PA chemisorption rate is increased, whereas the aluminum dissolution rate is decreased. As illustrated in Figure 4.6a, the associated lower aluminum dissolution rate also leads to a slower dissolution of initial L_{OX} film. Meanwhile, the dissolved unstable chemisorbed PA-aluminum fragments (as illustrated in Chapter 3, Figure 3.1, K7) are further hydrolysis or directly interacting with other phosphonate anions forming a gradual increase of the aluminum-phosphonate complex in the solution. This also implies that, for the high-steric molecules, the initial L_{OX} oxide film might not yet be fully dissolved for short immersion times. Thus, for short immersion time, the final thickness rather reflects the remaining thickness of a mixture of initial L_{OX} and re-oxidized aluminum oxide (note as L_{REOX} in Figure 4.6), which could rationalize the initial decrease of the final oxide film thickness with time for BPA, CnPPA, PPA and MtPPA in Figure 4.5b and c. Only if the L_{OX} film is completely dissolved, the final oxide film thickness reflects the re-oxidized film thickness of the bare metallic aluminum, which shows constant oxide film thickness as a function of time (as governed by the Mott potential).

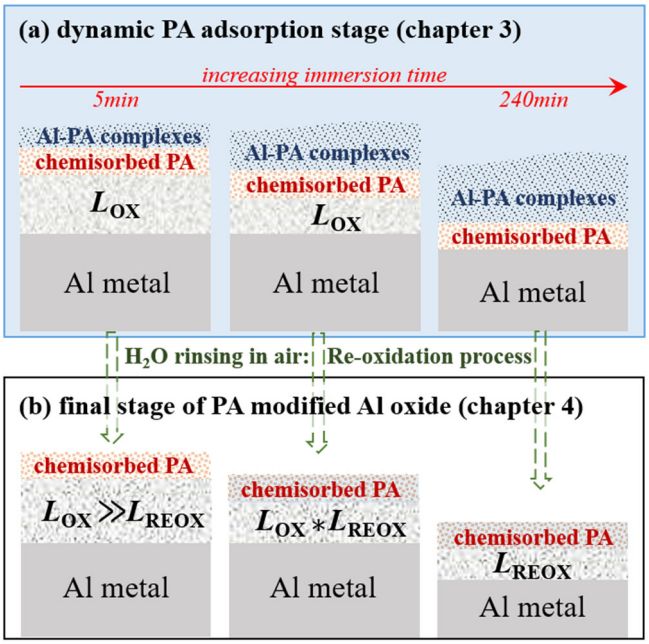

Figure 4.6. *Sketch of the initial aluminum oxide (L_{OX}) dissolution with time in high steric PA solutions except PePA: (a) dynamic PA adsorption stage and (b) final stage of PA modified aluminum oxide (after H_2O-rinsing and air-exposure). This sketch also includes the information on evolutions of the aluminum-phosphonate (Al-PA) complexes, chemisorbed PA layer as well as of the underlying oxide film. The red layer denotes the PA adsorbate layer formed by the condensation reaction, while the blue layer denotes the ionic diffusion barrier layer formed by low-soluble Al-PA complexes. L_{OX} represents the initial or remaining oxide layer before PA treatment. L_{REOX} denotes the oxide layer formed by re-oxidation of the metallic aluminum underneath the adsorbate layer after H_2O-rinsing and air-exposure (i.e. after the PA treatment).*

tBPA exhibits higher aluminum oxide thickness than initial L_{OX} for t< 5 min, as displayed in Figure 4.5b. This might be because the special molecular structure (tert-butyl group) attracts extra aluminum cations on surface, and thus leads to a more porous surficial oxide film during aluminum re-oxidation process in air. When the same aluminum oxide parameters are used to calculate the oxide thickness, tBPA presents as a thicker oxide layer, whereas it might actually result from a loose oxide film. This work is not able to distinguish this difference. However, tBPA also exhibits a gradual decrease of aluminum oxide thickness over time, which is the same case as other high steric PA molecules as illustrated in Figure 4.6.

Finally, as follows from Figure 4.5b, the PePA modified aluminum oxide displays a similar thickness as the initial L_{OX} thickness (within the experimental error), independent of the immersion time. This matches very well with its very high stratification factor as attributed to strong chemisorption on aluminum oxide surface and pronounced van der Waals interactions

among 2-phenyl ethyl groups, which very effectively block initial L_{OX} dissolution. Consequently, the values of the final oxide film thickness for the different PePA treatments are approximately the same as the initial L_{OX} film thickness (after NaOH etching).

4.1.5. Oxygen Auger Parameter

The resolved binding energy (BE) positions of the oxidized Al 2p and the P 2s main peaks are plotted versus immersion time for the different groups of PA molecules in Figure B.7 of Appendix B. For the low steric PA modified aluminum oxide, the oxidized Al 2p and P 2s binding energy (BE) values are roughly time-independent and equal for H_3PO_3, MPA and EPA, which is consistent with the conversion from Al-PA complexes to chemisorbed state on the re-oxidized aluminum surface (L_{REOX} in Figure 4.6), after the H_2O-rinsing and air-exposure. For the high steric molecules (except for PePA), the oxidized Al 2p and P 2s BE values decrease with increasing immersion time, which might indicate similar information as discussed in Figure 4.5 and 4.7, i.e. the adsorbent gradually transfers from mixture L_{OX} and L_{REOX} to a complete L_{REOX}. Meanwhile, PePA modified aluminum oxide exhibits constant Al 2p and P 2s BE values due to the invariable adsorbent, L_{OX}. It is also evidenced by the similar Al 2p BE values of PePA modified aluminum oxide to L_{OX}.

Notably, the oxidized Al 2p and P 2s main peaks shift in the same BE direction and with a very similar magnitude for any given PA molecule. Such highly correlated shifts of the BE peaks as a function of immersion time are a strong indication of shifts in the Fermi level due e.g. band bending and/or differential charging effects [108]. Hence, these correlated oxidized Al 2p and P 2s shifts cannot be unambiguously attributed to changes in the chemical environment or defect structure of the oxide film, but might be partially due to (unknown) electron environment effects in oxide. To isolate the effect of a change in the local chemical environment from any electron environment effects in aluminum oxide, chemical state analysis of the oxygen anions in the oxide film was performed on the basis of the Auger parameter.

Auger parameter value (α) directly relates to the local electronic polarizability around the core-ionized atom involved in the photoemission process and is thus very sensitive to any changes in the nearest coordination sphere of the core-ionized atom [109]. In this chapter, only the Auger α_O is calculated as summary of the most intensive oxygen core level photoelectron line binding energy (BE_O 1s) and the kinetic energy of oxygen sharpest core-core Auger transition (KE_O KLL): $\alpha_O = \text{BE\_O 1s} + \text{KE\_O KLL} = \text{BE\_O 1s} + h\nu - \text{KE\_O KLL}$, where hν is the AlKα X-ray excitation energy (1486.6 eV).

The chemical properties of alkaline etched and various PA treated aluminum oxides are comparing by their oxygen Auger parameters combining with literature value of α-Al_2O_3 and α-$Al(OH)_3$[109], as shown in Figure 4.7. A representation of the oxygen Auger parameter is obtained by plotting KE_O KLL on the ordinate and BE_O 1s on the abscissa (in the negative direction) (the so-called Wagner plot). Lines of constant Auger parameter values are represented by a diagonal grid of slope = -1, where all the points line on the same line have the same final state of a doubly core-ionized atom in an extra-atomic environment; i.e. mainly nearest-neighboring atoms in so-called first coordination shell.

Since different PA modified aluminum oxide layer thickness is stable after 120 min (as discussed in Figure 4.5), only 120 min PA treated aluminum oxides are compared in this discussion to avoid the influence of different amount of remained L_{OX}. All studied PA molecule modified aluminum oxides and L_{OX} have similar α_O values around 1039.5±0.2 eV between α-Al_2O_3 (1038.82 eV) and α-$Al(OH)_3$ (1040.23 eV). It indicates the oxygen extra-atomic polarizability in these aluminum oxide layers after different PA treatments are similar to L_{OX} with small variation in the amorphous oxide structure, which is not interpreted at this stage of the study.

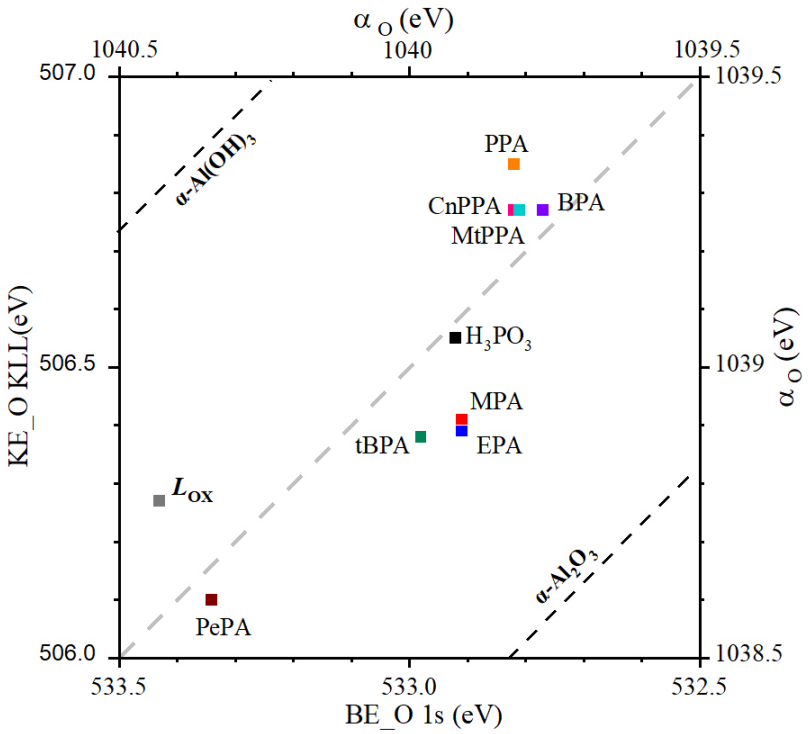

Figure 4.7. *Wagner plot of oxygen binding energy (BE_O_1s) and oxygen kinetic energy (KE O_KLL) of various PA modified aluminum oxides after 120 min, where a constant oxygen Auger parameter (α_O) is shown as grey dash line. L_{OX} shows the oxygen final state before PA treatment.*

As summary, varied PA steric effect changes the adsorbed PA stratification with aluminum and aluminum oxide layer thickness. It is interesting to plot these two aspects together: stratification factor, θ_{PA}, as Y-axis and aluminum oxide thickness as X-axis, as shown in Figure 4.8. The average values of θ_{PA} and aluminum oxide thickness with 120 min and 240 min treatment period are used since the adsorbed PA layer and aluminum oxide are stable with time evolution. With the increase of PA molecular steric effect (Figure 4.8, dashed arrow), there is an increasing trend to form a compact adsorbed PA layer on a thinner aluminum oxide surface. Except for PePA, the initial L_{OX} film is dissolved after 120 min and aluminum re-oxidation process is hindered with the increase of PA steric effect. Meanwhile, one also finds an increased stratification factor of higher steric PA due to higher coverage by single PA molecule and slightly increased number of adsorbed PA by enhanced Van der Waals interaction among functional groups. However, when the steric effect increased to PePA, the PA surface treatment mechanism is different to the others: PePA layer adsorbs efficiently on initial aluminum oxide (L_{OX}) and the adsorbate PA molecules on surface are increased due to the strongly increased Van der Waals interaction.

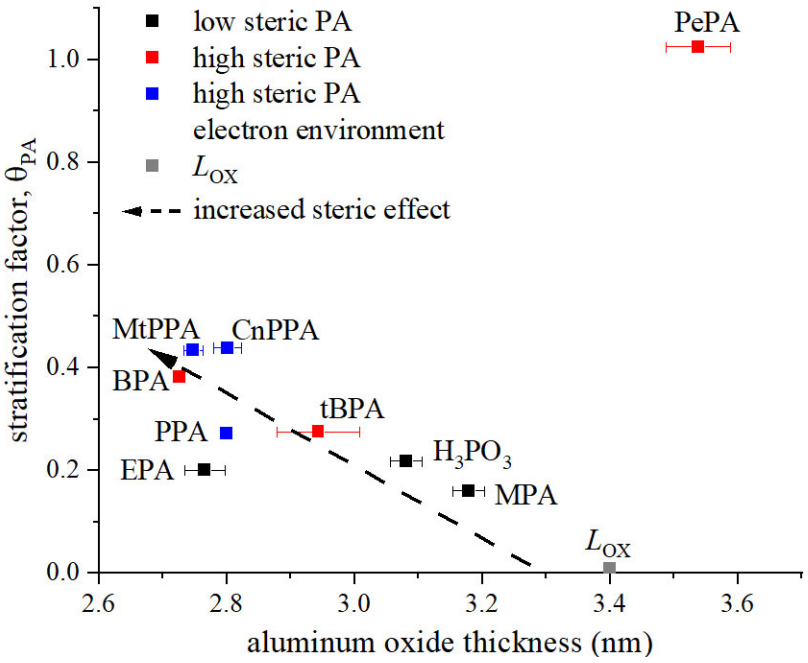

Figure 4.8. *PA molecular steric effect on stratification factor and aluminum oxide thickness after 120 min treatment time, where the dashed arrow shows the trend of increased PA steric effect and the initial aluminum oxide thickness before the PA treatment is denoted as* L_{OX}.

4.1.4. PA Interaction Mode with Aluminum Oxide

To this end, the binding mode of the phosphonic anchor group to aluminum oxide surface is characterized by ToF-SIMS. The fragments containing $Al_xPO_3H_y$ are selected in this discussion because they are representative for complete fragments of PA anchor group binding with aluminum oxide, as displayed in Figure 1.2 of Chapter 1. The existing frames on PA modified surface are presented in Figure 4.9. Only PA modified aluminum oxides after 240 min are used for ToF-SIMS study to ensure similar adsorbent, L_{REOX}, as discussed in Figure 4.5. As shown in Figure 4.2, H_3PO_3 is chosen to represent the PA layers with θ_{PA} value around 0.2; and PPA is chosen to represent the PA layers with θ_{PA} value around 0.3; finally MtPPA is chosen to represent the PA layers with θ_{PA} value around 0.4. Due to the self-assembly effect in PePA layer densification over time, 5 min and 240 min PePA treatment time are compared as well. The original measured spectrums are shown in Appendix B, Figure B.8.

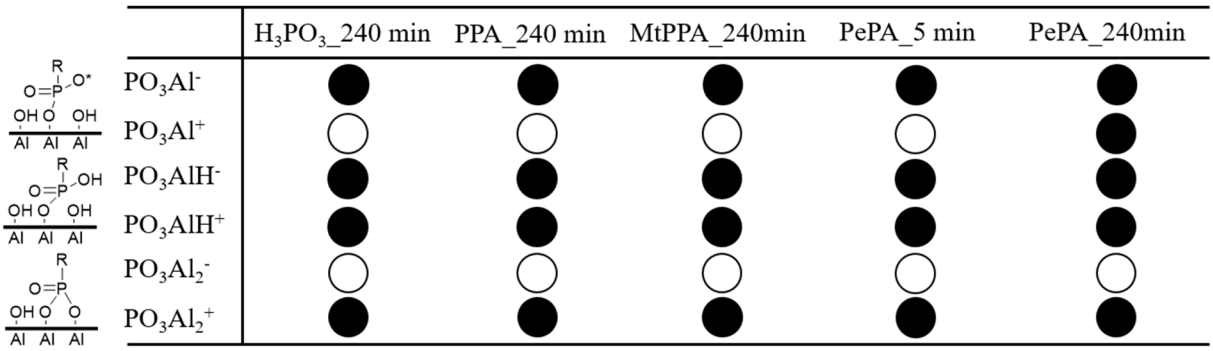

Figure 4.9. *ToF-SIMS surface characterization of PA layer binding mode with aluminum oxide surface: the solid circles indicate existing fragment, and hollow circles indicate absent fragment. The criterion for detection (solid circle) is based on signal to noise ratio; see also Appendix B Figure B8.*

The analysis shows that PA molecule interaction modes with aluminum oxide surface are in a mixture of monodentate and bidentate. The presence of mono/bi-dentate interaction modes on H_3PO_3 modified aluminum oxide shows that the physisorbed Al-PA complexes on metallic aluminum surface partly convert to chemisorbed PA on aluminum oxide after H_2O rinsing in air.

With different molecular steric and electron environment effects, H_3PO_3, PPA and MtPPA modified aluminum oxides after 240 min exhibit similar secondary ion fragments after stabilization process (i.e. H_2O rinsing in air). This means different PA molecular steric or electron environment effects do not change the phosphonic acid group interaction mode with aluminum oxide. Meanwhile, PePA layer shows the similar binding modes at initial 5 min comparing to

other PA molecules after 240 min treatment time. It indicates that PA interaction modes with initial NaOH etched aluminum oxide (i.e. PePA_5 min) and re-oxidized aluminum oxide (i.e. H_3PO_3, PPA and MtPPA_ 240 min) are similar to each other. However, PePA layer on the aluminum oxide surface after 240 min treatment shows additional PO_3Al^+, which is absent for other PA modified aluminum oxides. This PO_3Al^+ fragment might come from the hydroxyl group (-OH) interaction with neighboring monodented oxygen of P=O due to a PePA layer densification, illustrated in Figure 4.11.

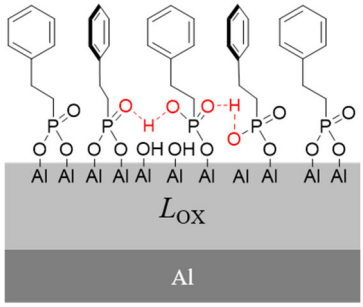

Figure 4.11. *Sketch of PePA interaction with neighboring molecules on the aluminum oxide surface after 240 min treatment; T-shaped conformation of π-π interaction is chosen since it's one of the energetically favored configurations.*

4.2. Conclusion

The molecular steric effect is a key factor that changes the adsorbed phosphonic acid (PA) layer and aluminum oxide layer thickness when the aluminum sheet is removed from acidic PA solution and rinsed by H_2O in air. After immersion in PA solution, the final H_2O-rinsing and air-exposure process generates an aluminum re-oxidation process and stabilizes the surface.

Low steric PA molecules remove the initial aluminum oxide (L_{OX}) and PA molecules assemble on surface in a less compact monodentate & bidentate covalent binding mode. This chemisorbed PA layer converts from prior physisorbed aluminum-phosphonate complexes after the stabilization and oxidation via H_2O ringing in air. Note that most of the prior physisorbed Al-PA complexes were removed after H_2O rinsing, but only the complexes in close contact with the active metal aluminum surface are transformed into the chemisorbed state synergistically with the aluminum re-oxidation process in the air. This conversion process also causes a mixture of PA molecules and aluminum oxide/hydroxide on surface, leading to a low stratification of PA layer and aluminum oxide layer. Meanwhile, when the steric effect increases to EPA, adsorbed EPA starts to hinder the aluminum re-oxidation process of metallic aluminum substrate, which leads to a thinner oxide layer comparing to H_3PO_3 and MPA. Due to the constant adsorbent aluminum surface during the prior adsorption process, and the Al-PA conversion as well as re-oxidized aluminum formation mechanisms, the adsorbate PA layer stratification with adsorbent aluminum oxide and the oxide layer thickness are constant from 5 min to 240 min.

Except for PePA, **high steric PA** and **high steric PA with varied electron environment** form adsorbate layers with higher and time-independent stratification factor comparing to low steric PA layers. Meanwhile, these PA molecules require a time-consuming process (60~120 min) to dissolve initial aluminum oxide (L_{OX}) due to the inhibition of chemisorbed PA molecules during the prior adsorption process. This causes a gradual decrease of PA modified aluminum oxide until L_{OX} is completely dissolved. Meanwhile, the high steric effect leads to a hindering effect of aluminum re-oxidation process similar to EPA.

However, with the highest steric effect, PePA protects initial L_{OX} from initial 5 min and adsorbs on it. The π-π stacking among 2-phenylethyl groups of PePA results into an increase of the PePA adsorbed molecules on the surface over time (120 min) until surface saturation. Moreover, the additional degree of freedom to rotate the phenyl ring of PePA might be a prerequisite for this densification process.

It is important to note that the PA molecular electron environment effect on the adsorbate PA layer and the aluminum re-oxidation process is negligible in this Chapter 4. Whereas, in the dynamic adsorption process discussed in Chapter 3, the electron environment exhibits a significant effect on PA chemisorption on aluminum surface. One of the hypotheses is that the air-exposure step might equalize the difference of CnPPA/MtPPA modified oxides due to the strong aluminum re-oxidation. Thus, in the next Chapter 5, the PA surface treatment on aluminum oxide substrate is performed in a glovebox to reduce the partial O_2 pressure, which reveals the effect of PA molecular electron environment effect on aluminum oxide.

Chapter 5. Interactive Effects between Phosphonic Acid Structure and Aluminum Re-Oxidation

This chapter is adapted from a manuscript in preparation with multiple co-authors: Zhao R, Patrik S, Gaan S, Cancellieri C, Jeurgens L P H and Heuberger M. The major part of this work was done by Zhao R. Cancellieri C supervised the XPS/HAXPES and XRD characterization. Patrik S, Gaan S, Jeurgens L P H and Heuberger M contribute to the discussion and correction of the scientific text.

The PA molecular structural effect on PA dynamic adsorption process and the final PA modified aluminum oxide has been discussed in Chapter 3 and 4 respectively. PA molecules with different electron environments cause different aluminum dissolution activity but result in a similar final modified surface. The strong aluminum re-oxidation process during H_2O-rinsing and air exposure after PA adsorption process might equalize the effect of PA molecular electron environment on adsorbent aluminum surface. To test the hypothesis that different molecular electron environment of PA modified aluminum oxides are eventually equalized by re-oxidation upon ex-situ transfer, in this chapter a novel system is used to reduce the partial O_2 pressure in this chapter: glovebox, sputter chamber and X-ray/hard X-ray photoelectron spectroscopy (XPS/HAXPES) connected via ultra-high vacuum (UHV) transfer system. In this way, a fresh physical vapor deposited (PVD) aluminum on silicon substrate is created and transferred directly to glovebox through the UHV connection system; PA treated aluminum oxide in glovebox can be characterized by XPS/HAXPES in situ without further oxidation or contamination in air. PA surface treatment time is 5 min in both glovebox and air since the PVD aluminum film is only 500nm and a longer deposition time increases the H_2O in glovebox enormously. Two PA molecules with opposite inductive effect on phosphonic acid anchor group are used to modify aluminum oxide in glovebox: i.e. (4-cyanophenyl)phosphonic acid (CnPPA) with electron withdrawing effect, and (4-methoxyphenyl)phosphonic acid (MtPPA) with electron donating effect. Meanwhile, oxygen and aluminum Auger parameters are used to investigate the changes of PA modified aluminum oxides. As a reference, amorphous and crystalline aluminum oxides/hydroxides are also characterized (introduced in Chapter 2, section 2.3.3). This chapter starts with surface characterization of reference aluminum oxides/hydroxides using oxygen and aluminum Auger parameters. Then the effects of PA molecular electron environment and O_2

concentration are compared by using CnPPA and MtPPA to modify aluminum oxide in glove-box and air.

5.1. Results and Discussion

5.1.1. Auger Parameter

Different to other conventional XPS characterization, the current study uses an in situ X-ray (Al kα) and hard X-ray (Cr kα) combined photoelectron spectroscopy (XPS and HAXPES respectively), which provides access not just to analysis O 1s, Al 2p or oxygen Auger peak (O KLL) but also to aluminum Auger peak (Al KLL) of PA modified aluminum oxide, as shown in Appendix C, Figure C.2.

Chapter 4 shows that after PA treatment, the PA modified aluminum oxide exhibited an amorphous structure. Different chemical states of aluminum oxides are normally difficult to discern by photoelectron peaks (binding energy) due to the differential charging in an amorphous structure. Due to the charging effect and the existing of initial aluminum oxide, the effect of PA molecule on top oxide surface might be hard to extinguish from binding energy shifts. Therefore, it is essential to utilize the oxygen and aluminum Auger parameter to distinguish the minor changes of aluminum oxide because Auger parameter is independent of the charging effect, and sensitive to local electronic polarizability and structural changes in the nearest coordination sphere of the core-ionized atom[109]. The Auger parameter of an analyzed oxide can be expressed as:

$$\Delta\alpha = \Delta KE + \Delta BE \approx 2\Delta R. \tag{5.1}$$

Since photoemission and subsequent Auger relaxation are very fast electronic processes, the energy contribution of atomic rearrangements in the surrounding structure is assumed to remain approximately invariant; $\Delta\alpha$ is then also a measure for, ΔR, which is the collective relaxation energy of the extra-atomic electronic system[110]; this can be seen as electronic polarizability of the environment upon core-hole formation. This polarizability is sensitive to structural changes (e.g. Madelung constant) in the nearest coordination sphere of the core-ionized atom[109]. A useful visualization of the Auger parameter is obtained in the so-called Wagner plot, where the Auger electron kinetic energy is plotted on the ordinate and the core-level binding energy on the inverted abscissa[111]. The relative position of each compound gives information on the core hole shielding provided by the ligand environment and the relative covalence of the bonding. From the definition of Auger parameter shown in equation (5.1), α, and as

reviewed in reference[112], we can state that the line of constant Auger parameter (i.e. constant final state effect) comes with a slope = -1 in the Wagner plot:

$$KE=\alpha-BE \quad (5.2)$$

The final state refers to the energy at the final state of a doubly core-ionized atom in an extra-atomic environment; i.e. mainly nearest-neighboring atoms in so-called first coordination shell.

Additionally, the probing depth of emitted electrons depends on their kinetic energy: $3\lambda \times \cos\theta$ (nm), which is important when analyzing stratified systems, i.e. top aluminum oxide layer on metallic aluminum substrate. For the oxygen Auger parameter, the O 1s binding energy and O KLL kinetic energy is obtained from the same XPS measured spectrum due to similar kinetic energy; i.e. similar probing depth of 4.9 nm and 3 nm respectively. However, for aluminum Auger parameter, the determined Al 2p binding energy and Al KLL kinetic energy from HAXPES have a different probing depth: 6.2 nm and 19.3 nm respectively. In order to keep the aluminum Auger parameter analysis at a similar probing depth, the determined Al 2p binding energy and Al KLL kinetic energy are from XPS and HAXPES respectively since they have similar kinetic energy providing similar measuring depth (c.a. 6.4 nm)[113]. Thereby, we lose the advantageous cancellation of charging effects when working with only one spectrum, but we carefully calibrated both energy scales using Al2p and C1s signals. Combing photoelectron with Auger peaks analysis, the different chemical states can be discriminated at a typical accuracy around ±0.1eV.

It is important to note here the PA modified aluminum oxide has multiple aluminum oxide components in depth, i.e. aluminum hydroxide/oxide interacting with PA, aluminum oxide, and sub-oxide contacting with metallic aluminum. This work is not able to obtain the oxygen and aluminum Auger parameters for each component due to the lack of the pre-knowledge of O KLL and Al KLL deconvolution. Thus, the Auger parameter presented in the following discussion is an average of extra-atomic polarizability.

5.1.2. Reference Aluminum Oxides/Hydroxides

5.1.2.1. Core Level Analysis

The single crystalline aluminum oxide (α-Al_2O_3, Sapphire) and polycrystalline aluminum hydroxide (α-$Al(OH)_3$, Bayerite) are studied as the reference for different amorphous aluminum oxides/hydroxides. Crystal aluminum oxide/hydroxide are prepared in air, and then transferred through glovebox to HAXPES/XPS surface characterization. The measured O 1s peak shows

that a higher aluminum hydroxylated state exhibits higher binding energy, as shown in Figure 4b[81, 112]. The valence band shows an energy gap from 0 eV to 4 eV for three samples (Figure 4d); though the crystal structure is guaranteed by XRD (Appendix C, Figure C.1), the double peak shapes of the upper valence band region from 5 eV to 11 eV are typical for crystalline oxide structure as shown in Figure 5.1d [114-117]. Meanwhile, different amorphous aluminum oxides/hydroxide are compared. These samples are created by exposing PVD aluminum into various environments, i.e. glovebox (Al-O GB), air (Al-O air), and low-oxygen H_2O immersion in glovebox (Al-O+H_2O GB). As discussed in Chapter 4 section 4.2.1.1[7, 8], the featureless plateau shape of the valence band region from 5 to 14 eV (Figure 5.1d) proves "Al-O GB", "Al-O air" and "Al-O+H_2O GB" are amorphous structures. Note that the signal in the binding energy range from 0 to 5 eV contributes from the conduction band of the underlying metallic aluminum substrate [98].

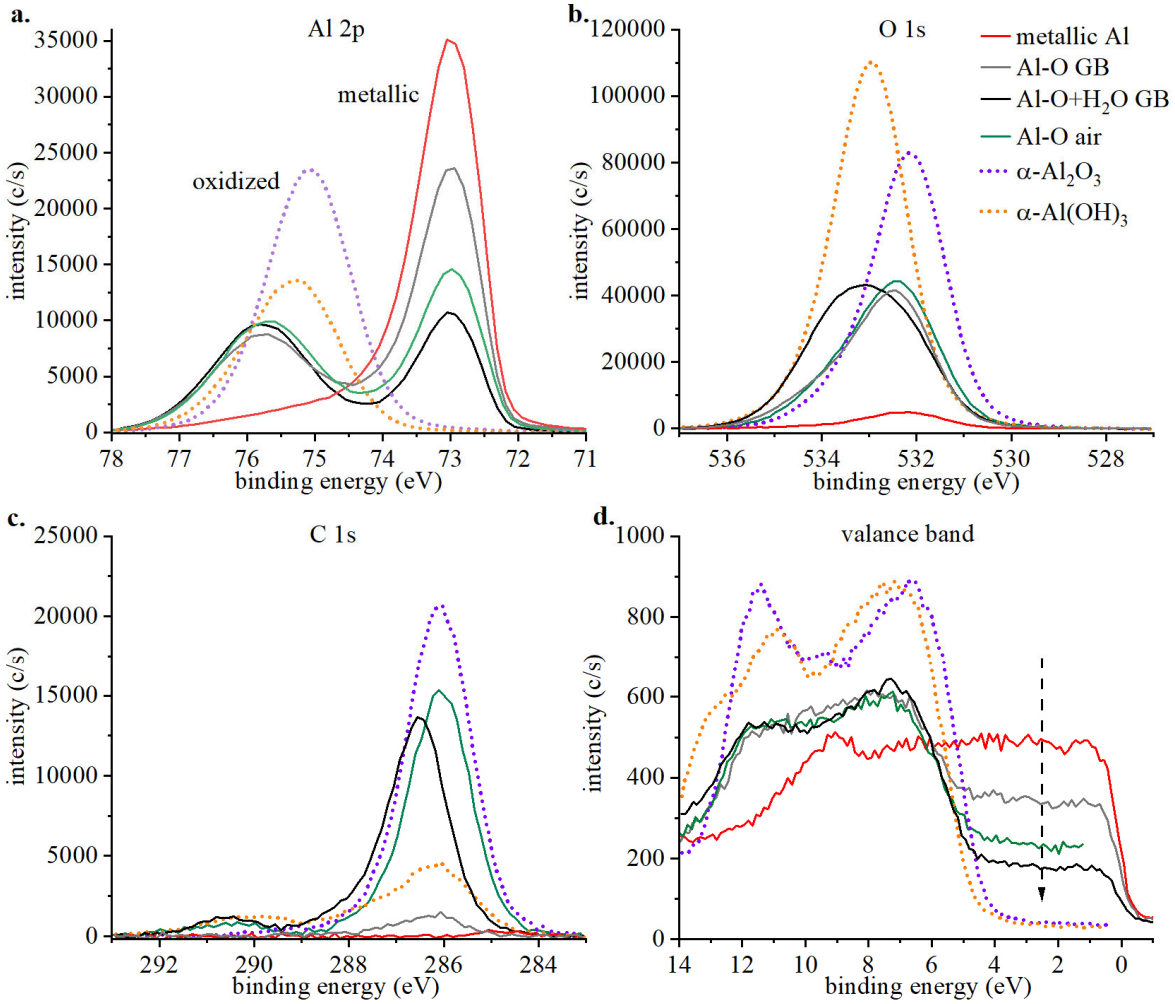

Figure 5.1. *XPS measured photoelectron peaks of reference aluminum oxides/hydroxide: a) is Al 2p peak, b) is O 1s peak, c) is C 1s peak, and d) is valence band. α-Al_2O_3 is Sapphire; α-*

$Al(OH)_3$ is Bayerite; "metallic Al" is a PVD aluminum directly transferred from sputter chamber to XPS/HAXPES chamber via vacuum transfer system; 'Al-O GB' is a native aluminum oxide grown on PVD aluminum in glovebox; 'Al-O+H_2O GB' is a PVD aluminum firstly transferred to GB followed with 5 min H_2O immersion, then dried under vacuum for 30 min; 'Al-O air' is a native aluminum oxide grown on PVD aluminum in air.

The vacuum transfer system is checked firstly by direct transferring a PVD aluminum from sputter chamber to XPS/HAXPES chamber, as illustrated in Chapter 2, Figure 2.4, green arrow ①, namely "metallic Al". Surface characterization of "metallic Al" shows that the vacuum transfer system prevents aluminum oxidization and air contamination, which is evidenced by extremely low oxidized Al 2p, O 1s and C 1s peaks as shown in Figure 5.1a, b and c respectively. When this "metallic Al" exposes to glovebox, air and H_2O in glovebox, a decrease of metallic Al 2p intensity is observed with similar oxidized Al 2p intensity, as shown in Figure 5.1a. It means the aluminum oxidation increases sequentially: "metallic Al"< "Al-O GB"< "Al-O air" < "Al-O+H_2O GB". This is also evidenced by valence band as shown in Figure 5.1d, dash arrow. "Metallic Al" shows a broad conductive band near the Femi level (0~4 eV); while this conductive band intensity decreases ("Al-O GB"> "Al-O air"> "Al-O+H_2O GB") with the increase of aluminum oxidation (oxide film thickness). Until the metallic aluminum phase is out of XPS detection range, three crystalline aluminum oxide/hydroxides exhibit a band gap at 0~4 eV zone. The Al 2p and valence band results indicate that glovebox can effectively decrease the aluminum oxidation comparing to air exposure. Meanwhile, immersion of PVD aluminum in H_2O in glovebox not just increases the oxidation, but also creates additional hydroxide on surface. As shown in Figure 5.1b, O 1s peak of "Al-O+H_2O GB" exhibits a broad peak with FWHM of 2.8 eV, which is a peak envelope of oxygen signal from aluminum oxide, aluminum hydroxide. Meanwhile, O KLL peak of "Al-O+H_2O GB" also exhibits a broader shoulder at the low binding energy side of O KLL peak as shown in the Appendix C, Figure C.3 (dash arrow). This additional shoulder of O KLL is typically contributed by increased aluminum hydroxide[118]. Additionally, "Al-O+H_2O GB" also shows significant amount of carbon containments similar to "Al-O air". Thus, one hour Argon-flow deaerated process of H_2O is not able to completely remove initial dissolved CO_2 in H_2O. Note that the C 1s binding energy of "Al-O+ H_2O GB" is c.a. 0.6 eV higher than other air-exposed surfaces, which might result from the difference of dissolved CO_2 in water and airborne carbonaceous contamination. The core level analysis of

reference amorphous aluminum oxide shows that the native aluminum oxide formed in glovebox is thinner than the oxide formed in air. Meanwhile, 5 min immersion in H_2O in glovebox creates additional aluminum hydroxide on the surface.

5.1.2.2. Auger Parameter Analysis

The oxygen Auger parameter (α_O) is calculated as the sum of oxygen Auger kinetic energy (KE_O KLL) and O 1s binding energy (BE_O 1s): $\alpha_O = KE\_O\ KLL + BE\_O\ 1s$. The XPS and HAXPES measured O KLL and Al KLL are shown in Appendix C, Figure C.3 a and b respectively. The calculated oxygen and aluminum Auger parameter values are displayed in Appendix C, Table C1. Note that, the core level analysis shows that " Al-O+H_2O GB" displays a mixed hydroxide/oxide layer. Due to the lack of pre-knowledge of O KLL peak deconvolution, the α_O is calculated using the binding energy of the maximum peak envelope of O 1s and O KLL, which represents an average value of α_O of the multi-components.

By plotting the KE_ O KLL vs BE_O 1s values, a Wagner plot is obtained. The corresponding data is plotted in Figures 5.2 a) and b) where lines of slope -1 connect chemical states of comparable extra-atomic polarizability according to equation (5.2). For amorphous aluminum oxide, "Al-O GB" and "Al-O air" display similar α_O values, which indicates different oxidation (different oxide film thickness) in glovebox or air does not change the oxygen extra-atomic polarizability inside the amorphous aluminum oxide. However, with a mixture of additional aluminum hydroxide component, the average oxygen extra-atomic polarizability of "Al+H_2O GB" is increased presenting as an increased α_O value than "Al-O GB". In aluminum hydroxide, the electron density of oxygen is reduced by sharing valence electron with hydrogen; thus, the binding energy of O 1s is increased, which would contribute to the increase of α_O value; this is under the assumption that the hydroxylation process generates similar O KLL kinetic energy referring to the similar O KLL of α-$Al(OH)_3$ and α-Al_2O_3. This shows that α_O is sensitive to detecting the formation of aluminum hydroxide in an amorphous structure even it is an average value.

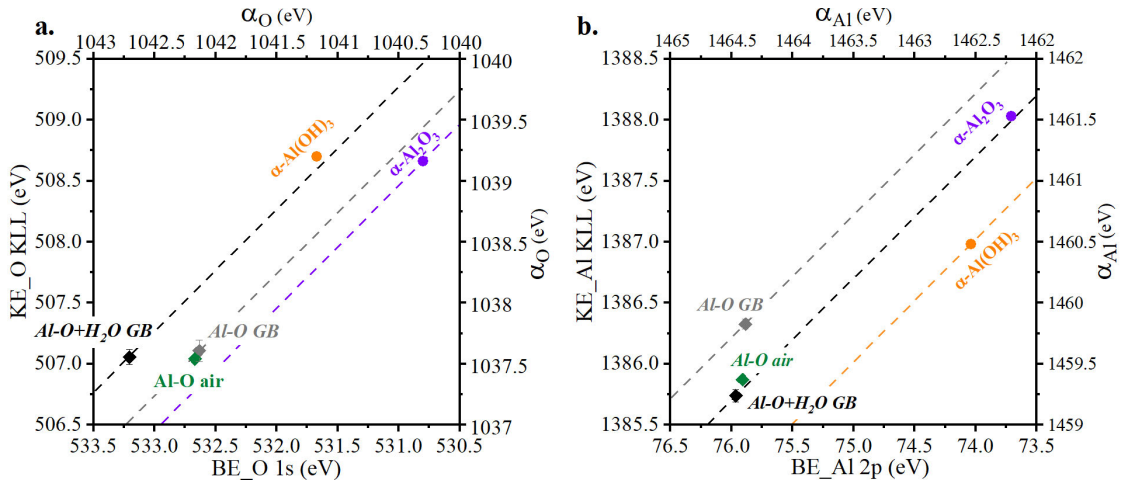

***Figure 5.2**. XPS measured oxygen Auger parameter (a.) and XPS/HAXPES measured aluminum Auger parameter (b.) of aluminum oxides/hydroxide without PA treatment, where GB presents for treatment in glovebox, the dash line with slope=-1 presents for a constant Auger parameter value. Crystal aluminum oxide/hydroxides are plotted as cycle shapes: α-Al_2O_3 is Sapphire; α-$Al(OH)_3$ is Bayerite. Amorphous aluminum oxides/hydroxides on PVD aluminum substrate are plotted as diamond shapes: "Al-O GB" is a native aluminum oxide grown in glovebox; "Al-O air" is a native aluminum oxide grown in air; "Al-O+H_2O GB" is a native aluminum oxide immersed in H_2O in glovebox.*

The aluminum Auger parameter (α_{Al}) is calculated as the summary of oxidized aluminum Auger kinetic energy (KE_Al KLL) measured by HAXPES and oxidized Al 2p binding energy (BE_Al 2p) measured by XPS since they have similar kinetic energy providing similar measuring depth (c.a. 6.4 nm)[113]: $\alpha_{Al} = KE\_Al\ KLL + BE\_Al\ 2p$. The calculated α_{Al} values are presented in Appendix C, Table C1. When aluminum is directly transferred to XPS/HAXPS, "Metallic Al" exhibits high α_{Al} value of 1466 eV; whereas α_{Al} values in aluminum oxides are reduced because the screening effect of aluminum atom is reduced sharing electrons with oxygen in aluminum oxide (Figure 5b).

The α_{Al} values of reference aluminum oxides/hydroxides increase in the sequence of α-$Al(OH)_3$ < α-Al_2O_3 ≈ "Al-O air" ≈ "Al-O+H_2O GB" < "Al-O GB". Aluminum oxidation is strongly suppressed in glovebox. The screening effect of aluminum atoms in the native amorphous aluminum oxide film formed in glovebox (Al-O GB) is significantly enhanced by the proximity of the metallic aluminum substrate[119]. However, with the increase of aluminum oxidation, the effect of metallic aluminum phase does not exhibits in "Al-O air" and "Al-O+H_2O GB". It is interesting to note that a hydroxylated aluminum oxide (Al-O+H_2O GB) and a native amorphous aluminum oxide formed in air (Al-O air) display similar α_{Al} value, which is similar

to a crystalline structure (α-Al_2O_3). Similar α_{Al} values of "Al-O air" and "Al-O+H_2O GB" indicate the average aluminum extra-atomic polarizability is not increased by the hydroxylation of "Al-O+H_2O GB". It is because the increased hydrogens are associated with oxygen atoms but not with aluminum atoms; meanwhile, aluminum atom has a stronger self-screening effect than oxygen atom. Additionally, the local chemical environment of aluminum atom is not changed with the structural transition from crystalline to amorphous[120], thus, α-Al_2O_3 ≈"Al-O air". However, the crystalline aluminum hydroxide (α-$Al(OH)_3$) significantly decreases the α_{Al} value due to the extra hydrogen bond networking[121]. Thus, α_{Al} is sensitive to distinguish ultra-low oxidation due to the effect of metallic aluminum substrate.

As a brief summary of reference amorphous aluminum oxides study, glovebox can largely suppress the aluminum oxidation process; H_2O immersion process hydroxylates the aluminum oxide, which increases the average oxygen Auger parameter. Thus, oxygen Auger parameter is sensitive to the existing of additional hydroxide; aluminum Auger parameter is sensitive to distinguish low aluminum oxidation state.

5.1.3. CnPPA and MtPPA Modified Aluminum Oxides

The electron density of phosphonic acid anchor group is reduced due to the electron withdrawing effect of cyano group in CnPPA, but increased due to the electron donating effect of methoxy group in MtPPA as described in Chapter 1, Figure 1.4[32]. The results show that during the dynamic adsorption process, CnPPA forms an unstable covalent bond with aluminum surface (as illustrated in Chapter 3, Figure 3.1 K7); whereas, MtPPA forms a stable chemisorption and passivates the aluminum surface as discussed in Chapter 3 (as illustrated in Chapter 3, Figure 3.1 K5). However, after H_2O rinsing and air exposure, adsorbate CnPPA and MtPPA layers show same aluminum oxide thickness and same oxygen Auger parameter as discussed in Chapter 4, Figure 4.5 and Figure 4.7 respectively. The H_2O rinsing stops the acidic attack on aluminum oxide surface and air-exposure step oxidized the unstable reactive aluminum sites on surface, which equalizes different PA modified aluminum surfaces in the prior adsorption stage. Thus, CnPPA and MtPPA surface treatment is transferred to glovebox, and compared with the treatment in air. The effect of molecular electron environment and air-exposure on adsorbent aluminum oxide are investigated in detail.

5.1.3.1. Core Level Analysis

Comparing to "Al-O GB", CnPPA/MtPPA modified aluminum oxides in glovebox exhibit higher aluminum oxidation exhibiting a decrease of metallic Al 2p signal as shown in Figure 5a. The featureless plateau shape (5 to 11 eV) of valence bands of PA modified aluminum oxides in glovebox/air indicates similar amorphous structures to "Al-O GB" and "Al-O+H_2O GB" (Figure 5.3c). CnPPA and MtPPA modified aluminum oxides in air show similar peak shape, binding energy and intensity of Al 2p, O 1s, valence band (Figure 5 a,b,c), O KLL and Al KLL (Appendix C, Figure C4 a,b). This is in agreement with results in Chapter 4 that a strong oxidation in air equalizes any difference of CnPPA/MtPPA modified aluminum oxide, i.e. "Al-O+CnPPA air" is similar to "Al-O+MtPPA air".

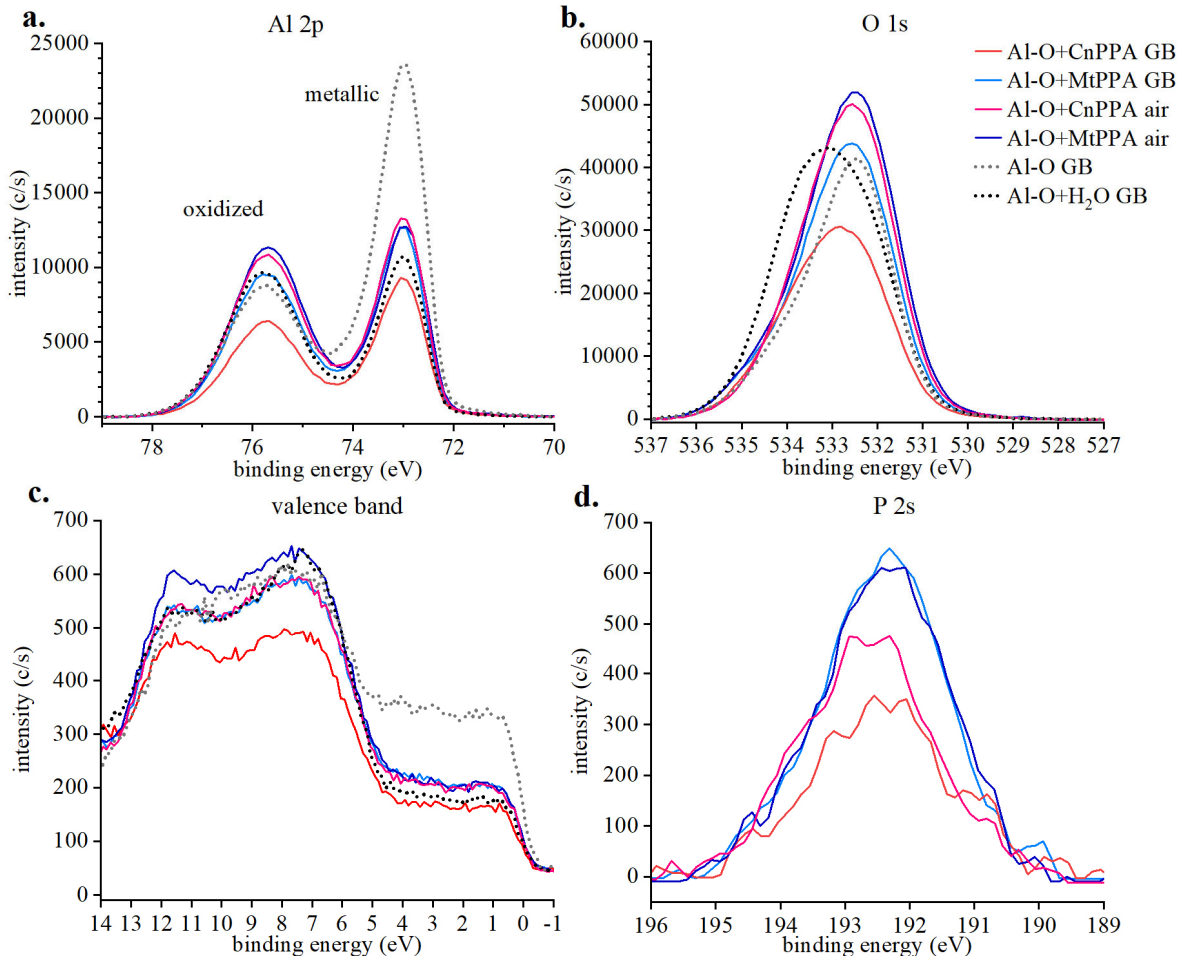

Figure 5.3. *XPS measured photoelectron peaks of PA surface modified physical vapor deposited (PVD) aluminum samples: a) is Al 2p peaks, b) is O 1s peaks, c) is valence band and d) is P 2s peak, where "Al-O+CnPPA GB" is a native oxide formed in glovebox and treated in de-aerated CnPPA solution in glovebox; "Al-O+CnPPA air" is a native oxide formed in air and treated in CnPPA solution in air; for MtPPA treated samples in glovebox and in air are noted as "Al-O+MtPPA GB" and "Al-O+MtPPA air" respectively. Reference aluminum oxides "Al-O GB" and "Al-O+H2O GB" are plotted together as dotted line.*

When the O_2 concentration is limited in glovebox, the O 1s peak of "Al-O+CnPPA GB" shifts to higher binding energy than "Al-O+MtPPA GB". Meanwhile, the unsymmetrical shape and the higher FWHM (2.7 eV) of O 1s peak of "Al-O+CnPPA GB" indicates that CnPPA surface modification creates multiple oxygen components. Meanwhile, O KLL peak of "Al-O+CnPPA GB" also exhibits a broader shoulder at the low binding energy side of O KLL peak comparing to "Al-O+MtPPA GB" as shown in the Appendix C, Figure C.3(dash arrow). This is the similar case to "Al-O+H_2O GB", i.e. this additional shoulder of O KLL is contributed by increased aluminum hydroxide[118]. Thus, CnPPA treatment in glovebox creates additional hydroxide, which is not observed on "Al-O+MtPPA GB" and "Al-O+MtPPA/CnPPA air". During the surface treatment, CnPPA forms unstable chemisorption on aluminum oxide surface, which is not capable to prevent the acidic attack. Thus, after H_2O rinsing in glovebox, the reactive aluminum sites on surface coverts to aluminum hydroxide during 30 min vacuum drying procedure. However, due to the strong oxidation in air, these reactive aluminum sites on surface is oxidized to aluminum oxide. Thus, the additional hydroxide phase only exhibits on "Al-O+CnPPA GB" but not on "Al-O+CnPPA air". Additionally, MtPPA passives the initial aluminum oxide in the 5 min adsorption stage. Thus, there is no additional hydroxide phase on MtPPA surface in glovebox or air. Additionally, due to the unstable chemisorption, there are less CnPPA adsorbed on PVD aluminum oxide surface than MtPPA in air and glovebox as shown in Figure 5.3d. Moreover, when strong oxidation in air is absent in glovebox, H_2O rinsing step may further remove a certain amount of CnPPA.

5.1.3.2. Auger Parameter Analysis

The adsorption stage study shows that CnPPA and MtPPA molecules only modified the surficial-top layer of aluminum oxide with 5 min treatment time. It means the variation of different PA treated aluminum oxides in glovebox or air would be small. Thus, here it is important to state the XPS/HAXPES measurement resolution and the reproducibility of triple samples for each PA treatment condition. The resolution of XPS/HAXPES measured is 0.1 eV; for each PA treatment condition, the standard deviation of triple Auger parameter values represent the reproducibility. Therefore, in the following discussion, when the difference of two Auger parameter values is higher than 0.1 eV and larger than the sum of their standard deviation, these two Auger parameters are considered as different values. The XPS and HAXPES measured O KLL and Al KLL peaks are shown in Appendix C, Figure C.4 a and b respectively. The calculated average oxygen and aluminum Auger parameter values are displayed in Appendix C, Table C.1.

Due to the strong re-oxidation in air, CnPPA and MtPPA modified aluminum oxides exhibit similar α_O values, i.e. "Al-O+CnPPA air" ≈ "Al-O+MtPPA air", as shown in Figure 5.4a. However, in glovebox, the α_O value of "Al-O+CnPPA GB" is 0.2 eV higher than "Al-O+MtPPA GB" (with the sum of standard deviation of 0.15 eV). This increased α_O value of 0.2 eV would be contributed by the additional hydroxide component. As discussed in core level analysis, after H_2O rinsing in glovebox, CnPPA generates reactive aluminum sites during the prior 5 min adsorption stage. The residual H_2O on surface covers these reactive aluminum sites into aluminum hydroxides during 30 min vacuum drying procedure. Additionally, the increased oxygen Auger parameter would also be contributed by the chemisorbed CnPPA molecule. Specifically, with the electron withdrawing group, the CnPPA anchor group electron density is reduced; thus, the electron density of oxygen atom on the oxide surface is further reduced when it is covalent binding with the phosphorus atom of CnPPA. The current work is not able to distinguish whether the hydroxide or chemisorbed CnPPA contributes to increased α_O value, or it is a synergistic effect. However, the effect from adsorbed CnPPA might be minor due to the low P 2s intensity. It is interesting to notice that "Al-O+MtPPA GB/air" and "Al-O+CnPPA air" show similar α_O values, which again suggests that strong air oxidation equalizes the different aluminum oxides modified by CnPPA and MtPPA.

As for the α_{Al} values of MtPPA/CnPPA modified aluminum oxides in glovebox and air, the differences are less than 0.1 eV with high standard deviations, as shown in Figure 5.4b. α_{Al} is not able to distinguish the different PA modified aluminum oxides because firstly, α_{Al} is not sensitive to the hydroxylated state changes on the amorphous aluminum oxide surface as discussed in Figure 3.5; secondly, the adsorbed PA molecules interact with oxygen but not with aluminum. Additionally, it seems like there is a slope = -3 crossing amorphous aluminum oxide with or without PA treatment that represents for the same aluminum initial state[115]. But this is not discussed in the present study with such high standard deviations.

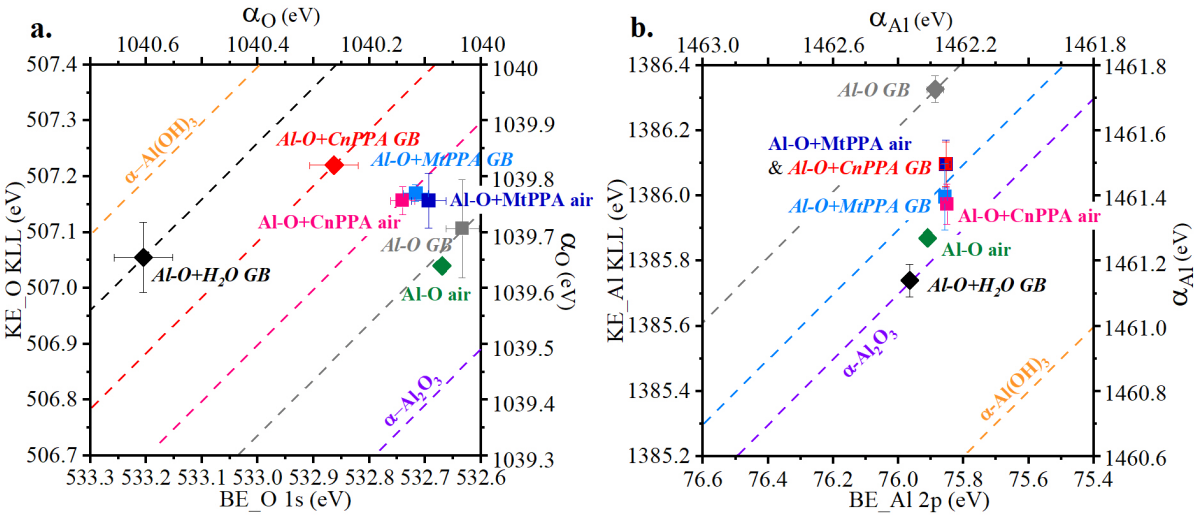

Figure 5.4. XPS measured oxygen Auger parameter (a.) and XPS/HAXPES measured aluminum Auger parameter (b.) of PA modified aluminum oxide (square shape) and reference aluminum oxides without PA treatment, where GB presents for treatment in glovebox and the dash line with slope = -1 presents for a constant Auger parameter value. "Al-O+CnPPA GB" is a native oxide formed in glovebox and treated in deaerated CnPPA solution in glovebox; "Al-O+CnPPA air" is a native oxide formed in air and treated in CnPPA solution in air; for MtPPA treated samples in glovebox and in air are noted as "Al-O+MtPPA GB" and "Al-O+MtPPA air" respectively.

5.2. Conclusion

This work systematically compares the reference crystalline and amorphous aluminum oxides/hydroxide and CnPPA/MtPPA modified aluminum oxide in glovebox and air. The average oxygen and aluminum Auger parameters are calculated by using the binding energy of the maximum peak envelope measured by XPS/HAXPES. From the study of reference aluminum oxides/hydroxide, it is clear that the average oxygen Auger parameter (α_O) is sensitive to detect the presence of hydroxide component, which increases the average oxygen extra-atomic polarizability exhibiting an increased α_O value. Meanwhile, the average aluminum Auger parameter (α_{Al}) is sensitive to detect the effect of nearby metallic aluminum substrate on a thin amorphous oxide layer.

Two phosphonic acid (PA) molecules are used as model PA to modify aluminum oxide surface in glovebox or air. CnPPA with an electron withdrawing molecular environment decreases the electron density of PA anchor group, and MtPPA with an electron donating molecular environment that increases the electron density of PA anchor group. With the comparison of CnPPA treatment in glovebox and air, it is clear that the unstable reactive aluminum surface modified by CnPPA is hydroxylated by H_2O with 30 min vacuum drying and oxidized by O_2 in air-exposure, respectively. Thus, CnPPA modified aluminum oxide in air exhibits a high

average oxygen extra-polarizability (α_O value) than CnPPA surface modified in air due to the additional hydroxide. However, MtPPA passivates the adsorbent oxide barely exhibiting hydroxide phase in glovebox and air.

This work shows that the final stage of PA modified aluminum surface is highly dependent on the exposure atmosphere (e.g. O_2, H_2O) when PA aluminum oxide surface modification uses CnPPA-like molecules (e.g. low steric PA and PPA causing significant aluminum dissolution during prior adsorption process in Chapter 3). Meanwhile, MtPPA-like molecules (e.g. BPA and PePA with stable chemisorption during the prior adsorption process in Chapter 3) passivate the aluminum oxide surface independent of the following exposure atmosphere.

Chapter 6. Conclusion and Outlook

The molecular structural effects of phosphonic acid (PA) molecules on the aluminum oxide surface modification are investigated in this work. PA with varied molecular steric and electron environments are systematically compared. Three different stages covering the whole PA surface treatment process are discussed in Chapter 3 (dynamic PA adsorption stage), Chapter 4 (final stage of PA modified aluminum oxide), and Chapter 5 (air-exposure transition stage between the above two stages). This work has revealed some unexpected facts and mechanisms that are not described or clearly established in the previous literature:

During the dynamic PA adsorption stage, there is a non-equilibrium steady state charge and species transfer process on aluminum surface in PA solution (0.01 M, pH ≈ 2). Note that even in the H_3PO_3 solution that causes the most active aluminum dissolution, this non-equilibrium steady state occurs from 5 min until 240 min in 5 mL H_3PO_3 solution on a pure aluminum sheet with the contacting surface area of c.a. 260 mm^2. This reveals the nature of low-solubility of aluminum-phosphonate complexes acting as an aluminum dissolution barrier.

However, the acidic attack of low steric PA molecules (H_3PO_3, MPA, EPA) on the c.a. 3 nm native aluminum oxide created after NaOH etching (L_{OX}) is still a fast process within 5 min. A high steric PA molecule slows down the aluminum dissolution via chemisorption evidenced by the high aluminum surface impedance. Except for PePA, this chemisorption provides only limited protection on the surface causing a slower dissolution of L_{OX} between 5 min to 120 min, which is deduced from the final stage of aluminum oxide thickness. Due to the high steric effect of PePA (2-phenylethyl group), PePA chemisorbs and passivates the L_{OX} for the entire 240 min immersion time. Additionally, the effect of PA molecular electron environment also varies the stability of chemisorption on the aluminum surface, which is barely considered in previous work. With an electron withdrawing group, the reduced electron density of CnPPA anchor group destabilizes its covalent binding on the aluminum surface. Conversely, MtPPA with an electron donating electron environment stabilizes its chemisorption on the aluminum surface.

After PA adsorption stage, the PA modified aluminum sheet is rinsed by H_2O in air. This transition towards air exposure has a crucial impact on the final stage of PA surface modification. It is the first time in this work to discuss systematically the PA molecular structural effect and aluminum re-oxidation effect on aluminum oxide surface modification in this transition stage to full air-exposure. Firstly, the physisorbed aluminum-phosphonate complexes that intimate contact on reactive hydroxylated aluminum surface convert to chemisorbed state after

H_2O rinsing synergistically with aluminum re-oxidation in air. This conversion is evidenced by mono-/bi-dentate covalent bindings of H_3PO_3 with aluminum oxide after 240 min treatment time. Meanwhile, this converted PA layer shows a low stratification with aluminum oxide layer, i.e. a rather mixture of low steric PA molecules and aluminum oxide. Due to the similar ionic interaction between low steric phosphonate anions with aluminum cations, the stratification factor of H_3PO_3, MPA and EPA are the same. However, note that the synergistic aluminum re-oxidation in air is limited with the increase of adsorbate PA steric effect. EPA is a benchmark molecule that starts to reduce significantly the re-oxidized aluminum layer thickness.

Moreover, the strong oxidation of air-exposure step in the transition stage might also affect the final stage of high steric PA layer. In addition to PePA, although high steric PA molecules chemisorb on the surface, the stratification of high steric PA layer with oxide layer decreases after 5 min (typically for BPA and CnPPA). This work raises the hypothesis that this phenomenon might also be due to the high steric PA layer captured aluminum-phosphonate complexes in the adsorption stage. The existing of aluminum-phosphonate complexes in high steric solution is inferred from the detected aluminum cations in solution and the gradual decrease of final aluminum oxide layer from 5 min to 120 min.

This strong oxidation during transition upon air-exposure is further studied in a glovebox at very low O_2 partial pressure. After 5 min treatment in glovebox, the average of oxygen extra-atomic electronic polarizability of CnPPA modified aluminum oxide is increased due to the mixture of hydroxide. The CnPPA modified unstable reactive aluminum surface are converted to hydroxide by the residual H_2O on surface after H_2O rinsing and 30 min vacuum drying. Whereas, a full air-exposure step or prior MtPPA surface passivation exhibits an aluminum oxide after surface treatment. Thus, the final PA modified aluminum oxide morphology depends on both, molecular structural effect in the adsorption stage as well as the exposure atmosphere effect in the transition stage.

The high steric effect of PePA with 2-phenylethyl group is a remarkable molecule because it shows the same modified aluminum oxide surface during the adsorption stage (from 5 min to 240 min) and also in the final stage. Firstly, during the adsorption stage of 240 min, PePA provides sufficient surface passivation and thus, protects the initial L_{OX} layer. Therefore, the air-exposure transition stage does not significantly change the thickness of adsorbent L_{OX}. Meanwhile, PePA is also uniquely capable of self-assemble, which increases the amount of adsorbed PA molecules and reaches surface saturation after 120 min due to the π-π interaction among 2-phenylethyl groups.

This work provides a systematical fundamental understanding of molecular steric and electron environment effects on phosphonic acid interaction with aluminum oxide surface. A few analytical tools are provided in this work, which helps feature study:

1. relative dissolution inhibition factor using H_3PO_3 as a benchmark,
2. frequency dependent resistor and capacitor of equivalent circuit used for EIS data analysis,
3. normalized stratification factor being a measure for adsorbed PA molecule on surface,
4. A XPS/HAXPES combined system consists of glovebox and vacuum transfer system providing oxygen and aluminum Auger parameter analysis without air-exposure contamination.

These fundamental understandings and analytical tools are instructive for the design of PA molecules tailored to specific application scenarios. Synthesis of a new PA molecule with an additional functional group on 2-phenylethyl phosphonic acid would be a good candidate for a fast SAMs formation on aluminum surface, which only requires 240 min at room temperature, protects the adsorbent oxide layer, and fits well into an oxygen limited environment as shown in Figure 6.1.

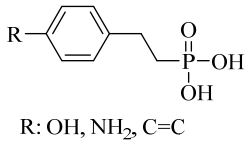

Figure 6.1. *Suggested design of a new phosphonic acid for the next generation of aluminum oxide surface functionalization.*

This kind of PA surface modification would be applied for a primer on the aluminum oxide surface to increase the adhesive joining adhesion and durability. Meanwhile, when the adsorbent extends from pure aluminum sheet to aluminum alloys, e.g. aluminum alloy 5XXX/ 6XXX series commonly used in the automobile industry, magnesium is the major alloy element that is stable in acidic solution. To use a PA molecule with similar structure to high steric PA studied (e.g. BPA, MtPPA) as a primer would increases the aluminum alloy surface lateral homogeneity for a short immersion time (within 5 min) since the aluminum oxide is protected.

Appendix A

1. PH measurement of the prepared PA solution

The pH measurement is done at room temperature by 914 pH/Conductometer by Metrohm AG.

Table A.1. *pH value of 0.01M phosphonic acid aquatic solution*

acid	H_3PO_3	MPA	EPA	tBPA	BPA	PePA	PPA	CnPPA	MtPPA
pH	2.2	2.4	2.4	2.5	2.3	2.4	2.3	2.2	2.4

2. Initial transition to steady state

Numerical simulations of the initial transition to steady state at interface according to the rate model proposed in the main manuscript is shown in Figure A.1. The aluminum sample is immersed into one of the phosphonic acid solutions and the native oxide layer is assumed to be dissolved quickly to form a mainly hydrolyzed aluminum surface, i.e. at t_0=0. The adsorbed states of phosphonic acid are initially unpopulated. Therefore, the aluminum leaching rate (from unprotected aluminum surface) is initially maximal, followed by an asymptotic decrease to a steady state value; a constant rate of aluminum dissolution is eventually reached (figures below, red curve). We have simulated three different scenarios to visualize the kinetics of competitive adsorption/desorption; i.e. involving physisorption with/without the possibility to ensue monodentate or bidentate chemisorption. The most stable chemisorbed states are predominantly populated at steady state, as they are available. In all scenarios, a constant aluminum leaching rate (i.e. constant slope of red curve) is eventually reached, predicting steady state conditions. This numerical simulation is supported by Prof. Dr. Manfred Heuberger.

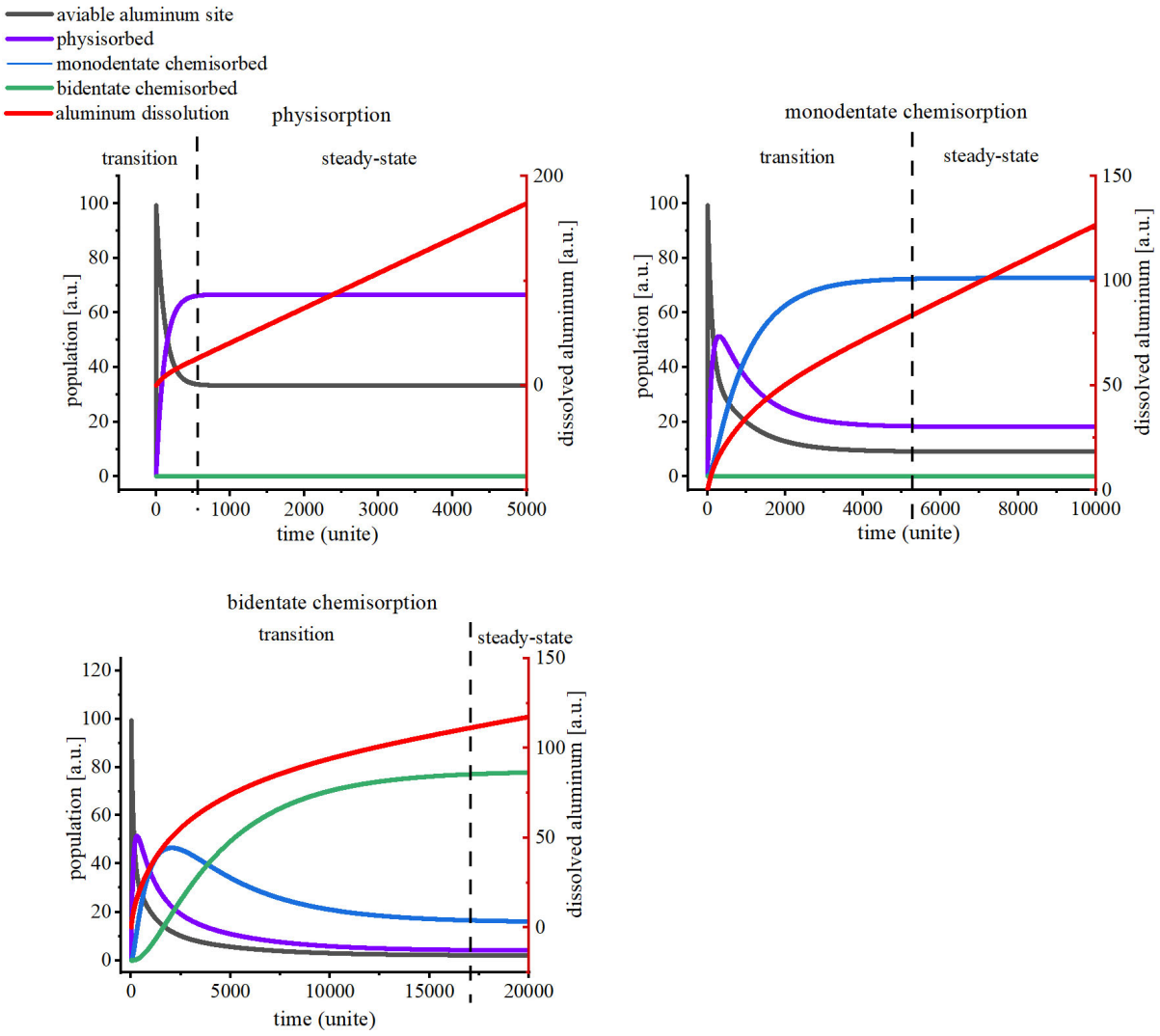

Figure A.1. *Numerical simulation of charges and species transfer at the interface of PA solution and aluminum surface, as predicted by the proposed rate model: from transition period to steady-state.*

3. Aluminum concentration measured by ICP-OES

The total amount of aluminum dissolved in the supernatant solution as a function of time was measured, as displayed in Figure 3.2. Each PA treatment condition was repeated for three times, the average value and standard deviation (STDEV) are shown in Table A.2.

Table A.2*. Aluminum concentration (ppm) evolution with time in different PA solutions*

a) low steric PA

time (min)	H_3PO_3		MPA		EPA	
	average	STDEV	average	STDEV	average	STDEV
5	0.40	0.04	0.23	0.02	0.10	0.01
15	1.19	0.12	0.48	0.02	0.21	0.01

60	3.60	0.99	2.24	0.07	0.96	0.07
120	8.22	0.57	4.43	0.29	2.57	0.3
240	15.74	1.06	8.39	0.19	4.53	0.18

b) high steric PA

time (min)	tBPA		BPA		PePA	
	average	STDEV	average	STDEV	average	STDEV
5	-	-	0.04	0.01	0.02	0.01
15	-	-	0.07	0.01	0.02	0.000
60	0.01	0.00	0.17	0.01	0.04	0.01
120	0.06	0.01	0.35	0.04	0.06	0.01
240	0.16	0.01	0.75	0.07	0.07	0.01

c) high steric PA with varied electron environment

time (min)	CnPPA		PPA		MtPPA	
	average	STDEV	average	STDEV	average	STDEV
5	0.05	0.01	0.05	0.005	0.04	0.01
15	0.14	0.01	0.12	0.012	0.06	0.01
60	0.59	0.01	0.36	0.016	0.12	0.01
120	1.22	0.12	0.80	0.082	0.19	0.03
240	2.57	0.18	1.85	0.082	0.29	0.02

4. Equivalent circuit fitting of EIS data

The equivalent circuit model used to fit and interpret the EIS measurements were modified to allow for low-frequency (LF) features especially for two of the equivalent circuit elements. In order to allow stable fitting, we chose functions that mainly change at low frequency, but exhibit asymptotic behavior at higher frequency. Namely, we choose the following mathematical representation:

$R_{(f)}\ or\ Cg_{(f)} = \sum_i \frac{C_i}{a(f)^i}$, with monotonous frequency scaling $a(f) = \log(f) + 4$,

in which frequency dependent geometric interface capacitance ($Cg_{(f)}$), frequency dependent interface- or charge transfer resistance ($R_{(f)}$)

With this mathematical description LF-features can be described by an array of coefficients C_i; the first coefficient, C_0, corresponds to a constant value (i.e. the conventional model), here also seen as high-frequency asymptotic value. Table B summarizes the numerical fitting results that are also used to generate the fitted curves (plain lines) shown in Figure 6 of the main paper. Note that the value of Z_{int} is a complex number described by two arrays of coefficients C_i.

Table A.3. *The coefficients C_i used in the frequency-dependent element calculation.*

H_3PO_3	AW	Re	Cg	Rct	CED	Z'int	Z"int
C0	1.20E+3	1.29E+3	2.80E-6	0	0	2.01E+4	-6.44E+3
C1	-	-	-1.97E-5	-	-	7.70E+3	5.19E+4
C2	-	-	7.96E-5	-	-	-3.54E+4	-6.95E+4
C3	-	-	2.33E-6	-	-	-6.89E+4	-2.04E+0
C4	-	-	-4.09E-6	-	-	1.56E+5	-7.77E-1

MPA	AW	Re	Cg	Rct	CED	Z'int	Z"int
C0	1.70E+3	2.23E+3	7.21E-7	0	0	9.15E+4	2.47E+3
C1	-	-	-1.09E-6	-	-	-2.37E+5	4.13E+4
C2	-	-	2.76E-5	-	-	1.75E+5	-7.19E+4
C3	-	-	-	-	-	8.40E+2	-3.37E+4
C4	-	-	-	-	-	1.75E+5	-7.19E+4

EPA	AW	Re	Cg	Rct	CED	Z'int	Z"int
C0	2.72E+3	2.66E+3	1.01E-6	0	0	3.11E+5	5.33E+4
C1	-	-	-1.46E-6	-	-	-6.14E+5	-2.22E+4
C2	-	-	1.45E-5	-	-	5.99E+4	-1.16E+5
C3	-	-	-1.62E-8	-	-	1.97E+5	-4.32E+3
C4	-	-	-2.01E-6	-	-	2.12E+5	1.34E+5

tBPA	AW	Re	Cg	Rct	CED	Z'int	Z"int
C0	1.67E+4	2.94E+3	1.72E-6	0	0	1.55E+6	-6.22E+5
C1	-	-	-2.65E-6	-	-	-1.11E+7	1.33E+6
C2	-	-	1.04E-6	-	-	2.83E+7	4.92E+5
C3	-	-	-	-	-	1.17E-8	-7.09E+5
C4	-	-	-	-	-	-3.10E+7	-1.52E+6

BPA	AW	Re	Cg	Rct	CED	Z'int	Z"int
C0	6.54E-13	1.96E+3	1.29E-6	7.10E+4	1.46E-6	3.85E+5	0
C1	-	-	-	7.67E+5	2.19E-5	2.88E+5	0
C2	-	-	-	3.65E+4	-	-	-
C3	-	-	-	-6.00E+5	-	-	-

PePA	AW	Re	Cg	Rct	CED	Z'int	Z''int
C0	1.25E+4	1.83E+3	1.59E-6	0	0	4.21E+5	0
C1	-	-	4.64E-7	-	-	1.02E-8	0
C2	-	-	-	-	-	7.54E-9	0
C3	-	-	-	-	-	1.26E+7	0
C4	-	-	-	-	-	-1.36E+7	0

CnPPA	AW	Re	Cg	Rct	CED	Z'int	Z''int
C0	1.50E+3	1.30E+3	2.12E-6	7.72E+5	1.35E-5	8.74E+5	0
C1	-	-	-2.75E-6	-1.00E+6	-1.76E-5	-1.16E+6	0

PPA	AW	Re	Cg	Rct	CED	Z'int	Z''int
C0	1.50E+3	1.67E+3	1.52E-6	9.90E+5	6.05E-6	9.40E+5	-1.08E+5
C1	-	-	-	-1.29E+6	-	-1.20E+6	1.25E+6
C2	-	-	-	-	-	-1.80E-8	-1.43E+6

CnPPA	AW	Re	Cg	Rct	CED	Z'int	Z''int
C0	1.50E+3	1.79E+3	1.00E-6	9.36E+04	-2.58E-06	1.23E+05	-1.08E+5
C1	-	-	1.53E-6	7.57E+05	2.09E-05	1.41E+06	1.25E+6
C2	-	-	-	4.26E+04	-1.31E-06	4.03E-02	-1.43E+6
C4	-	-	-	-2.24E+05	2.01E-04	-1.39E+05	
C5	-	-	-	-1.10E+06	-		

Note: Error values are unfortunately not quantifiable due to the semi-automated iterative fitting procedure, required to avoid parameter runaways. The iterative process was thus sometimes stopped with only a selection of parameters enabled. Since we show measured and model-calculated values together in all plots, a visual rather than quantitative inspection of fitting error is still readily available.

5. Bode plots of EIS data

Figure A.2 shows the same data as in Figure 3.3 but this time displayed in the Bode-plot representation, where the results are divided into three groups a), b) and c) based on the molecule classification mentioned in Chapter 1, Figure 1.3). The blue diamond shape shows the aluminum surface impedance ($Z_{Al\_surface}$).

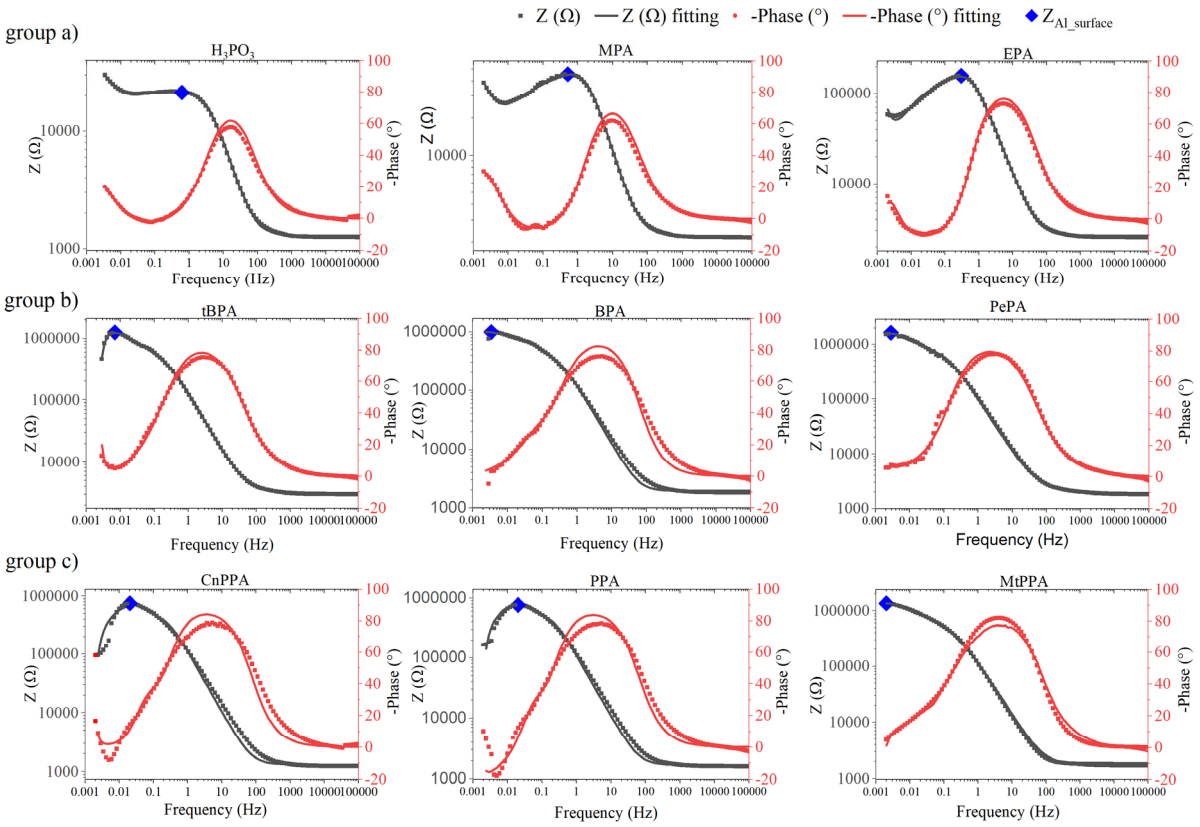

Figure A.2. *The EIS measurement results and their equivalent circuit fittings of aluminum in different PA solutions in the Bode plot representation.*

6. Insights from molecule calculations

Table A.4 lists some key theoretical values calculated for the nine different phosphonic acid molecules.

Table A.4. DFT calculated ionization potential (IP), vertical electron affinity (EA), and electronegativity (χ); HOMO/ LUMO energy and energy gap (ΔE).

	IP: E(N-1)-E(N)	EA: E(N)-E(N+1)	χ: (IP+EA)/2	E_{HOMO} (eV)	E_{LUMO} (eV)	ΔE (E_{LUMO}-E_{HOMO})
H_3PO_3	10.69	-1.80	4.44	-8.58	0.38	8.96
MPA	10.22	-0.94	4.64	-8.21	0.35	8.56
EPA	9.97	-0.90	4.53	-8.11	0.37	8.48
tBPA	9.43	-0.91	4.26	-7.92	0.40	8.32
BPA	8.77	-1.26	3.76	-6.84	-0.49	6.35
PePA	8.62	-1.37	3.62	-7.26	-0.86	6.40
CnPPA	9.34	0.77	5.05	-7.87	-2.40	5.48
PPA	9.05	-0.23	4.41	-7.39	-1.16	6.23
MtPPA	8.16	-0.62	3.77	-6.63	-0.87	5.76

Appendix B

1. Calculated Atomic Fraction of Phosphorus Atom in PA Molecule

Table B.1. *Atomic fraction of phosphorus atom in the respective PA molecular unit (excluding H, since it cannot be detected by XPS) for the different PA molecules, noted as* f_P .

	H_3PO_3	MPA	EPA	tBPA	BPA	PePA	CnPPA	PPA	MtPPA
f_P	1/4	1/5	1/6	1/8	1/11	1/12	1/12	1/10	1/12

2. Shakeup Binding Energy of C 1s Evolution with Different PA Molecules Treated Aluminum Oxide Surface.

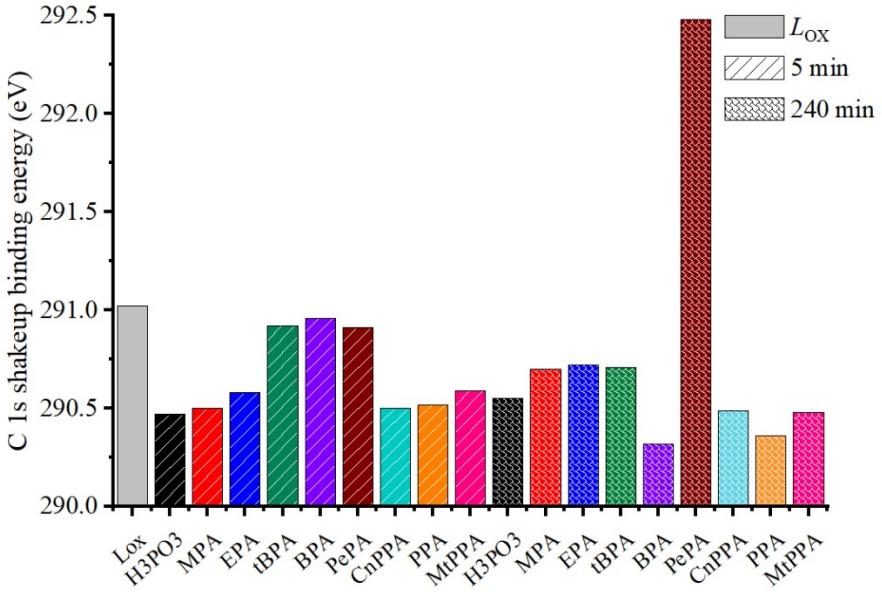

Figure B.1. *Resolved binding energy of the C 1s π→π* shakeup satellite peak for the different PA molecules (see Fig. 2) after an immersion time of 5 min and 240 min.* L_{OX} *is the NaOH etched aluminum oxide prior to PA surface treatment.*

3. Survey Scan of Aluminum Oxide Formed after NaOH Etching

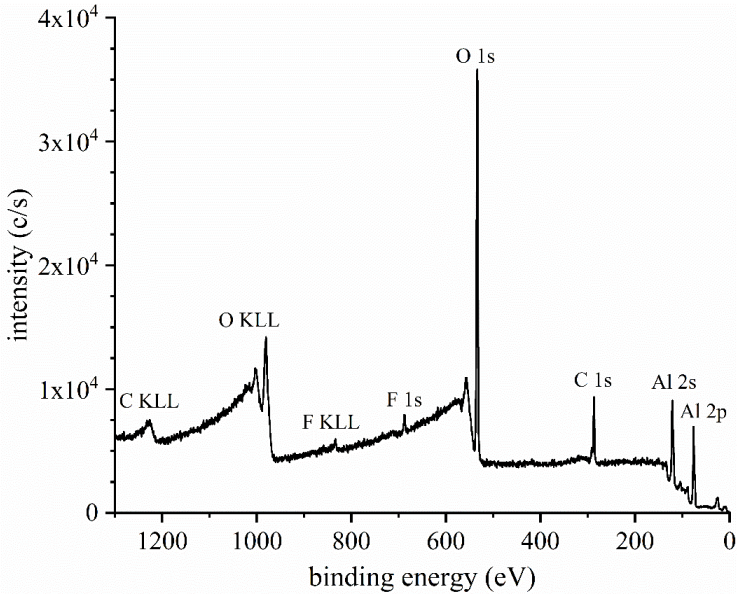

Figure B.2. *XPS survey scan of the aluminum surface after etching in NaOH, followed by rinsing in water and exposure to air (L_{OX}). Besides the signals from aluminum oxide and metallic aluminum, there are still significant amounts of adventitious carbon from air exposure. A slight fluorine contamination originates from the XPS analysis chamber.*

4. Valence Band of Aluminum Oxide Formed after NaOH Etching

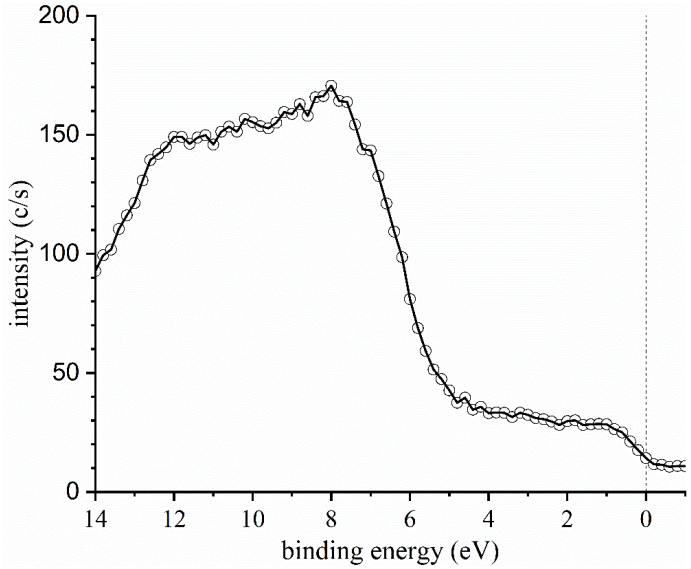

Figure B.3. *XPS measurement of the valence band region of the aluminum surface after etching in NaOH, followed by rinsing in deionized water and exposure to air. As evidenced by the featureless shape of the upper valence band, the oxide film is predominantly amorphous.*

5. Deconvolution of Photoelectron Peak, Al 2p, of NaOH Etching Formed Aluminum Oxide

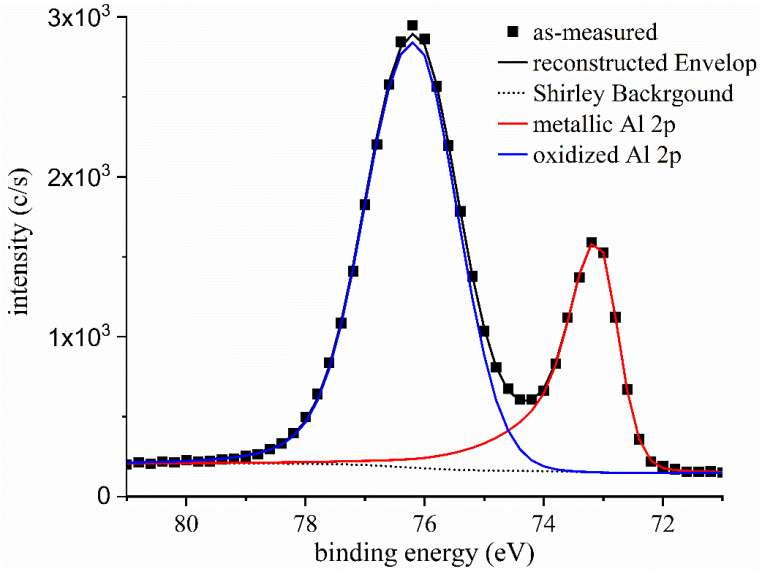

Figure B.4.*Peak fitting of the measured Al 2p spectrum of the aluminum surface after etching in NaOH, followed by rinsing in deionized water and exposure to air. The Al 2p spectrum shows contributions from metallic aluminum substrate and in the oxide overlayer. Note: the metallic Al 2p main peak was shifted to 73 eV to correct for differences in charging during the XPS measurement.*

6. Parameters for Aluminum Oxide Thickness Calculation

Here different parameters of amorphous aluminum oxide, α-Al_2O_3 (Sapphire), α-$Al(OH)_3$ (Bayerite) and metallic aluminum (Al) for aluminum oxide calculation are listed in Table B.2. Specifically, the IMFP values were calculated from the TTP2 formulism. E_g denotes the optical band gap (eV); BE is the binding energy of the respective Al 2p main peak; ρ is the density (g/cm^3); M is the atomic or molecular weight; N_v is the number of valence electrons per atom (for elemental solids) or for the molecular unit (for compounds).

Table B.2. *Calculated values of the inelastic mean free pass (IMFP) of Al 2p photoelectrons emitted by Al X-rays in the solid and traveling through metallic aluminum or different aluminum oxide/hydroxide phases.*

	E_g (eV)	BE (eV)	ρ (g/cm^3)	M (g/mol)	Nv	IMFP (nm)
amorphous Al_2O_3	3.6	74.68	3.2	101.96	24	3.06
α-Al_2O_3	9	74.68	3.97	101.96	24	3.28
α-$Al(OH)_3$	5.54	74.68	2.455	78	21	3.44
metallic Al	0	72.8	2.669	26.9815	3	3.12

7. **The Average of Aluminum Oxide Thickness Calculated by Assuming Different Oxide/Hydroxide Structure as Documented in Table B.2.**

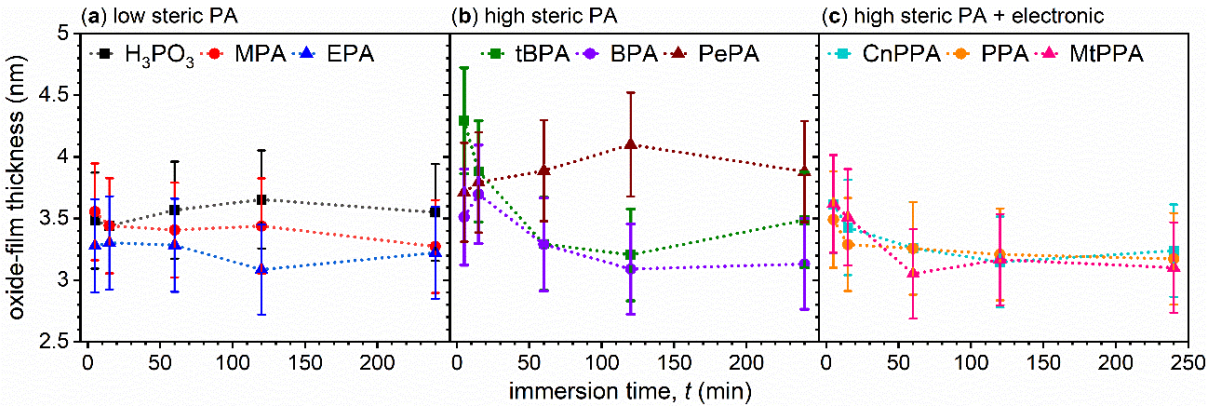

Figure B.5. *Average value and standard deviation of the PA modified oxide film thickness as a function of immersion time. The error bars were calculated from the thickness values obtained from three identical, repetitive surface treatments, while assuming different values for the density and IMFPs of different oxide/hydroxide phase, as tabulated in Table B.2.*

8. **Valence Band of Aluminum Oxide Formed after Different Chemical Treatment.**

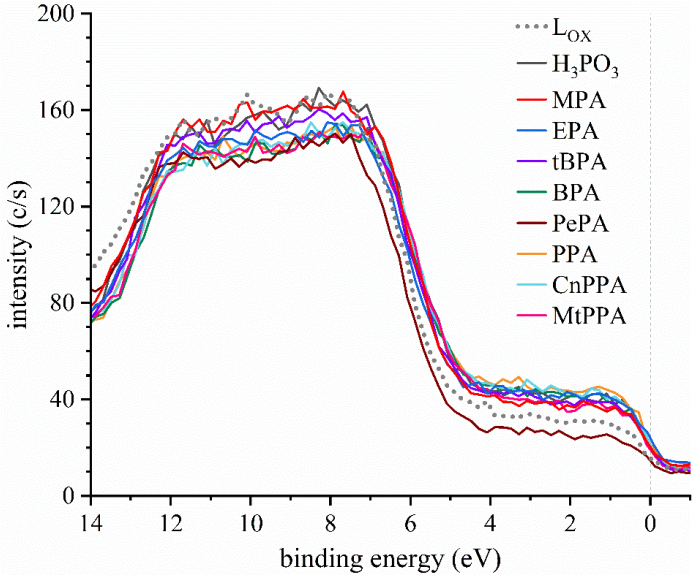

Figure B.6. *XPS measurements of the valence band region of all chemically treated surfaces, evidencing a featureless shape of the upper valence band similar to that of the NaOH etched aluminum surface (denoted as LOX). It may thus be concluded that an amorphous state of the oxide film is largely preserved after chemical treatment, followed by H_2O rinsing and air exposure.*

9. Binding Energy Shifts of Oxidized Al 2p and P 2s Photoelectron Peaks as Function of Time after Different PA Treatment.

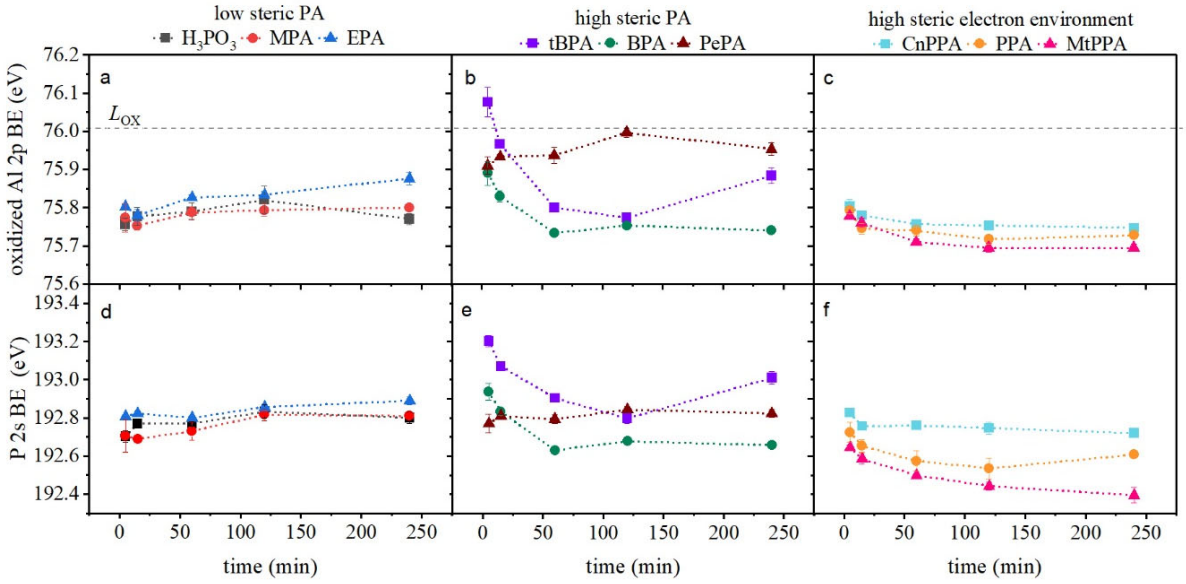

Figure B.7. *Resolved binding energies (BE) of* ***(a,b,c)*** *the oxidic Al 2p, and* ***(d,e,f)*** *the P 2s main peaks as a function of immersion time for the PA molecules of class (a) – (b).*

10. ToF-SIMS Spectrums of PA-Aluminum Fragments on Various Aluminum Oxides Modified by Chosen PA Molecules.

For each group of PA molecules, one PA molecule is chosen to study its phosphonic acid group interaction mode with aluminum oxide. The normalized intensity is used to present different fragment intensity, which is calculated by measured peak intensity divided by total mass counts.

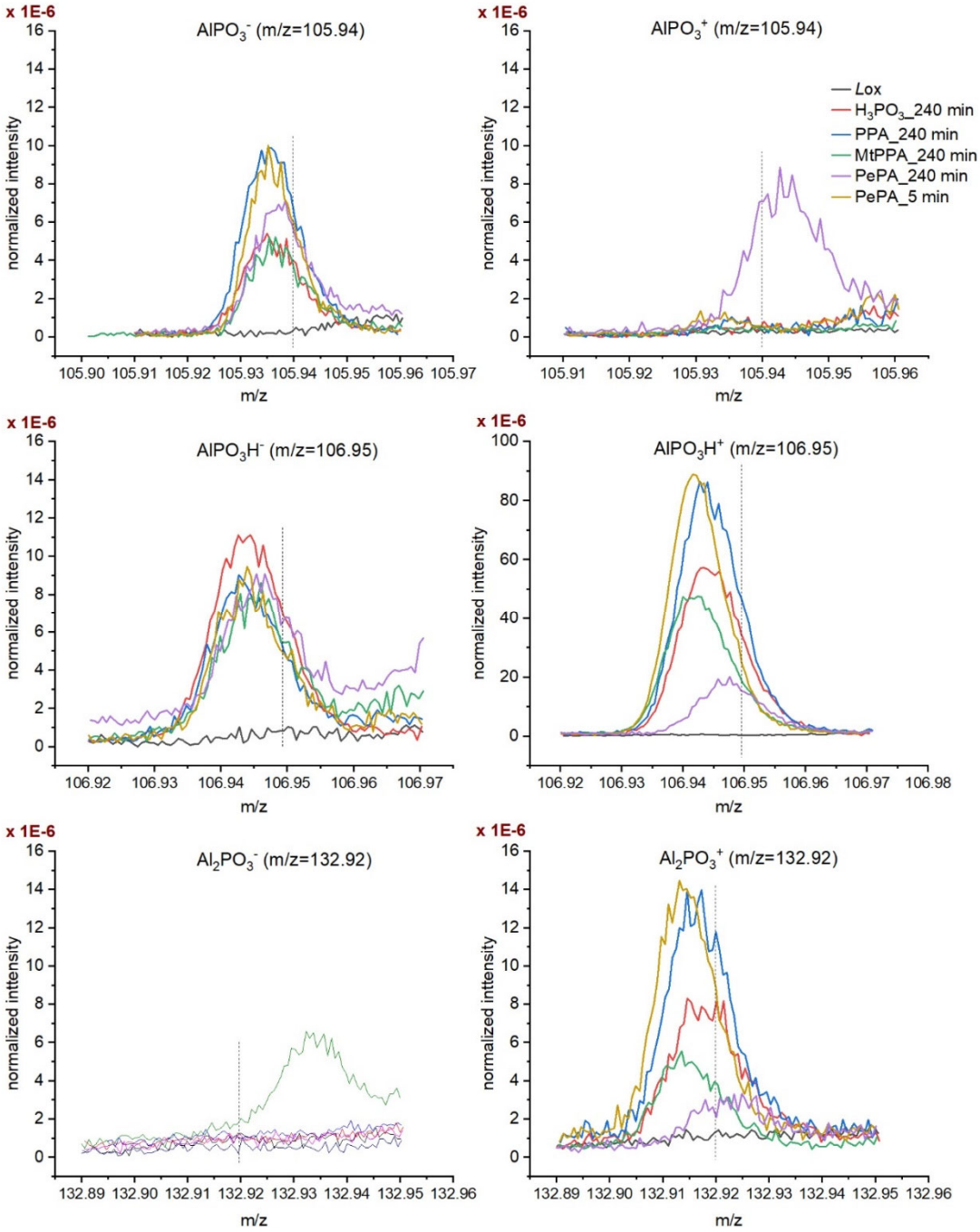

Figure B.8. *ToF-SIMS surface characterization of aluminum oxide formed by NaOH etching (Lox) and aluminum oxide formed after different PA treatment: H_3PO_3_240 min, PPA_240 min, MtPPA_240 min, PePA_240 min and PePA_5 min.*

Appendix C

1. X-ray/ Hard X-ray Photoelectron Spectroscopy (XPS/HAXPES) Surface Characterization.

MtPPA modified aluminum oxide surface in glovebox is denoted as "Al-O+MtPPA GB". The survey and detail scans of "Al-O+MtPPA GB" is used as an example to display by X-ray/ hard X-ray photoelectron spectroscopy (XPA/ HAXPES) surface characterization, as shown in Figure C.1. HAXPS provides more information on deep core-level photoelectron lines and its Auger transition, such as Al 1s and Al KLL, as shown in Figure C.1 red line. Moreover, HAXPES is more in depth sensitive with the probing depth of photoelectrons up to ~20 nm[113]. XPS surface characterization is more surface sensitive than HAXPES. For example, in this current study, XPS measured Al 2p detail scan shows a clear two peaks that contribute from the top oxide film and underneath metallic aluminum substrate, as shown in Figure C.1 blue line. However, HAXPES measured Al 2p detail scan exhibits a weak oxidized Al 2p peak. Thus, it is necessary to combine XPS and HAXPES to provide a full information on PA modified aluminum oxide.

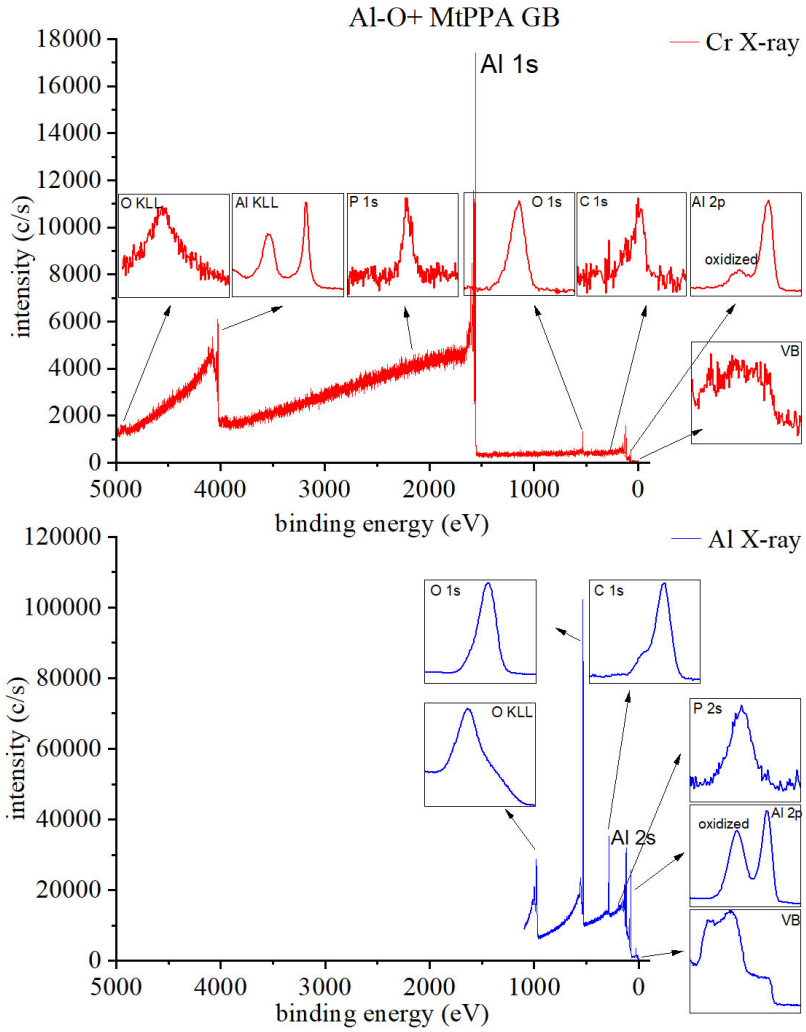

Figure C.1. *HAXPES and XPS measured MtPPA modified aluminum oxide in glovebox (Al-O+MtPPA GB). The red line shows the HAXPES survey scan spectrum with enlarged captions for details scan of photoelectron peaks, Augers peaks and valence band (VB). The blue line displays the XPS surface survey scan and enlarged captions for detail scan spectrums.*

2. XRD Characterization of Crystalline Aluminum Oxide/Hydroxide

The crystalline structure of commercial single crystalline Sapphire (α-Al_2O_3), lab synthesized Bayerite (α-$Al(OH)_3$) is characterized by XRD. The lab synthesized aluminum hydroxides show metallic aluminum substrate since the aluminum hydroxide layer is around 10~15 μm.

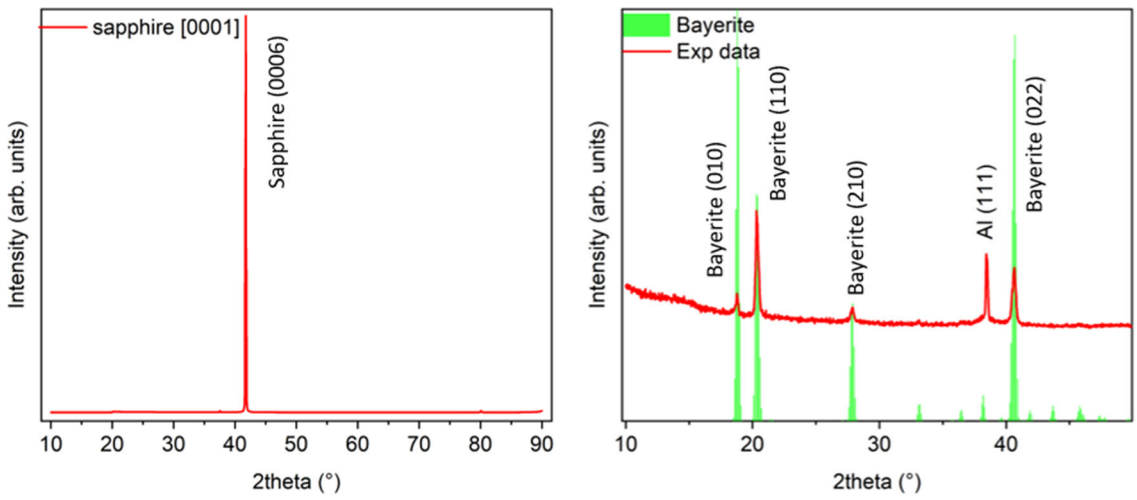

Figure C.2. *XRD characterization of commercial single crystalline Sapphire and lab synthesized multi-crystalline Bayerite.*

3. Oxygen and Aluminum Auger Peak of Reference Aluminum Oxides/Hydroxide

The intensities of O KLL peaks of crystalline and amorphous aluminum oxides/hydroxide are normalized from 0-1 to highlight the "shoulder" shape changes on the low binding energy side as shown in dash arrow in Figure C.3a. The Al KLL peaks of crystalline and amorphous aluminum oxides/hydroxide are displayed in Figure C.3b. It is notable that "metallic Al" exhibits a minor peak at binding energy of 4027 eV, which is aluminum plasmon but not oxidized phase.

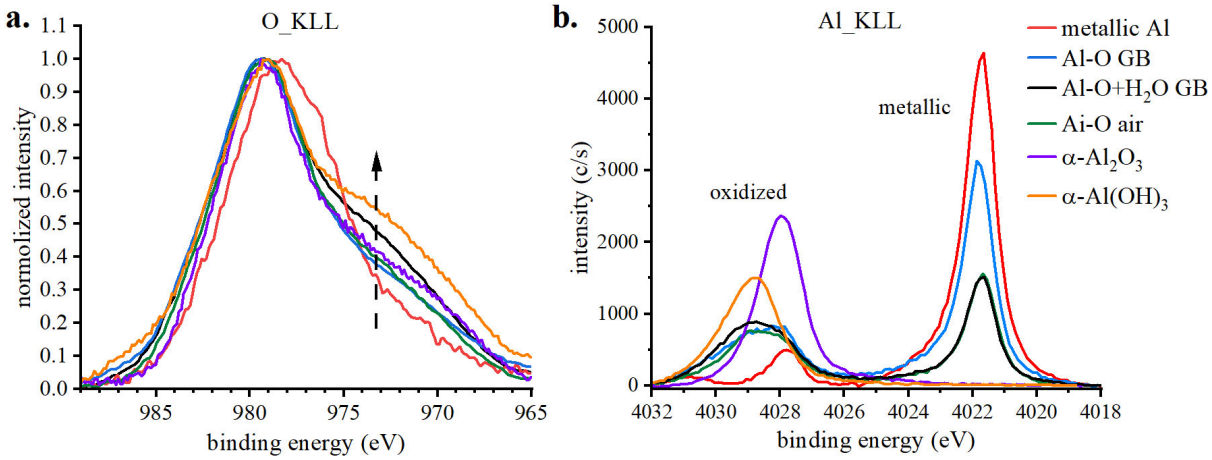

Figure C.3. *a).XPS measured oxygen Auger peak, and b). HAXPES measured aluminum Auger peak of crystalline aluminum oxide/hydroxides and amorphous aluminum oxides without phosphonic acid treatment.*

4. Oxygen and Aluminum Auger Peak of Phosphonic Acid Modified Aluminum Oxide

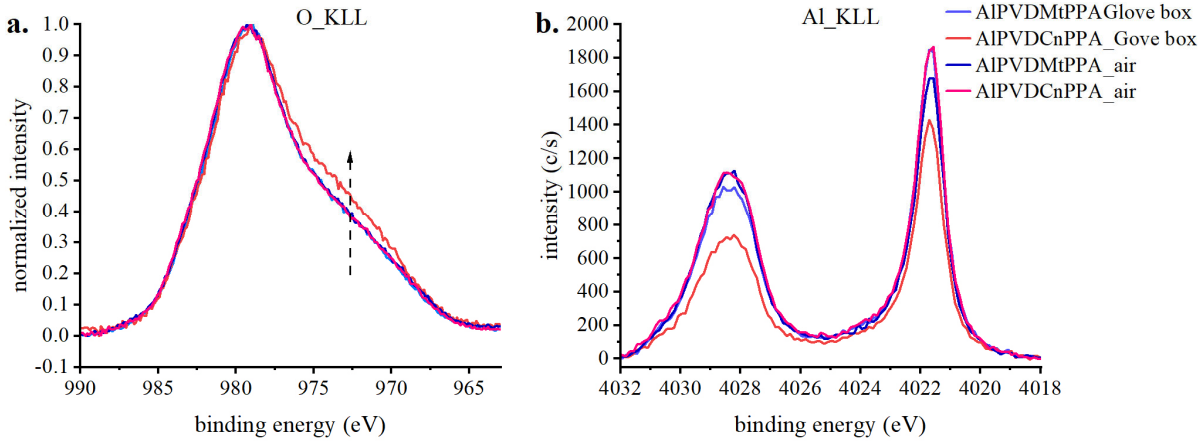

Figure C.4. *XPS measured oxygen Auger peak (a.) and HAXPES measured aluminum Auger peak of phosphonic acid modified aluminum oxides (b)*

5. Oxygen and Aluminum (Oxidized and Metallic) Auger parameter

Table C1. *Summary of oxygen and aluminum Auger parameter*

oxygen Auger parameter						
	BE_O 1s		KE_O KLL		AP_O	
	average	STDEV	average	STDEV	average	STDEV
Sapphire	530.80	-	508.66	-	1039.46	-
Bayerite	531.67	-	508.70	-	1040.37	-
Metallic Al	-	-	-	-	-	-
Al-O GB	532.63	0.06	507.11	0.18	1039.74	0.16
Al-O air	532.67	-	507.04	-	1039.71	-
Al-O+H2O GB	533.21	0.10	507.06	0.13	1040.26	0.02
Al-O+MtPPA GB	532.72	0.04	507.17	0.03	1039.89	0.07
Al-O+MtPPA air	532.69	0.06	507.16	0.10	1039.85	0.10
Al-O+CnPPA GB	532.86	0.09	507.22	0.02	1040.08	0.08
Al-O+CnPPA air	532.74	0.04	507.16	0.05	1039.90	0.01

oxidized aluminum Auger parameter						
	BE_Al 2p_oxidized		KE_Al KLL_oxidized		AP_Al_oxidized	
	average	STDEV	average	STDEV	average	STDEV
Sapphire	73.71	-	1388.03	-	1461.74	-
Bayerite	74.04	-	1386.98	-	1461.02	-
Metallic Al	-	-	-	-	-	-
Al-O GB	75.89	0.05	1386.33	0.08	1462.21	0.09
Al-O air	75.91	-	1385.87	-	1461.78	-

Al-O+H2O GB	75.97	0.02	1385.74	0.10	1461.71	0.08
Al-O+MtPPA GB	75.86	0.01	1386.00	0.20	1461.85	0.19
Al-O+MtPPA air	75.85	0.02	1386.10	0.15	1461.95	0.13
Al-O+CnPPA GB	75.85	0.00	1386.10	0.14	1461.95	0.13
Al-O+CnPPA air	75.85	0.00	1385.97	0.12	1461.82	0.12

metallic aluminum Auger parameter						
	BE_Al 2p_metallic		KE_Al KLL_metallic		AP_Al_metallic	
	average	STDEV	average	STDEV	average	STDEV
Sapphire	-	-	-	-	-	-
Bayerite	-	-	-	-	-	-
Metallic Al	73.0	-	1392.95	-	1465.95	-
Al-O GB	73.0	0.00	1392.94	0.03	1465.94	0.00
Al-O air	73.0	-	1393.00	-	1466.01	-
Al-O+H2O GB	73.0	0.00	1393.00	0.00	1466.00	0.00
Al-O+MtPPA GB	73.0	0.00	1392.55	0.09	1465.56	0.18
Al-O+MtPPA air	73.0	0.00	1392.75	0.02	1465.76	0.00
Al-O+CnPPA GB	73.0	0.00	1392.79	0.02	1465.79	0.00
Al-O+CnPPA air	73.0	0.00	1392.62	0.07	1465.63	0.13

This page intentionally left blank

Reference

1. Fridlyander, I.N., et al., *Aluminum Alloys: Promising Materials in the Automotive Industry.* Metal Science and Heat Treatment, 2002. **44**(9): p. 365-370.
2. Starke, E.A. and J.T. Staley, *Application of modern aluminum alloys to aircraft.* Progress in Aerospace Sciences, 1996. **32**(2): p. 131-172.
3. Twite, R.L. and G.P. Bierwagen, *Review of alternatives to chromate for corrosion protection of aluminum aerospace alloys.* Progress in Organic Coatings, 1998. **33**(2): p. 91-100.
4. Kaufman, J.G., *Introduction to Aluminum Alloys and Tempers*. 2000: ASM international.
5. Feister, T., et al., *Failure predictions in warm forming of 7075-T6 aluminum structural parts.* IOP Conference Series: Materials Science and Engineering, 2018. **418**: p. 012024.
6. Weritz, J. and M. Dudek. *Aluminum Roadmap to a Sustainable Future*. 2022. Cham: Springer International Publishing.
7. Pröller, S. *Dual-curing adhesives for fast cycle times and high-precision alignment of components*. in *Vehicles of Tomorrow 2019*. 2021. Wiesbaden: Springer Fachmedien Wiesbaden.
8. Hung, Y.Y., et al., *Review and comparison of shearography and pulsed thermography for adhesive bond evaluation.* Optical Engineering, 2007. **46**(5): p. 051007.
9. Shannon, R.W. and E.W. Thrall, *Adhesive bonding of aluminum alloys*. First edition. ed. Materials Engineering ; 1. 2017, Place of publication not identified: Routledge.
10. Pate, K.D., *Chapter 25 - Applications of adhesives in aerospace*, in *Adhesion Science and Engineering*, D.A. Dillard, A.V. Pocius, and M. Chaudhury, Editors. 2002, Elsevier Science B.V.: Amsterdam. p. 1129-1192.
11. Critchlow, G.W. and D.M. Brewis, *Review of surface pretreatments for aluminium alloys.* International Journal of Adhesion and Adhesives, 1996. **16**(4): p. 255-275.
12. Kendig, M., et al., *Role of hexavalent chromium in the inhibition of corrosion of aluminum alloys.* Surface and Coatings Technology, 2001. **140**(1): p. 58-66.
13. Lunder, O., et al., *Formation and characterisation of a chromate conversion coating on AA6060 aluminium.* Corrosion Science, 2005. **47**(7): p. 1604-1624.
14. Bhatt, H., *Alternatives to Hexavalent Chromium to Comply with European Union's Directives (ELV, RoHS and WEEE).* Plating and surface finishing, 2006. **93**(10): p. 20-23.
15. Abrahami, S.T., et al., *Towards Cr(VI)-free anodization of aluminum alloys for aerospace adhesive bonding applications: A review.* Frontiers of Chemical Science and Engineering, 2017. **11**(3): p. 465-482.
16. Yu, Q.S. and H.K. Yasuda, *Protection of aluminum alloys from filiform corrosion by low-temperature plasma interface engineering.* Progress in Organic Coatings, 2005. **52**(3): p. 217-226.
17. Quazi, M.M., et al., *Laser-based Surface Modifications of Aluminum and its Alloys.* Critical Reviews in Solid State and Materials Sciences, 2016. **41**(2): p. 106-131.
18. Park, S.Y., W.J. Choi, and H.S. Choi, *A review of the recent developments in surface treatment techniques for bonded repair of aluminum airframe structures.* International Journal of Adhesion and Adhesives, 2018. **80**: p. 16-29.

19. Phung, L.H., et al., *Influence of Self-Assembling Adhesion Promoter on the Properties of the Epoxy/Aluminium Interphase.* International Journal of Adhesion and Adhesives, 2005. **25**(3): p. 239-245.
20. Ahearn, J.S. and G.D. Davis, *Improved Durability of Aluminum Adhesive Bonds with Phosphonic Acid Inhibitors.* The Journal of Adhesion, 1989. **28**(2-3): p. 75-102.
21. Wapner, K., M. Stratmann, and G. Grundmeier, *Structure and stability of adhesion promoting aminopropyl phosphonate layers at polymer/aluminium oxide interfaces.* International Journal of Adhesion and Adhesives, 2008. **28**(1): p. 59-70.
22. Maege, I., et al., *Self-assembling adhesion promoters for corrosion resistant metal polymer interfaces.* Progress in Organic Coatings, 1998. **34**(1): p. 1-12.
23. Zhong, J. and J.B. Adams, *Adsorption and Decomposition Pathways of Vinyl Phosphonic and Ethanoic Acids on the Al (111) Surface: a Density Functional Analysis.* The Journal of Physical Chemistry C, 2007. **111**(20): p. 7366-7375.
24. Liao, K.-C., et al., *Comparative Interface Metrics for Metal-Free Monolayer-Based Dye-Sensitized Solar Cells.* ACS Applied Materials & Interfaces, 2012. **4**(12): p. 6735-6746.
25. Bauer, T., et al., *Phosphonate- and Carboxylate-Based Self-Assembled Monolayers for Organic Devices: A Theoretical Study of Surface Binding on Aluminum Oxide with Experimental Support.* ACS Applied Materials & Interfaces, 2013. **5**(13): p. 6073-6080.
26. Milošev, I., et al., *Editors' Choice—the Effect of Anchor Group and Alkyl Backbone Chain on Performance of Organic Compounds as Corrosion Inhibitors for Aluminum Investigated Using an Integrative Experimental-Modeling Approach.* Journal of The Electrochemical Society, 2020. **167**(6): p. 061509.
27. Marcinko, S. and A.Y. Fadeev, *Hydrolytic Stability of Organic Monolayers Supported on TiO2 and ZrO2.* Langmuir, 2004. **20**(6): p. 2270-2273.
28. Liakos, I.L., et al., *Comparative Study of Self‐Assembly of a Range of Monofunctional Aliphatic Molecules on Magnetron‐Sputtered Aluminium.* Surface and Interface Analysis: an International Journal Devoted to the Development and Application of Techniques for the Analysis of Surfaces, Interfaces and Thin Films, 2004. **36**(4): p. 347-354.
29. Gawalt, E.S., et al., *Bonding Organics to Ti Alloys: Facilitating Human Osteoblast Attachment and Spreading on Surgical Implant Materials.* Langmuir, 2003. **19**(1): p. 200-204.
30. Bassi, C., et al., *Metal Surface Coatings for Improving Bond Performance and Making the Surface Coatings and Coated Metal of Joined Structures*. 2021, Novelis Inc., USA; EMPA, Swiss Federal Laboratories for Materials Science and Technology . p. 35pp.
31. Cattani-Scholz, A., *Functional Organophosphonate Interfaces for Nanotechnology: A Review.* ACS Applied Materials & Interfaces, 2017. **9**(31): p. 25643-25655.
32. Zhao, R., et al., *Two Steady-State Adsorption Modes of Phosphonic Acids on Aluminum Surfaces.* ACS Applied Materials & Interfaces, 2022.
33. Zhao, R., P. Rupper, and S. Gaan, *Recent Development in Phosphonic Acid-Based Organic Coatings on Aluminum.* Coatings, 2017. **7**(9): p. 133.
34. Saker, S., et al., *Tetraphosphonic Acid as Eco-Friendly Corrosion Inhibitor on Carbon Steel in 3% NaCl Aqueous Solution.* Ionics, 2015. **21**(7): p. 2079-2090.

35. Labjar, N., et al., *Corrosion Inhibition of Carbon Steel and Antibacterial Properties of Aminotris-(Methylenephosphonic) Acid.* Materials Chemistry and Physics, 2010. **119**(1): p. 330-336.
36. Poshtiban, F., G. Bahlakeh, and B. Ramezanzadeh, *A Detailed Computational Exploration and Experimental Surface/Electrochemical Analyses of Mild Steel Functionalized by Zinc-Aminotris Methylene Phosphonic Acid Complex Film.* Applied Surface Science, 2019. **495**: p. 143582.
37. Yan, R., et al., *Corrosion Protective Performance of Amino Trimethylene Phosphonic Acid-Metal Complex Layers Fabricated on the Cold-Rolled Steel Substrate via One-Step Assembly.* Applied Surface Science, 2018. **442**: p. 264-274.
38. Duprat, M., F. Moran, and F. Dabosi, *Some preliminary experiments regarding the corrosion inhibition of a carbon steel by oleylamino-propylene amine with tri (methyl-phosphonic) acid.* Corrosion Science, 1983. **23**(9): p. 1047-1050.
39. Veres, A., G. Reinhard, and E. Kálmán, *Study of the chemical passivation of iron by phosphonates.* Materials and Corrosion, 1992. **43**(1): p. 28-32.
40. Fang, J.L., et al., *Passive Films and Corrosion Protection Due to Phosphonic Acid Inhibitors.* Corrosion, 1993. **49**(4): p. 266-271.
41. To, X., et al., *A Corrosion-Protective Film Formed on a Carbon Steel by an Organic Phosphonate.* Corrosion Science, 1997. **39**(10-11): p. 1925-1934.
42. laamari, M.R., et al., *Investigation of the Effect of Piperidin-1-Yl-Phosphonic Acid on Corrosion of Iron in Sulfuric Acid.* Arabian Journal of Chemistry, 2016. **9**: p. S1218-S1224.
43. Amar, H., et al., *Piperidin-1-Yl-Phosphonic Acid and (4-Phosphono-Piperazin-1-Yl) Phosphonic Acid: a New Class of Iron Corrosion Inhibitors in Sodium Chloride 3% Media.* Applied Surface Science, 2006. **252**(18): p. 6162-6172.
44. Falewicz, P. and S. Kuczkowska, *Untersuchung vielkomponentiger, Nitrilotrimethylenphosphonsäure enthaltender Systeme als Inhibitoren für den Metallschutz in neutralen wäßrigen Medien.* Materials and Corrosion, 1992. **43**(5): p. 215-223.
45. Kozlica, D.K., A. Kokalj, and I. Milošev, *Synergistic Effect of 2-Mercaptobenzimidazole and Octylphosphonic Acid as Corrosion Inhibitors for Copper and Aluminium – an Electrochemical, XPS, FTIR and DFT Study.* Corrosion Science, 2021. **182**: p. 109082.
46. Holzle, L., et al., *Corrosion behaviour of aluminium in ethyleneglycol–water electrolytes containing phosphonic acid.* Materials chemistry and physics, 2007. **103**(1): p. 59-64.
47. Xia, D.-H., et al., *Covalent surface modification of LY12 aluminum alloy surface by self-assembly dodecyl phosphate film towards corrosion protection.* Progress in Organic Coatings, 2020. **143**: p. 105638.
48. Pan, C., et al., *Monododecyl Phosphate Film on LY12 Aluminum Alloy: pH-Controlled Self-Assembly and Corrosion Resistance.* Journal of The Electrochemical Society, 2020. **167**(16): p. 161510.
49. Telegdi, J., et al., *Inhibition of aluminum alloy corrosion in electrolytes by self-assembled fluorophosphonic acid molecular layer.* Materials and Corrosion, 2016. **67**(10): p. 1027-1033.

50. Thieme, M. and H. Worch, *Ultrahydrophobic aluminium surfaces: properties and EIS measurements of different oxidic and thin-film coated states.* Journal of Solid State Electrochemistry, 2006. **10**(9): p. 737-745.
51. Fiurasek, P. and L. Reven, *Phosphonic and Sulfonic Acid-Functionalized Gold Nanoparticles: A Solid-State NMR Study.* Langmuir, 2007. **23**(5): p. 2857-2866.
52. Textor, M., et al., *Structural Chemistry of Self-Assembled Monolayers of Octadecylphosphoric Acid on Tantalum Oxide Surfaces.* Langmuir, 2000. **16**(7): p. 3257-3271.
53. Brovelli, D., et al., *Highly Oriented, Self-Assembled Alkanephosphate Monolayers on Tantalum(V) Oxide Surfaces.* Langmuir, 1999. **15**(13): p. 4324-4327.
54. Gao, W., et al., *Order−Disorder Transitions in Self-Assembled Monolayers: A 13C Solid-State NMR Study.* Langmuir, 1997. **13**(2): p. 115-118.
55. Pawsey, S., et al., *1H Fast MAS NMR Studies of Hydrogen-Bonding Interactions in Self-Assembled Monolayers.* Journal of the American Chemical Society, 2003. **125**(14): p. 4174-4184.
56. Pujari, S.P., et al., *Covalent surface modification of oxide surfaces.* Angewandte Chemie International Edition, 2014. **53**(25): p. 6322-6356.
57. Hoque, E., et al., *Alkylperfluorosilane Self-Assembled Monolayers on Aluminum: A Comparison with Alkylphosphonate Self-Assembled Monolayers.* The Journal of Physical Chemistry C, 2007. **111**(10): p. 3956-3962.
58. Hauffman, T., et al., *In Situ Study of the Deposition of (Ultra)thin Organic Phosphonic Acid Layers on the Oxide of Aluminum.* Langmuir, 2012. **28**(6): p. 3167-3173.
59. Hauffman, T., et al., *Dynamic, In Situ Study of Self-Assembling Organic Phosphonic Acid Monolayers from Ethanolic Solutions on Aluminium Oxides by Means of Odd Random Phase Multisine Electrochemical Impedance Spectroscopy.* Electrochimica Acta, 2013. **106**: p. 342-350.
60. Giza, M., P. Thissen, and G. Grundmeier, *Adsorption Kinetics of Organophosphonic Acids on Plasma-Modified Oxide-Covered Aluminum Surfaces.* Langmuir, 2008. **24**(16): p. 8688-8694.
61. Pellerite, M.J., et al., *Effects of Fluorination on Self-Assembled Monolayer Formation from Alkanephosphonic Acids on Aluminum: Kinetics and Structure.* The Journal of Physical Chemistry B, 2003. **107**(42): p. 11726-11736.
62. Hoque, E., et al., *Phosphonate self-assembled monolayers on aluminum surfaces.* The Journal of Chemical Physics, 2006. **124**(17): p. 174710.
63. Van Cleve, T., et al., *Enhanced Hydrothermal Stability of γ-Al2O3 Catalyst Supports with Alkyl Phosphonate Coatings.* Langmuir, 2018. **34**(12): p. 3619-3625.
64. Smith, J.G., *Organic chemistry*. 2008: McGraw-Hill.
65. Pijpers, A.P. and L. Lefferts, *The oxidation state of Ge on Pd/C catalysts investigated by XPS.* Applied Catalysis A: General, 1999. **185**(1): p. 29-39.
66. Friedrichs, O., et al., *Synthesis of nanocrystalline MgH2 powder by gas-phase condensation and in situ hydridation: TEM, XPS and XRD study.* Journal of Alloys and Compounds, 2007. **434-435**: p. 721-724.
67. Luo, W., et al., *Surface chemistry of black phosphorus under a controlled oxidative environment.* Nanotechnology, 2016. **27**(43).

68. Światowska-Mrowiecka, J., et al., *Adsorption of 1,2-diaminoethane on ZnO thin films from p-xylene.* Applied Surface Science, 2008. **254**(17): p. 5530-5539.
69. Światowska-Mrowiecka, J., et al., *XPS study of Li ion intercalation in V2O5 thin films prepared by thermal oxidation of vanadium metal.* Electrochimica Acta, 2007. **52**(18): p. 5644-5653.
70. Adolphi, B., et al., *Characterization of the adsorption of ω-(thiophene-3-yl alkyl) phosphonic acid on metal oxides with AR-XPS.* Analytical and Bioanalytical Chemistry, 2004. **379**(4): p. 646-652.
71. Hauffman, T., A. Hubin, and H. Terryn, *Study of the self-assembling of n-octylphosphonic acid layers on aluminum oxide from ethanolic solutions.* Surface and Interface Analysis, 2013. **45**(10): p. 1435-1440.
72. Mansfeld, F., *Use of Electrochemical Impedance Spectroscopy for the Study of Corrosion Protection by Polymer Coatings.* Journal of Applied Electrochemistry, 1995. **25**(3): p. 187-202.
73. Arabzadeh, H., M. Shahidi, and M.M. Foroughi, *Electrodeposited Polypyrrole Coatings on Mild Steel: Modeling the EIS Data with a New Equivalent Circuit and the Influence of Scan Rate and Cycle Number on the Corrosion Protection.* Journal of Electroanalytical Chemistry, 2017. **807**: p. 162-173.
74. Fernández-Sánchez, C., C.J. McNeil, and K. Rawson, *Electrochemical Impedance Spectroscopy Studies of Polymer Degradation: Application to Biosensor Development.* TrAC Trends in Analytical Chemistry, 2005. **24**(1): p. 37-48.
75. de Rooij, D.M.R., *Electrochemical Methods: Fundamentals and Applications.* Anti-Corrosion Methods and Materials, 2003. **50**(5).
76. BIOVIA, D.S., *Material Studio, v. 08.* San Diego: Dassault Systemes, 2018.
77. Inada, Y. and H. Orita, *Efficiency of Numerical Basis Sets for Predicting the Binding Energies of Hydrogen Bonded Complexes: Evidence of Small Basis Set Superposition Error Compared to Gaussian Basis Sets.* Journal of computational chemistry, 2008. **29**(2): p. 225-232.
78. Chakraborty, A., et al., *Aromaticity in All-Metal Annular Systems: the Counter-Ion Effect.* Physical Chemistry Chemical Physics, 2011. **13**(33): p. 14865-14878.
79. Visa, A., et al., *Combined Experimental and Theoretical Insights into the Corrosion Inhibition Activity on Carbon Steel Iron of Phosphonic Acids.* Molecules, 2021. **26**(1): p. 135.
80. Seah, M., *Summary of ISO/TC 201 Standard: VII ISO 15472: 2001—surface chemical analysis—x‐ray photoelectron spectrometers—calibration of energy scales.* Surface and Interface Analysis: An International Journal devoted to the development and application of techniques for the analysis of surfaces, interfaces and thin films, 2001. **31**(8): p. 721-723.
81. John, F.M., et al., *Handbook of X-ray photoelectron spectroscopy.* Perkin-Elmer Corporation Physical Electronics Division, 1992.
82. Evertsson, J., et al., *The Thickness of Native Oxides on Aluminum Alloys and Single Crystals.* Applied Surface Science, 2015. **349**: p. 826-832.
83. Milošev, I., et al., *Electrochemical, Surface-Analytical, and Computational DFT Study of Alkaline Etched Aluminum Modified by Carboxylic Acids for Corrosion Protection and Hydrophobicity.* Journal of The Electrochemical Society, 2019. **166**(11): p. C3131.

84. Milošev, I., et al., *The Effects of Perfluoroalkyl and Alkyl Backbone Chains, Spacers, and Anchor Groups on the Performance of Organic Compounds as Corrosion Inhibitors for Aluminum Investigated Using an Integrative Experimental-Modeling Approach.* Journal of The Electrochemical Society, 2021. **168**(7): p. 071506.
85. Kokalj, A., et al., *How Relevant Are Molecular Electronic Parameters for Predicting Corrosion Inhibition Efficiency: Imidazoles as Corrosion Inhibitors of Cu/Zr Materials in NaCl Solution.* Corrosion Science, 2021. **193**: p. 109900.
86. Getsoian, A.B., Z. Zhai, and A.T. Bell, *Band-Gap Energy as a Descriptor of Catalytic Activity for Propene Oxidation over Mixed Metal Oxide Catalysts.* Journal of the American Chemical Society, 2014. **136**(39): p. 13684-13697.
87. Vernack, E., et al., *DFT Studies of 2-Mercaptobenzothiazole and 2-Mercaptobenzimidazole as Corrosion Inhibitors for Copper.* Corrosion Science, 2020. **174**: p. 108840.
88. Kokalj, A., et al., *What Determines the Inhibition Effectiveness of ATA, BTAH, and BTAOH Corrosion Inhibitors on Copper?* Journal of the American Chemical Society, 2010. **132**(46): p. 16657-16668.
89. Kokalj, A., et al., *Simplistic Correlations between Molecular Electronic Properties and Inhibition Efficiencies: Do They Really Exist?* Corrosion Science, 2021. **179**: p. 108856.
90. Zabka, W.-D., et al., *Comparative Study of the Different Anchoring of Organometallic Dyes on Ultrathin Alumina.* The Journal of Physical Chemistry C, 2019. **123**(36): p. 22250-22260.
91. Mezzi, A. and S. Kaciulis, *Surface investigation of carbon films: from diamond to graphite.* Surface and Interface Analysis, 2010. **42**(6-7): p. 1082-1084.
92. Gardella Jr, J.A., S.A. Ferguson, and R.L. Chin, *$\pi^* \leftarrow \pi$ shakeup satellites for the analysis of structure and bonding in aromatic polymers by X-ray photoelectron spectroscopy.* Applied spectroscopy, 1986. **40**(2): p. 224-232.
93. Zhao, Y., et al., *Conformational preferences of π–π stacking between ligand and protein, analysis derived from crystal structure data geometric preference of π–π interaction.* Interdisciplinary Sciences: Computational Life Sciences, 2015. **7**(3): p. 211-220.
94. Koutsioubas, A.G., et al., *Formation of alkane‐phosphonic acid self‐assembled monolayers on alumina: an in situ SPR study.* Surface and Interface Analysis: An International Journal devoted to the development and application of techniques for the analysis of surfaces, interfaces and thin films, 2009. **41**(11): p. 897-903.
95. Cernetic, N., et al., *Enhanced Performance of Self‐Assembled Monolayer Field‐Effect Transistors with Top‐Contact Geometry through Molecular Tailoring, Heated Assembly, and Thermal Annealing.* Advanced Functional Materials, 2015. **25**(33): p. 5376-5383.
96. Ma, H., et al., *Multifunctional phosphonic acid self-assembled monolayers on metal oxides as dielectrics, interface modification layers and semiconductors for low-voltage high-performance organic field-effect transistors.* Physical Chemistry Chemical Physics, 2012. **14**(41): p. 14110-14126.
97. Spori, D.M., et al., *Influence of alkyl chain length on phosphate self-assembled monolayers.* Langmuir, 2007. **23**(15): p. 8053-8060.
98. Snijders, P., L. Jeurgens, and W. Sloof, *Structure of thin aluminium-oxide films determined from valence band spectra measured using XPS.* Surface science, 2002. **496**(1-2): p. 97-109.

99. Tanuma, S., C.J. Powell, and D.R. Penn, *Calculations of electron inelastic mean free paths. V. Data for 14 organic compounds over the 50–2000 eV range.* Surface and interface analysis, 1994. **21**(3): p. 165-176.

100. Strohmeier, B.R., *An ESCA method for determining the oxide thickness on aluminum alloys.* Surface and interface analysis, 1990. **15**(1): p. 51-56.

101. Gutiérrez, G. and B. Johansson, *Molecular dynamics study of structural properties of amorphous Al_2O_3.* Physical Review B, 2002. **65**(10): p. 104202.

102. Cabrera, N. and N.F. Mott, *Theory of the oxidation of metals.* Reports on progress in physics, 1949. **12**(1): p. 163.

103. Fehlner, F.P. and N.F. Mott, *Low-temperature oxidation.* Oxidation of Metals, 1970. **2**(1): p. 59-99.

104. Jeurgens, L.P.H., et al., *Growth kinetics and mechanisms of aluminum-oxide films formed by thermal oxidation of aluminum.* Journal of Applied Physics, 2002. **92**(3): p. 1649-1656.

105. Reichel, F., L.P.H. Jeurgens, and E.J. Mittemeijer, *The effect of substrate orientation on the kinetics of ultra-thin oxide-film growth on Al single crystals.* Acta Materialia, 2008. **56**(12): p. 2897-2907.

106. Cai, N., et al., *Effect of oxygen gas pressure on the kinetics of alumina film growth during the oxidation of Al(111) at room temperature.* Physical Review B, 2011. **84**(12): p. 125445.

107. Nemanick, E.J., et al., *Chemical and Electrical Passivation of Silicon (111) Surfaces through Functionalization with Sterically Hindered Alkyl Groups.* The Journal of Physical Chemistry B, 2006. **110**(30): p. 14800-14808.

108. Jeurgens, L.P.H., et al., *Composition and chemical state of the ions of aluminium-oxide films formed by thermal oxidation of aluminium.* Surface Science, 2002. **506**(3): p. 313-332.

109. Wagner, C., et al., *Auger and photoelectron line energy relationships in aluminum–oxygen and silicon–oxygen compounds.* Journal of Vacuum Science and Technology, 1982. **21**(4): p. 933-944.

110. Moretti, G., *Auger parameter and Wagner plot in the characterization of chemical states by X-ray photoelectron spectroscopy: a review.* Journal of Electron Spectroscopy and Related Phenomena, 1998. **95**(2): p. 95-144.

111. Wagner, C.D. and A. Joshi, *The auger parameter, its utility and advantages: a review.* Journal of Electron Spectroscopy and Related Phenomena, 1988. **47**: p. 283-313.

112. Wagner, C.D., et al., *Auger and photoelectron line energy relationships in aluminum–oxygen and silicon–oxygen compounds.* Journal of Vacuum Science and Technology, 1982. **21**(4): p. 933-944.

113. Siol, S., et al., *Concepts for chemical state analysis at constant probing depth by lab-based XPS/HAXPES combining soft and hard X-ray sources.* Surface and Interface Analysis, 2020. **52**(12): p. 802-810.

114. Snijders, P.C., L.P.H. Jeurgens, and W.G. Sloof, *Structure of thin aluminium-oxide films determined from valence band spectra measured using XPS.* Surface Science, 2002. **496**(1): p. 97-109.

115. Bakradze, G., L.P.H. Jeurgens, and E.J. Mittemeijer, *Valence-Band and Chemical-State Analyses of Zr and O in Thermally Grown Thin Zirconium-Oxide Films: An XPS Study.* The Journal of Physical Chemistry C, 2011. **115**(40): p. 19841-19848.

116. Filatova, E.O. and A.S. Konashuk, *Interpretation of the Changing the Band Gap of Al2O3 Depending on Its Crystalline Form: Connection with Different Local Symmetries.* The Journal of Physical Chemistry C, 2015. **119**(35): p. 20755-20761.
117. Thomas, S. and P.M. Sherwood, *Valence band spectra of aluminum oxides, hydroxides, and oxyhydroxides interpreted by X. alpha. calculations.* Analytical Chemistry, 1992. **64**(21): p. 2488-2495.
118. van den Brand, J., et al., *Acid−Base Characterization of Aluminum Oxide Surfaces with XPS.* The Journal of Physical Chemistry B, 2004. **108**(19): p. 6017-6024.
119. Flötotto, D., Z.M. Wang, and E.J. Mittemeijer, *On the structural development during ultrathin amorphous Al2O3 film growth on Al(111) and Al(100) surfaces by thermal oxidation.* Surface Science, 2015. **633**: p. 1-7.
120. Snijders, P.C., L.P.H. Jeurgens, and W.G. Sloof, *Structural ordering of ultra-thin, amorphous aluminium-oxide films.* Surface Science, 2005. **589**(1): p. 98-105.
121. Demichelis, R., et al., *Structure and stability of aluminium trihydroxides bayerite and gibbsite: A quantum mechanical ab initio study with the Crystal06 code.* Chemical Physics Letters, 2008. **465**(4): p. 220-225.

Acknowledgements

It is a pleasure for me to spend wonderful five years in Switzerland. Switzerland is an amazing country: people are polite and friendly; nature scenery is beautiful; it is a small country but accommodates all different cultures and languages. However, if I hadn't met you, I'd just be another foreign tourist and wouldn't really appreciate the Swiss life.

Looking back on the timeline, my academic career in Switzerland started with my master's project at Empa in 2017. Dr. Sabyasachi Gaan opened the gate of scientific research to me for the first time. I am very grateful for your professional scientific research spirit and tireless answering questions. You not only gave me professional support, but also gave me a lot of philosophical thinking about life, which I will benefit in my entire life.

I would like to thank my colleagues in the department of Advanced Fibers 402, Empa St. Gallen: we are not only colleagues at work, but also friends in life. I will miss those suffering days with you in the lab, and those highlight moments of the party after work.

In the year of 2018 I started my doctoral research life. Here, I would like to thank the Chinese Scholarship Council (CSC) and the Education Office of the Chinese Embassy in Switzerland. You sponsored a part of my research and made this doctoral work possible.

I would like to thank Prof. Dr. Manfred Heuberger; you are the one who spends most of effort in the whole process from the initial doctoral research plan defense, to the publication of the first paper, and to the final doctoral thesis/defense. You are also the first person to let me realize the meaning of "being a professor". In countless update meetings, you are always the wisest one: in the multi-disciplinary and complicated discussions, you have put forward refreshing scientific guidance, which has continuously deepened professionalism of this doctoral project. Your rigorous scientific attitude of seeking truth from facts and your respectful guidance to the younger generation have benefited me for a lifetime. At the same time, from every discussion with you, I have gradually learned from you how to impart knowledge from the simple to the deep. One day in the future, I may also become a senior, a boss; I hope I can become a person like you.

Throughout my doctoral research time, I have also developed close collaborations and deep friendships with my colleagues in the department of Joining Technologies and Corrosion 202, Empa Duebendorf. Dr. Patrik Schmutz took me into the field of surface science, corrosion science and electrochemistry science and gave me many instructions. You showed me a completely new perspective on the translation of laboratory research results to industrial application.

In addition, I am sorry that the EQCM story that we put a lot of effort into is not presented in this doctoral thesis. However, I believe that in the future, more results will be generated from the EQCM we build. Meanwhile, I would like to thank Dr. Noemie Ott, many thanks for your help on EIS test and correcting all my English typo mistakes.

I would like to thank Dr. Roland Hauert for his guidance on using the XPS. From the initial sample preparation to XPS detection, as well as the final data analysis. Through your guidance, I have become a quasi-professional XPS user. Many of my colleagues also benefit from this. At the same time, I would like to thank Dr. Lars Jeurgens. Your strict requirements for oxide sample preparation and analysis have made me deeply appreciate the true meaning of "spirit of the craftsman". In addition, employing the brand new HAXPES to enrich this doctoral project is a great idea.

I would like to thank the many postdocs who met me briefly at Empa but helped me a lot. You brought me into the field of organic chemistry synthesis. Although I still failed to purify enough molecules for my research, you gave me an enjoyable experience of the magic of organic synthesis.

I would like to thank some old friends. Without the introduction and recommendation from Julian Quatier, I would not consider Switzerland to complete my master's program. Also thanks to the Niessen family, you were the first friends I met in Switzerland (even before I went to Empa). In later life in Switzerland, you invited me to many Swiss festivals, Christmas, New Year's Eve, and your wedding. This also allows me to understand and experience Swiss culture more; I wish Lilli good health and many happy days. I would also like to thank Pietro Simonetti, Dr. Alessia Pasqualini, Dr. Ezgi Bulbul and Dr. Konrad Jakubowski for our friendship when we firstly arrived in Switzerland. In the following five years, the friendship has not cooled down. Meanwhile, I would like to thank to other doctoral students, Ruikai Wu, Danielle Roncucci, Jiuke Chen and Roberto Cestaro. I will always miss our scientific discussion in the office when we close the door.

Finally, I would like to sincerely thank my parents. You have given me a home that I can rely on. You also supported my every decision and gave me spiritual support. I'm sorry I haven't been home to see you for over three years for various reasons, but I hope this doctoral thesis is a gift that you can be proud of.

For me, English is only a foreign language for communication, and the gratitude presented here is less than a thousandth of my heart.